UNIVERSITEIT VAN PRETORIA
UNIVERSITY OF PRETORIA
YUNIBESITHI YA PRETORIA

UNIVERSITEIT VAN PRETORIA
UNIVERSITY OF PRETORIA
YUNIBESITHI YA PRETORIA
Denkleiers • Leading Minds • Dikgopolo tša Dihlalefi

Visualisation of electrolyte flow fields in an electrolysis cell

by

Xolani Melane

14454182

A dissertation submitted in partial fulfilment of the requirements for the degree

Master of Engineering (Chemical Engineering)

Supervisor: Prof. P.L. Crouse
Co-supervisor: Dr. D. van Vuuren

Department of Chemical Engineering
Faculty of Engineering, the Built Environment and Information Technology
University of Pretoria

December 2015

Plagiarism declaration

Full names	Xolani Melane
Student number	14454182
Topic of work	Visualisation of electrolyte flow fields in an electrolysis cell

Declaration

1. I understand what plagiarism is and am aware of the University's policy in this regard.
2. I declare that this dissertation is my own original work. Where other people's work has been used (either from a printed source, internet or any other source), this has been properly acknowledged and referenced in accordance with the requirements as stated in the University's plagiarism prevention policy.
3. I have not used another student's past written work to hand in as my own.
4. I have not allowed, and will not allow, anyone to copy my work with the intention of passing it off as his or her own work.

Signature _____

Visualisation of electrolyte flow fields in an electrolysis cell

SYNOPSIS

The performance and efficiency of an electrochemical system with gas evolution can be related to the mass transfer effects which are influenced by the resulting two-phase flow. The aim of this investigation was to develop a better understanding in the effects of current density, anode height and inter-electrode spacing on the electrolyte flow patterns and to validate Computational Fluid Dynamic (CFD) model predictions of the electrolyte flow patterns. The CFD model was developed in a previous study and was applied to the experimental rig developed for this study, in which the electrolysis of copper sulphate was studied.

A direct flow visualisation technique was used as the method of investigation in the experimental work. To facilitate the visual observation of the electrolyte flow patterns, O_2 gas bubbles evolved on the anode surface were used as the flow followers to track the electrolyte flow patterns. At the bottom of the anode where there was no gas evolution, polyamide seeding particles (PSP) were used as the flow followers. A Photron FASTCAM SA4 high speed camera with a capability of recording up to 5000 fps was used to record the electrolyte flow patterns and circulation. The Photron FASTCAM Viewer (PFV) camera software was used for the post analysis of the recordings and for measuring bubble size, bubble speed and the speed of the PSP tracking particles.

The experimental results were then compared with the results obtained from the CFD model simulation in order to validate the CFD model. The electrolysis cell was approximated by a simplified planar two-dimensional domain. The fluid flow patterns were assumed to be affected only by the change in momentum of the two fluids. To simplify the model, other physical, chemical and electro-magnetic phenomena were not modelled in the simulation. The Eulerian multiphase flow model was used to model the multiphase flow problem investigated.

The flow fields observed in the experiments and predicted by the model were similar in some of the positions of interest. The gas bubble flow field patterns obtained in the experiment and model were similar to each other in Position A (the top front of the anode), C (the area at the bottom of the cell

below the anode), and D (the gap between the anode and the diaphragm), with the only exception being Position B (slightly above the anode top back). The experimental results showed an accumulation of the smaller gas bubbles in Position B with a resulting circulation loop across that region. On the other hand, the model predictions did not show this gas bubble accumulation and circulation in Position B.

All the flow patterns predicted for the electrolyte flow illustrated similar flow patterns to the ones observed in the experimental results, including the circulation loop in Position B. The bubble speeds measured at Position A in the experimental work had a reasonable agreement with the bubble speeds predicted by the model. The error between the two results ranged from 6% to 29% for the various cases which were tested.

An increase in the current density generated more gas bubbles which resulted in an increase in the bubble speed. Increasing the anode height increased the amount of gas bubbles generated as well as bubble speed while the bubble speed was decreased with an increasing inter-electrode distance.

KEYWORDS: electrolysis cell, direct flow visualisation, bubble size, bubble speed, electrolyte flow patterns, CFD model

ACKNOWLEDGEMENTS

I would like to acknowledge the CSIR for affording me the opportunity to conduct my master's research by providing me with the necessary funding and support to complete the project.

I would like to express sincere gratitude to Dr David Van Vuuren and Prof. Philip Crouse for their support, guidance and supervision throughout the project.

I would like to thank the CSIR workshop team for their assistance in the construction of the electrolysis cell.

I would also like to thank Mangalani Miyambo and Martin Mwila from the CSIR DPSS unit for their assistance with the high speed camera video imaging.

I would also like to thank Jeffrey Baloyi from the CSIR MDS unit for his assistance with the CFD modelling work.

I want to thank my family for the support they have given me throughout my academic career.

TABLE OF CONTENTS

LIST OF FIGURES

LIST OF TABLES

1. INTRODUCTION

The Council of Scientific and Industrial Research (CSIR) is researching ways to develop a more economical process to produce the titanium metal via the reduction of $TiCl_4$ with an alkali or alkaline earth metal. The cost of producing these metals is a significant fraction of the total cost of producing the titanium metal. As a result, the CSIR is studying alternative cell designs that can be used to economically produce alkali/alkaline earth metals by molten salt electrowinning.

In the course of the CSIR's studies, a novel electrolysis cell design was proposed and a patent application filed to seek protection of the intellectual property (Van Vuuren, Terblanche & Swanepoel, 2013). In contrast to the conventional Downs cell design (Downs, 1924), the CSIR cell design employs planar electrodes instead of cylindrical electrodes with the electrodes arranged in a sequence of anode-cathode-anode assemblies. One particular advantage of this arrangement is that the electrolyte flow is induced to flow upwards between the electrodes and then over the anodes rather than over the cathodes as in the Downs cell. It is believed that with this flow pattern fewer gas bubbles will be collected with the liquid metal product above the cathodes than in the Downs cell design resulting in higher current efficiencies.

In a previous confidential study, a CFD model was developed and used to predict the flow of a molten salt electrolyte inside an electrolysis cell with planar electrodes (Baloyi *et al.*, 2014). However, due to the complexity of the system and all the simplifying assumptions that had to be made, it was uncertain whether or not the predictions were realistic. It was therefore decided that in order to validate the model predictions an experimental investigation must be conducted using a simpler system whereby the flow patterns can be observed and measured (Baloyi *et al.*, 2014). Typically, there is insufficient validation of the predictions made by CFD models because of inadequate experimental data (Hreiz *et al.*, 2015). Thus, it is important to obtain experimental data to validate model predictions.

To obtain the required experimental observations and measurements it was required to have an electrolysis cell that would enable visual observation. As part of this work, an electrolysis cell that allowed optical visualisation and subsequent study of the flow patterns was designed

and constructed. The details of this experimental electrolysis cell design will be presented later in the document.

In a gas-evolving electrolysis cell where an aqueous salt solution is electrolysed, gas bubbles evolve on the surface of one or both of the electrodes depending on the electrolyte used (Pletcher & Walsh, 1990b: 1-55; Hreiz *et al.*, 2015). The gas bubbles evolved in these electrochemical systems create a buoyancy induced two-phase flow in the area next to the electrode surface (Mandin *et al.*, 2014). The electrolysis of some molten salts can also produce gas bubbles which induce such a two-phase flow (Kuhn, 1971: 177-178). Gas evolving electrochemical cells are widely used in industrial operations for the production of various chemicals and metals (Pletcher & Walsh, 1990b: 1-55). However, there are few experimental studies investigating the two-phase flow in electrolysis cell reported in literature (Mandin *et al.*, 2014). As a result, there are a number of gaps in the knowledge about the effects of gas evolution and subsequent two-phase flow on the cell performance and efficiency.

Various design parameters such as electrode material, dimensions, electrolyte type, operating conditions and cell configurations have an effect on cell performance and on the determination of flow patterns in an electrolysis cell (Abdelouahed *et al.*, 2014a; Ashraf Ali & Pushpavanam, 2011a; Hine *et al.*, 1980; Sillen *et al.*, 1982). The cell configuration and operating conditions have been identified as important parameters for reducing the gas void fraction, voltage drops and subsequently improve efficiency in gas evolving electrolysis cells (Hine *et al.*, 1980; Abdelouahed *et al.*, 2014b; Nagai *et al.*, 2003b).

The main aim of this study was to visualise and measure the flow patterns inside an electrolysis cell with planar electrodes by using an experimental setup. Furthermore, to validate the CFD modelling approach used in previous work with the aim to use the model in future design and optimisation studies.

To achieve these aims the objectives were to:

- Design and construct an electrolysis cell that enables visual observation of the flow patterns inside the cell.
- Identify techniques to qualitatively and quantitatively study the flow patterns.

- Test the effect of current density, anode height and inter-electrode spacing on the flow patterns and electrolyte circulation rates.
- Apply the developed CFD model on the system investigated and validate the modelling approach by comparing the experimental results with the model results.
- Test the effectiveness of the diaphragm design that was used in preventing the gas bubbles from entering the channel between the diaphragm and the cathode.

This study focused on a particular cell design with the aim of getting a better understanding of how the cell operates in order to able to make improvements on the functionality and design of the electrolysis cell. Therefore, the focus of this investigation was based on studying the flow patterns inside the electrolysis cell. This was done by observing, measuring and analysing electrolyte flow patterns and circulation caused by gas evolution on the anode surface. Direct flow visualisation was used as the method of study whereby a high speed camera was used to capture the electrolyte flow field for measurements and analysis. Furthermore, the experimental results were compared to the results obtained from a CFD model in order to validate the modelling approach.

The structure of the dissertation is as follows: Chapter 1 presents the introduction of the thesis whereby the background, problem statement and objectives of the research work are laid out. Chapter 2 gives an overview of the relevant theory related to this work. This looks at the factors that affect electrolysis cell performance with a focus on gas evolving cells. Chapter 3 presents the electrolysis cell design, experimental setup and experimental procedures. Chapter 4 presents the results obtained from the experimental work together with discussion of the findings. Chapter 5 presents the results obtained from the CFD model simulations, and Chapter 6 presents the conclusions drawn from the findings and recommendations for future studies.

2. LITERATURE REVIEW

2.1. Introduction

This chapter presents the theoretical framework, principles and techniques which underpin this study. To introduce the theory a brief background on the field of the study is presented and then more details are unpacked in the main section.

Electrochemical processes are based on electrolysis, where an otherwise non-spontaneous chemical reaction is driven by the application of an electric potential across an electrolyte (Pletcher & Walsh, 1990b: 1-55). In electrochemical reactions, a chemical change is brought about by the passage of current; the electrochemical reactions occur at the surface of electrodes immersed in an electrolyte (Sandenbergh, 2014c). For electrolysis to occur, electrons must pass from the anode to the cathode through an external electric circuit connecting the electrodes (Pletcher & Walsh, 1990b: 1-55). The electrolyte between the electrodes must complete the circuit by providing a mechanism for charge transport within the cell (Pletcher & Walsh, 1990b: 1-55; Goodridge & Scott, 1995: 1-16).

Electrolysis is used in various industrial applications for the production of chemicals and metals. The most commonly used electrolytic processes include metal electrowinning, electrorefining, electrodeposition, electroplating, hydrodimerization and inorganic electrolytic processes (Pletcher & Walsh, 1990b: 1-55). Depending on the application, various molten salts (in metal production) and aqueous salt solutions can be used as the electrolyte in these electrolytic processes.

2.2. Gas-evolving electrolysis cells

Electrolytic gas evolution is an important phenomenon in most electrochemical processes in applied electrochemistry (Janssen, 1989). Some of the widely used and most popular electrochemical processes which involve gas evolution are presented below.

2.2.1. Chlor-alkali process

The chlor-alkali process is an electrochemical process used for the production of chlorine gas from NaCl. A direct current is passed through an aqueous solution of NaCl to decompose the NaCl into Cl_2, H_2 and NaOH solution (Schmittinger, 2003: 186-215). There are three common industrial processes used to produce Cl_2. These are the diaphragm cell process, mercury cell process and membrane cell process (Pletcher & Walsh, 1990b: 1-55;

Schmittinger, 2003: 186-215). These processes each represent a different approach of separating the Cl_2 produced at the anode from the NaOH and H_2 produced at the cathode. The electrolysis of an aqueous solution of NaCl results in the evolution of Cl_2 and H_2 gas at the anode and cathode respectively (Schmittinger, 2003: 186-215).

Chlorine can also be produced electrochemically via the electrolysis of hydrochloric acid, molten alkali metal and alkaline earth metals where Cl_2 is a by-product (Schmittinger, 2003: 186-215). The membrane cell process has been the most favoured and dominant process due to its environmental and financial benefits. As a result, all new plants are using the membrane cell process for the production of chlorine gas (Schmittinger, 2003: 186-215).

2.2.2. Molten salt electrolysis

Molten salt electrolysis is mainly used for the electrowinning of reactive metals where the potential required to reduce the metal cation to the metal is so negative that the decomposition of water cannot be avoided (Sandenbergh, 2014e). Electric conductivity, electrode reaction rate and high decomposition potential of the electrolyte are the main advantages of using molten salts in electrolytic systems. Molten salts are good conductors of electricity and their high conductivity is of great importance in the efficiency of electrolytic processes (Grjotheim *et al.*, 1998: 42-71).

The conductivity of molten salts is much higher than the conductivity of the same salts in aqueous solution and also higher than that of organic electrolytes (Mantell, 1960: 1-13; Grjotheim *et al.*, 1998: 42-71). The high conductivity helps to limit the ohmic voltage drop (Sandenbergh, 2014e). The high temperatures in molten salt electrolysis contribute in making the process have fast electrode reaction rate and less polarization (Grjotheim *et al.*, 1998: 42-71).

Furthermore, as a result of these advantages molten salts have been used in various electrochemical processes. Amongst others, they have been used in metal production, metal refining, electroplating and deposition, inorganic chemicals production, and organic chemicals production. The Hall-Heroult process is used almost exclusively for the production of aluminium metal (Grjotheim *et al.*, 1998: 42-71; Sandenbergh, 2014d).

2.2.3. Alkaline water electrolysis

Alkaline water electrolysis is a process used to produce both very pure hydrogen and oxygen gas (Pletcher & Walsh, 1990c: 256-268). Alkaline water electrolysis is widely used for the large scale production of hydrogen gas (Pletcher & Walsh, 1990c: 256-268; Nagai *et al.*, 2003a). However, this is an expensive route to produce the H_2 gas compared with the separation of CO and H_2 from synthesis gas produced by coal gasification (Pletcher & Walsh, 1990c: 256-268).

Typically, an alkaline solution of NaOH, KOH or LiOH is usually used as the electrolyte in hydrogen and oxygen production (Mantell, 1960: 1-13). A direct electric current is passed through the alkaline solution between the electrodes and forces a reaction that splits the water molecule into its elements. During water electrolysis, oxygen and hydrogen gas bubbles are evolved at the anode and cathode respectively (Sillen *et al.*, 1982). A diaphragm between the anode and the cathode is used to separate the two gases formed (Mantell, 1960: 1-13).

2.3. Electrolysis cell performance

The process of optimizing electrochemical systems through improving the cell design and optimising operating conditions involves a number of factors that need to be understood thoroughly. This allows a more informed decision making in the design of the cell and enables relevant modifications to improve performance and efficiency. Some of these design and operational parameters have been identified and are discussed below.

2.3.1. Gas bubble evolution

Gas evolution in electrolysis cells occurs in three stages, nucleation, growth and detachment (Matsushima *et al.*, 2013; Zhang & Zeng, 2012). The gas bubble nucleates at the electrode surface adjacent to the electrolyte solution which is saturated with the dissolved gas species. The bubble then grows under the mass transport controlling condition for the dissolved gas. When the buoyancy force is greater than the interfacial tension force, the bubble detaches from the electrode surface and moves to the bulk solution (Matsushima *et al.*, 2013). The detached bubbles move upwards under the buoyancy force and this mechanism creates a two-phase flow near the electrode surface (Hreiz *et al.*, 2015; Vogt, 1978).

The steps that the bubbles undergo determine both the residence time and the diameter of the gas bubbles (Zhang & Zeng, 2012). These two factors are important for determining the

resistance effect of the evolved gas bubbles (Zhang & Zeng, 2012). A high bubble population and residence time increases the gas void fraction resulting in a high electrolyte resistance (Sillen *et al.*, 1982). The high electrolyte resistance causes an increase in the electrolyte potential drop and subsequently affects the energy efficiency of the cell (Sandenbergh, 2014c; Sillen *et al.*, 1982).

Parameters such as electrode geometry, electrode material, cell design, type of electrolyte and operating conditions have been identified as the major factors that affect gas bubble evolution (St-Pierre & Wragg, 1993; Vogt, 1985). Under certain conditions, the bubbles formed may coalesce with neighbouring bubbles to form bigger gas bubbles (Matsushima *et al.*, 2013).

The presence of gas bubbles and their motion inside the cell has a significant effect on the performance of the electrolytic cell (Philippe *et al.*, 2005). Gas bubbles can form a layer at the electrode surface which can lead to a complete deactivation of the electrode (Sillen *et al.*, 1982). This bubble layer introduces an additional resistance to mass and ion transport to the electrode (Zhang & Zeng, 2012). When the kinetics of the system is mass transfer controlled, the bubble layer formed will significantly lower the electrode kinetics. The main challenge in operating electrolysis cell with gas evolution is to minimize the resistance caused by gas bubbles and subsequently improve the electrode kinetics and cell efficiency (Zhang & Zeng, 2012).

Furthermore, as a result of this bubble shielding the reactive surface area and reaction rate of the electrodes is reduced (Wüthrich *et al.*, 2005; Philippe *et al.*, 2005). Due to the bubble coverage and the subsequent surface reduction of the working electrode, the cell overvoltage increases (Hine *et al.*, 1980). All these bubble effects result in a reduction in energy efficiency and high energy consumption when operating the cell (Zhang & Zeng, 2012; Hine *et al.*, 1980; Philippe *et al.*, 2005). In addition, the mass transfer rate and the effective cell performance are significantly reduced as a result of the bubble coverage (Matsushima *et al.*, 2013; Boissonneau & Byrne, 2000; Eigeldinger & Vogt, 2000; Aldas, 2004). Hence, the fraction of the electrode surface covered or shielded by adhering gas bubbles has been identified as the controlling parameter of mass transfer rates in gas-evolving electrodes (Matsushima *et al.*, 2013; Eigeldinger & Vogt, 2000).

The electrical and thermal properties of the electrolyte, diffusive transport of electro active species and current density are all modified by the presence of gas bubbles (Philippe *et al.*, 2005). This is due to the fact that gas bubbles have zero conductivity and their presence in a system will thus affect potential and current distributions (Abdelouahed *et al.*, 2014a). As a result of these modifications, the macroscopic performance of the electrolytic cell is significantly affected (Philippe *et al.*, 2005). All these changes in the electrical properties of electrochemical cells have a negative effect on the systems overall performance and efficiency. Thus, optimization studies are investigating various cell configurations and designs that can allow a quick removal of gas bubbles from the electrode surface (Abdelouahed *et al.*, 2014a).

In the light of the above, it is therefore essential to understand the rate of formation, gas evolution, ion transport, mass transfer and motion of gas bubbles in order to optimize cell performance and efficiency.

2.3.2. Bubble size and bubble velocity

A number of studies reported in the literature have used different techniques to measure and calculate bubble size and bubble velocity. The typical values reported in the literature have been reviewed and will be used as a guide for this investigation in terms of what values can be expected and which measurement techniques can be used. It should be noted that these values differ for different electrochemical systems.

The aim of measuring bubble size and velocity in gas-evolving electrolysis cell is mainly to gain data for modelling studies. Matsushima *et al.*, (2013) measured the bubbles size of O_2 gas bubbles formed during alkaline water electrolysis at a current density of 0.3 A/cm^2. They reported an average bubble size of the rising O_2 gas bubbles growing on the anode surface to be between 0.015-0.07 mm. A minimum bubble size of 5 µm was recorded in their measurements.

Abdelouahed *et al.*, (2014) measured O_2 gas bubble velocity along the anode surface and reported bubble velocities varying from 5-25 mm/s. Model predictions of an electrochemical cell with gas evolution reported time averaged axial liquid velocities between 0.006-0.2 m/s, taken at different locations along the electrode and at different current densities (Alexiadis *et al.*, 2011). Bubble diameters between 0.59 to 1.09 mm at current densities between 3 to 6

A/m^2 in a 0.5 M KOH solution have been reported in (Zhang & Zeng, 2012). A study conducted in an alkaline water electrolysis cell reported bubble velocities ranging from 4-24 cm/s and bubble diameters of 0.01-0.08 mm (Nagai *et al.*, 2003b).

It has been noted that the current density greatly influences the mean bubble diameters and bubble velocities in an electrolysis cell (Nagai *et al.*, 2003b; Hreiz *et al.*, 2015; Vogt, 1989). The bubble growth rate increases with an increase in current density (Sillen *et al.*, 1982). On the contrary, Vogt (1989) states in a stationary electrolyte the diameter at detachment from an electrode typically decreases with an increase in current density. However, this only applies to bubbles on the electrode surface and the author acknowledges the fact that moving bubbles may exhibit a different behaviour, due to bubble coalescence (Vogt, 1989).

Other factors that determine bubble size are electrolyte density, surface tension, contact angle, surface roughness, electrode potential, pH, flow rate, temperature, pressure and geometry (St-Pierre & Wragg, 1993; Vogt, 1989). However, in this study only the effects of current density and cell geometry will be investigated and other variables will remain constant.

2.3.3. Gas-liquid flow

Gas-liquid two-phase flow in electrolysis cells is induced by the evolution of gas bubbles along the electrode surfaces (Ashraf Ali & Pushpavanam, 2011b; Alexiadis *et al.*, 2011). Fluid flow and mass transfer can be forced by electrochemically producing gas bubbles at an electrode's surface (Boissonneau & Byrne, 2000). The flow induced by gas evolving electrodes is very important in determining the mass transfer, electrolyte mixing, gas distribution, ionic transport and overall cell performance (Mat & Aldas, 2005; Alexiadis *et al.*, 2011; Vogt, 2011; Liu *et al.*, 2015).

The two-phase flow also influences the macro scale electrolyte motions which are caused by the density gradients of the gas-liquid mixture (Wedin *et al.*, 2003). In the presence of the evolved gas bubbles, a vertical electrolyte motion driven by buoyancy force can be observed. This buoyancy driven flow can be expected to form circulation flow patterns (Alexiadis *et al.*, 2011). Moreover, the induced electrolyte circulation is mainly responsible for mixing, which then promotes ion transport and mass transfer (Ashraf Ali & Pushpavanam, 2011a). The

focus of this study was to get a better understanding of these electrolyte circulation patterns and the factors that influence them.

The presence of gas bubbles in the fluid causes fluctuations in the electrical conductivity of the electrolyte which in turn affects the performance and efficiency of the electrolysis cell (Wedin *et al.*, 2003). It is therefore essential to have an understanding of the strong coupling effects between the evolved gas bubbles and the electrolyte solution for predicting the overall electrolyte conductivity and macro scale motions (Wedin *et al.*, 2003). In order to improve ion transport, mass transport, system optimization and efficiency it is vital to thoroughly understand the effects of the two-phase flow in electrochemical systems with gas evolution (Mat & Aldas, 2005).

2.3.4. Mass transfer

In general, mass transport in electrochemical systems occurs in three forms and these are diffusion, migration and convection (Pletcher & Walsh, 1990b: 1-55). During electrolysis, a reaction occurs at the electrode surface to form a certain product. This means a boundary layer develops at the electrode surface in which the reactants concentration is lower than in the bulk. As a result of this concentration gradient, the reacting species will diffuse towards the electrode and the products formed will diffuse away from the electrode surface (Pletcher & Walsh, 1990b: 1-55).

Migration is the movement of charged species which is induced by a potential gradient. It is the mechanism by which charge passes through the electrolyte (Pletcher & Walsh, 1990b: 1-55). The migration transport mechanism is driven by electrostatic forces and does not differentiate between the types of ions to be transported. This leads to a small amount of the electroactive species being transported by migration.

Convection is the movement of a species as a result of a mechanical force (Pletcher & Walsh, 1990b: 1-55). This represents forced convection and it is usually achieved by agitating an electrolyte solution or passing it through a cell (Pletcher & Walsh, 1990b: 1-55). On the other hand, natural convection occurs when a chemical reaction at the electrode surface causes small differences in the density. At a very low current density, the dissolved gas near the electrodes is transported to the bulk solution by means of convection and diffusion (Sillen *et al.*, 1982).

The performance of electrochemical processes which involve gas evolution at the electrode surface is intrinsically related to mass transfer effects which are influenced by hydrodynamics (Boissonneau & Byrne, 2000; Riegel *et al.*, 1997). The gas bubbles formed during electrolysis significantly affects mass transfer which is an important parameter in determining electrolysis reaction rate (Aldas, 2004).

Mass transfer at gas evolving electrodes is controlled by macro-convective and micro-convective mass transfer, acting simultaneously in such electrodes (Vogt, 1978). Macro-convective mass transfer is due to the liquid flow parallel to the electrode surface which influences mass transfer by the velocity distribution near the wall. Micro-convective mass transfer is linked with the bubbles adhering to the electrode surface (Vogt, 1978). Adhering gas bubbles causes micro-convection near the growing bubbles which push away the electrolyte from the electrode in a radial direction (Matsushima *et al.*, 2013; Vogt & Stephan, 2015). This causes a disturbance of the diffusion layer and an increase in mass transfer (Vogt, 1978).

Furthermore, at certain operating conditions the micro-convection induced by gas bubbles exerts the controlling action on mass transfer at gas evolving electrodes (Eigeldinger & Vogt, 2000). This can be observed at high current densities as the number of adhering bubbles increases and hence, the influence of micro-convective mass transfer increases at the expense of macro-convective mass transfer (Vogt 1978).

An increase in macro-convection has been shown to reduce the departure diameter of gas bubbles by disturbing the balance between adhesion and buoyancy forces (Vogt 1978). At certain conditions the macro-convection can superimpose other mass transfer mechanisms and also interfere with micro-convective mass transfer by reducing the bubble coverage (Eigeldinger & Vogt, 2000). The bubble coverage represents the fraction of the electrode area shaded by adhering gas bubbles (Matsushima *et al.*, 2013).

Parameters such as the size of gas bubbles at the moment they detach/depart from the electrode and bubble coverage have been considered when estimating the mass transfer rates at gas evolving electrodes (Eigeldinger & Vogt, 2000; Vogt, 1989). Moreover, the detachment of gas bubbles causes turbulence in the electrolyte boundary layer which enhances the heat and mass transfer rate (Matsushima *et al.*, 2013).

The fractional bubble coverage is strongly affected by the liquid flow past the electrode surface (Eigeldinger & Vogt, 2000). Increasing flow reduces the bubble coverage which in turn affects the mass transfer rates at the electrode surface (Eigeldinger & Vogt, 2000). On the other hand, the size of the bubbles depends on the concentration and pH of the electrolyte at the electrode-electrolyte interface, polarity and potential of the electrodes (Vogt, 1989).

2.3.5. Current density

According to Faraday's law, the amount of electrogenerated gas per unit electrode area is directly proportional to the current density of the cell (Abdelouahed *et al.*, 2014b; Liu *et al.*, 2015). When the current density is increased, the supersaturation of the liquid exceeds a lower limit sufficient for gas evolution and the first gas bubbles are formed at the electrode (Vogt, 1978; Eigeldinger & Vogt, 2000). Thereafter, any further increase in the current density results in more gas bubble formation. An increase in current density increases the number of active nucleation sites and it can cause activation of the smaller nucleation sites. As a result, this causes an increase in bubble population, bubble frequency and the tendency of bubbles to coalesce (Sillen *et al.*, 1982). High gas volume fractions can be observed at high current densities and small bubble sizes (Abdelouahed *et al.*, 2014b; Liu *et al.*, 2015). High current densities have also been shown to increase the gas production rates (Mat & Aldas, 2005). These results are similar to the findings reported by (Aldas, 2004; Sillen *et al.*, 1982; Glas & Westwater, 1964; Abdelouahed *et al.*, 2014b; Liu *et al.*, 2015). The increase in current density can also increase the velocity of the electrolyte flow (Liu *et al.*, 2015).

However, the electrogenerated gas bubbles can accumulate at the electrode surface and form a gas bubble layer which reduces the electrode active reaction area (Boissonneau & Byrne, 2000; Wüthrich *et al.*, 2005). Consequently, there is a reduction in the reaction rate of the electrodes and overall cell performance (Aldas, 2004). This is mainly due to the fact that the performance of an electrochemical process is highly dependent on the flow of the reacting species or ions towards the electrode surface (Ashraf Ali & Pushpavanam, 2011a). The bubble coverage increases with increasing current density as more bubbles are evolved at high current densities (Matsushima *et al.*, 2013). It has been observed that at high current densities gas bubble evolution becomes the rate limiting step in the electrochemical process (Wüthrich *et al.*, 2005).

Riegel *et al.*, (1997) observed a back flow and an increase in electrolyte resistance at high current densities. This is expected since at high current densities the gas bubble formation is enhanced and the increase in the bubble population results in a decrease in solution conductivity and an increase in resistance. On the other hand, low current densities result in the two-phase flow being confined to a thin layer along the electrode surface (Riegel *et al.*, 1997).

Dahlkid (2001) observed that a non-uniform bubble distribution along the electrodes causes a non-uniform current density distribution and this result was found to be consistent with existing experimental findings in literature.

Riegel *et al.*, (1997) observed that an increase in current density resulted in a higher void fraction at the cathode surface. Similar observations were made in the findings of a two-phase flow model for natural convection developed by (Mat & Aldas, 2005). The void fraction of gas is another factor that has a hindering effect for electrical current which in turn reduces the cell energy efficiency (Aldas, 2004). Furthermore, Aldas (2004) showed that the void fraction of gas increases with increasing electrode height. Therefore, suggesting that there is an optimal electrode height that can be exploited in the cell design to avoid a large void fraction of gas.

2.3.6. Cell voltage

The energy consumption of an electrochemical process is highly dependent on the cell voltage and current efficiency (Pletcher & Walsh, 1990a: 60-141). Therefore, to improve the overall efficiency of an electrolysis cell, the energy consumption can be minimized by reducing the cell voltage. Furthermore, the applied current needs to be exclusively used for reaction purposes only (Pletcher & Walsh, 1990a: 60-141). The voltage of an electrolytic cell can be estimated by using Equation 2-1 below;

$$E_{cell} = E_e^C - E_e^A - |\eta_C| - |\eta_A| - iR_{cell} - iR_{circuit} \quad (2\text{-}1)$$

where E_{cell} is the cell voltage, E_e^C and E_e^A are the equilibrium potentials for the cathode and anode reactions respectively, η_C is the cathode overpotential, η_A is the anode overpotential, iR_{cell} is the voltage drop across the cell due to the ohmic resistance of the cell components with R_{cell} the internal resistance of the cell and $iR_{circuit}$ the voltage drop across the external

circuit of the cell, mainly across the electrical connections (Pletcher & Walsh, 1990a: 60-141).

Equation 2-1 illustrates that the important parameters that determine energy efficiency in the cell are the electrode kinetics, electrolyte properties and cell design (Pletcher & Walsh, 1990b: 1-55). The overpotential and *iR* terms represent energy efficiencies of an electrolytic process (Pletcher & Walsh, 1990a: 60-141). When charge transfer is the rate limiting step in the reaction sequence, the rate of electrochemical reactions is very dependent on the potential gradient next to the electrode surface (Sandenbergh, 2014b). As a result, this affects the electrode overpotential required to activate the reaction at the electrode surface. To obtain the required current density to drive an electrode reaction, applying overpotential is necessary. The overpotential required at the electrodes is essential to enhance electron transfer. When the terms in Equation 2-1 are minimized and controlled, the cell will operate at optimal energy efficiency.

The cell voltage is affected by process parameters such as temperature, electrolyte concentration, electrolyte flow, electrolyte conductivity, electrode material, electrode configuration and surface conditions (Pletcher & Walsh, 1990a: 60-141). In the design of an electrolytic cell, all these parameters need to be considered as they play a role in determining cell voltage and subsequently cell performance and efficiency.

2.3.7. Overpotentials

When a large enough direct current voltage difference is applied across a cell to cause electrochemical reactions to occur at the electrodes, current flows through the system. In the system there are various resistances to the current flow which results in voltage drops over and above the minimum decomposition voltage required for the electrochemical reaction. These voltage drops are called overpotentials. The processes that lead to overpotentials are ohmic (IR) drop, concentration overpotential and activation overpotential (Gabrielli *et al.*, 2005).

One of the important factors that affect the voltage balance of an electrolytic cell is the IR drop in the electrolyte across the anode-cathode gap (Hine *et al.*, 1980). The anode-cathode gap has been found to be the most significant parameter when it comes to the reduction of the electrolyte IR drop in a cell (Hine *et al.*, 1980). This is partly due to the fact that the anode-

cathode gap strongly affects the gas void fraction and subsequently the electrolyte conductivity and resistivity. In gas evolving electrolytic cells, the presence of gas bubbles dispersed in the electrolyte result in an increase in the electrolyte resistance and IR drop (Hine *et al.*, 1980). The electrolyte resistance varies due to the formation of gas bubbles (Sillen *et al.*, 1982).

The voltage drop across the electrolyte is proportional to the resistance of the electrolyte. The electrolyte resistance on the other hand is proportional to the inter-electrode distance and inversely proportional to the area of the electrode (Sandenbergh, 2014c). Equation 2-2 illustrates this relationship.

$$R = \rho \frac{l}{A} \tag{2-2}$$

where R is the electrolyte resistance, ρ is the electrolyte resistivity which is the inverse of conductivity, l is the inter-electrode distance and A is the area of the electrode.

Perforated electrodes have been shown to effectively remove the evolved gas bubbles from the electrolysis gap, hence, minimizing the IR drop by reducing the gas fraction in the anode-cathode gap (Hine *et al.*, 1980). Another way to minimize IR drop is by the recirculation of electrolyte. Circulating the electrolyte reduces the gas void fraction in the electrolysis zone. As a result, the conductivity of the two-phase electrolyte mixture in the electrolysis gap is improved and the electrolyte resistance reduced (Hine *et al.*, 1980). Electrolyte circulation also plays a role in the mass transfer and electrolyte mixing in a gas evolving electrolysis cells (Hine *et al.*, 1980). Therefore, optimizing this parameter may lead to an efficient and optimally operating electrolytic cell.

2.3.8. Cell configuration and electrode design

2.3.8.1. Electrode design

The electrode material and electrode geometry affect the maximum current density in an electrolytic cell (Sillen *et al.*, 1982). The electrode surface roughness on the other hand has a significant effect on the bubble population. This is due to the fact that a rough surface promotes more nucleation as compared to a smooth surface (Sillen *et al.*, 1982; Matsushima

et al., 2013). The bubble nucleation stage prefers to take place on the pits and scratches on which the electric field line converges (Matsushima *et al.*, 2013).

Nagai *et al.*, (2003) investigated the effect of electrode height on water electrolysis efficiency. Their findings showed that the electrodes with the larger height produced a higher void fraction between electrodes as compared to the smaller height electrodes. The larger electrodes have a greater surface area and the electrodes with a larger surface area possess lower resistance for the current flow (Mazloomi *et al.*, 2012). Furthermore, a lower current resistance can be related to higher currents and subsequently more gas bubble evolution. Therefore, high void fractions can be expected in systems with electrodes that have a large surface area as reported in Nagai *et al.* (2003).

Using vertical electrodes has been reported to yield higher efficiencies. This is due to a reduced ohmic resistance that is caused by an optimal higher bubble departure rate (Mazloomi *et al.*, 2012). The above studies are among the various studies that have been reported in literature which investigated different cell and electrode designs (Sillen *et al.*, 1982; Glas & Westwater, 1964). All these studies show that the electrode material, design and configuration have a significant effect in determining cell performance.

2.3.8.2. Inter-electrode distance

The inter-electrode distance is a significant parameter in determining the terminal cell voltage in an electrochemical cell. A narrow inter-electrode distance results in a reduction in electrolyte resistance which in turn causes a decrease in the electrolyte IR drop. This can be illustrated with reference to Equation 2-2 above.

Since R is proportional to L, reducing L will reduce R. Hine *et al.*, (1980) identified an optimal inter-electrode distance of 5-7 mm for the electrolysis of caustic soda; this was dependent on the operating conditions such as current density and electrolyte concentration. Another optimal distance between the electrodes was identified and it was found to be dependent on the current density (Nagai *et al.*, 2003a). This optimal distance measured was 1-2 mm which corresponded to a current density greater than 0.5 A/cm^2 in a water electrolysis system (Nagai *et al.*, 2003a).

When distance between electrodes is small and the current density high, the void fraction between the electrodes becomes high (Nagai *et al.*, 2003a; Abdelouahed *et al.*, 2014a). This

is because the high current density generates a large number of bubbles and since the electrode spacing is small the gas bubbles tend to accumulate quickly. A high gas void fraction in the inter-electrode gap increases the electrolyte IR drop by decreasing the conductivity and subsequently increasing the solution resistance and (Hine *et al.*, 1980). As a result, this causes a decrease in the cell energy efficiency as more energy needs to be supplied to overcome the increase in electrolyte resistance (Nagai *et al.*, 2003a).

An increase in the inter-electrode space results in a decrease in gas volume fraction but it also increases electrolyte resistance (Nagai *et al.*, 2003a; Abdelouahed *et al.*, 2014b). A narrow inter-electrode distance results in a reduction in internal cell resistance (Pletcher & Walsh, 1990a: 60-141; Mazloomi *et al.*, 2012). An optimal electrode-diaphragm configuration can lead to a reduced ohmic resistance (Sillen *et al.*, 1982). A reduced overall cell resistance results into reduced losses in the electrolytic cell. The optimal inter-electrode differs from system to system and it is an important parameter to identify and optimise.

2.4. Flow regimes in electrolysis cell

2.4.1. Types of flow and flow behaviour

Two-phase flow in an electrolysis cell is evident when there are gas bubbles forming and detaching from the electrode surface (Dedigama *et al.*, 2014). The rising gas bubbles causes shear forces that result in an upward liquid motion near the electrode surface (Vogt, 1978). The resulting gas-liquid flow forms a distinct flow field pattern that can be observed in the area near the electrodes. The flow field patterns come into effect as a result of the cell configuration, design and operating conditions.

The most commonly observed flow regimes in two-phase flow is bubbly flows, slug flows, churn flows and annular flows (Dedigama *et al.*, 2014; Ito *et al.*, 2010). The flow regime varies depending on the superficial velocity of each phase which is related to the mass transport (Dedigama *et al.*, 2014; Ito *et al.*, 2010). These different flow regimes are graphically shown in Figure 2.1. The type of flow regime that can be expected in the type of electrochemical cell investigated would be the bubbly flow.

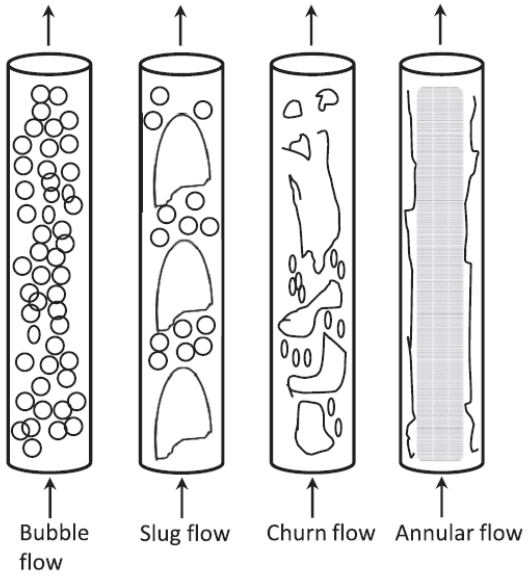

Figure 2.1: Different types of flow regimes in a vertical channel commonly found in two phase flow (Dedigama *et al.*, 2014).

Fluid flow in electrolysis cells is dependent on the evolution of gas bubbles at the electrode surface, which in turn depends on the cell design and configuration (Philippe *et al.*, 2005). One of the transport mechanisms of the electrolyte motion in a cell is due to the natural convection created by the gas evolution (Boissonneau & Byrne, 2000). In addition to the evolution of gas bubbles and detachment, the coalescence of bubbles adhering to the electrode surface causes a flow of the electrolyte solution (Janssen & Barendrecht, 1985). Shear forces caused by departing and rising bubbles along the electrode also contribute to the motion of the electrolyte solution (Vogt, 1978).

Fluid flow in electrolysis cells with bubble evolution can transform from a laminar to a turbulent behaviour throughout the length of the cell (Boissonneau & Byrne, 2000). Model predictions have reported similar transitions in the fluid flow, whereby it was predicted that the presence of small gas bubbles brings about a transition from a quasi-steady to a pseudo-turbulent regime in a cell with gas evolution (Alexiadis *et al.*, 2011).

Bubbly flows are evident at low current densities and as the current density increases the flow regime then changes to slug flow (Dedigama *et al.*, 2014). This change is partly due to the increase in the bubble population, speed and bubble size as the current density increases (Sillen *et al.*, 1982; Dedigama *et al.*, 2014; Mat & Aldas, 2005). Furthermore, this change in

flow regime has been shown to enhance mass transport as the electrolyte mixing and mobility of ions is enhanced (Dedigama *et al.*, 2014).

However, as the bubble population increases a layer or shield is formed at the electrode surface (Eigeldinger & Vogt, 2000; Boissonneau & Byrne, 2000; Matsushima *et al.*, 2013). Consequently, the reactive surface of the electrode and the cross sectional areas of pure electrolyte for mass and current transport are reduced (Eigeldinger & Vogt, 2000; Dahlkild, 2001). Therefore, mass transfer will increase until the point where there is bubble shielding and then it will eventually stop increasing. This again shows that current density plays a significant role in determining the flow patterns in gas evolving electrolysis cells.

When the supersaturation of dissolved gas in the liquid adjacent to the electrode surface is sufficiently high, gas bubbles form nucleation sites on the electrode surface (Dahlkild, 2001). When the sum of the buoyancy force of the gas bubbles and the shear forces of the liquid are greater than the interfacial tension force by which the bubbles adhere to the electrode surface, the gas bubbles leave their nucleation sites (Dahlkild, 2001).

2.4.2. Factors affecting flow patterns

2.4.2.1. Electrode design

Kim & Fahidy (1989) used different anode materials in their experiments and observed that the flow patterns generated at graphite, lead and durichlor 51 plate anodes of the same size were almost identical. It was further concluded that the anode material of construction is not an important factor for determining flow patterns (Kim & Fahidy, 1989). On the other hand, it was shown that the shape of the electrode affects the distribution of the electric current and hence, plays a significant role in determining the flow patterns (Kim & Fahidy, 1989).

In another study four different cathode materials were used and it was observed that the growth rate of gas bubbles is not affected by the electrode material (Glas & Westwater, 1964). In another study, five different electrode designs were used and different circulation patterns of the flow field for each of the electrode designs was observed (Ashraf Ali & Pushpavanam, 2011b). The maximum circulation and mixing was achieved with a configuration that included three small (1cm x 31cm) electrodes placed in parallel to one another and separated by a spacing of 3 mm (Ashraf Ali & Pushpavanam, 2011b).

These findings show that the combination of electrode design and configuration has a significant impact in determining the circulation flow patterns in electrolysis cells. Therefore, it can be expected that different electrochemical cells with unique designs and operating conditions will yield different flow patterns.

2.4.2.2. Current density and cell voltage

It has been shown that an increase in current density increases gas evolution (Sillen *et al.*, 1982; Aldas, 2004; Mat & Aldas, 2005; Glas & Westwater, 1964; Wüthrich *et al.*, 2005). The enhanced gas bubble evolution has an effect on the flow patterns since the fluid flow in gas evolving electrolysis cells is induced by gas evolution. Vogt (2012) noted that the bubble volume reached at departure from the electrode depends on the shape, size and direction of the operating electrode. Moreover, the bubble volume was shown to be largely affected by the conditions of the gas-liquid flow near the electrodes (Vogt, 2012).

An increase in voltage results in an increase in the current which then increases the production rate of the gas bubble. This causes an increase in circulation and consequently good electrolyte mixing (Ashraf Ali & Pushpavanam, 2011b).

2.5. Flow visualisation techniques

This section presents some of the widely used flow visualisation techniques. Flow visualisation is one of the most effective ways to analyse flow and it has played an important role in improving the understanding of complex fluid flows (Lim & Smits, 2000c: 1).

2.5.1. Direct flow visualisation

Direct flow visualisation can be used as a simple tool to establish a flow field as a basis for mathematical models (Kline, 1969). A number of studies in literature have used the direct visualisation technique to gain a better understanding of various aspects of the two-phase flow generated during electrolysis with gas evolution.

Direct observation of the two-phase flow with a high speed camera (Phantom Dantec Dynamics) was used to take photographs for the purpose of measuring bubble size, bubble velocity and gas volume fraction (Abdelouahed *et al.*, 2014a; Abdelouahed *et al.*, 2014b). The Matlab image processing tool was then used to analyse the images and also to convert

the real images to binary images for measurements and calculations (Abdelouahed *et al.*, 2014b).

Similarly, (Eigeldinger & Vogt, 2000) used a video camera to record the bubble population and diameter of adhering bubbles. The recorded videos were analysed with software and the fractional bubble coverage was also determined using the software.

Two cameras, one in each electrode were used to record bubble evolution during alkaline water electrolysis. The behaviour of the gas bubbles was recorded at a frame rate of 30 fps and the recordings were analysed offline using a computer (Zhang & Zeng, 2012).

A dark violet colour of electrochemically produced Mn (III) ions was observed using direct visualisation with the aid of a Canon video camera and still photographs were taken with a Nikon camera (Kim & Fahidy, 1989).

Microscopically enhanced visualisation was used to investigate the two-phase flow regime and measure bubble size inside a small electrolysis cell (Boissonneau & Byrne, 2000). The visualisation arrangement included a charge coupled device (CCD) video camera connected to a microscope on the front of the cell. A bubble counting method was used to measure bubble size and concentration.

A similar approach was used to study the growth of H_2, O_2, Cl_2 and CO_2 gas bubbles on platinum, nickel, copper and iron electrodes at constant current density (Glas & Westwater, 1964). Measurements of the gas bubbles were conducted using high speed motion picture photography through a microscope. Analysis of the motion pictures produced bubble size and the contact angle at electrode surface (Glas & Westwater, 1964).

Four CCD video cameras were used to observe the gas bubble formation at the electrode surfaces; two cameras per electrode were placed at a 30 degree angle to the electrode surface to avoid bubble screening (Mandin *et al.*, 2013). The cameras were used to gain direct visualisation of the bubbles in order to measure bubble diameter and population density during alkaline (NaOH) water electrolysis. The video sequences were decomposed to images and analysed using the Virtual_Dub software.

Matsushima *et al.*, (2013) studied the effects of a magnetic field on bubble evolution, growth and coverage. A high speed digital camera was used to gain visual access to the bubble evolution at the electrode surface at a frame rate of 2000 fps.

Dedigama *et al.*, (2012) conducted visualisation of bubble formation and flow patterns by using a high speed video system (Photron SA-5, Photron, USA) and a solarc light source for illumination. The images were captured at a frame rate of 7000 frames per second at a 1024 x 1024 resolution. The images were digitally analysed using Phantom camera control software.

These studies show evidence that indeed the technique has been widely used and trusted in studies involving two-phase flows. This technique is simple, relatively cheap and it gives out detailed information of the system studied. As a result, direct flow visualisation was chosen as the preferred method for this investigation.

2.5.2. Flow followers

The use of a flow follower is a technique commonly used to identify flow patterns. The movement of a particular particle is recorded and flow patterns are deduced from its trace. Flow followers can be simple particles which are made distinct by colouring and their movement is tracked visually and recorded with a camera (Mavros, 2001).

Flow followers in the form small, neutrally buoyant rhodamine coated particles of poly methyl metha acrylate were used to track flow fields and measure circulation times (Ashraf Ali & Pushpavanam, 2011b). Amongst other uses, the technique of using flow followers has been used to observe flow patterns or to measure circulation times, which were then used to validate the predictions theoretical models (Mavros, 2001).

Dye visualisation is another technique which has been widely used in flow visualisation studies (Lim & Smits, 2000a: 43-69). In the technique, a food dye is commonly used as the flow follower. Food dyes are used because they are safe to handle, easily accessible and come in various colours (Lim & Smits, 2000a: 43-69). In terms of the colour choice, it has been noted that the green, blue and red colours produce better picture contrasts compared to other colours (Lim & Smits, 2000a: 43-69).

2.5.3. Particle image velocimetry (PIV)

PIV is a technique that involves using a powerful light source for illumination and taking images of a plane cutting through the vessel at short time intervals. PIV is both a quantitative and qualitative technique. It has capabilities to use the captured picture frames to yield velocity vector components and to provide a map of the flow in the illuminated plane. Software is required to analyse the picture frames and use them to calculate the particle velocities (Mavros, 2001).

Recent software developments have resulted in very detailed flow maps and calculations of flow characteristics such as vorticity and turbulence amongst others (Mavros, 2001). Novel extensions of the PIV technique include the holographic PIV, which records the 3-D velocity distribution. Another extension is the three dimensional particle tracking velocimetry, in which all the three velocity vector components are determined as a function of time (Mavros, 2001).

Typically, PIV uses a set of lasers and cameras and provides instantaneous global views of the bubble layer behaviour along the electrodes (Boissonneau & Byrne, 2000). The technique has been used to visualize the global behaviour of a two-phase flow with a focus on finding the transition point where laminar flow transferred to turbulent flow (Boissonneau & Byrne, 2000).

Ashraf & Pushpavanam (2011) used PIV to quantitatively analyse the flow field in an electrolytic system. The electrolyte was seeded with tiny, neutrally buoyant rhodamine coated particles of poly methyl metha acrylate, PMMA (ρ=1000 kg/m^3, size 10 µm). Since the particles possessed similar densities as the electrolyte, they were assumed to follow the flow behaviour faithfully.

To conduct the measurements, a double pulsed Nd-YAG laser beam is passed through an optical arrangement in the system and the reflection from the particles is captured with a high speed camera. This allows one to obtain the velocities of the particle which then translates to the velocity of the liquid (Ashraf Ali & Pushpavanam, 2011b).

The PIV technique enables visual observation of fluid flow fields for qualitative flow analysis and as an added advantage it also has the ability to provide quantitative data. For this reason,

the PIV technique has been a very popular measurement tool in fluid flow investigations (Lim & Smits, 2000a: 43-69).

2.5.4. Laser Doppler Velocimetry (LDV)

The development of the laser technology in the 1960s resulted in a new measuring technique for velocities, the laser doppler velocimetry (Mavros, 2001). In the LDV technique, the measuring probe lies outside the vessel of interest and hence does not interfere with the flow pattern inside.

The working principles of LDV involves a laser beam splitting which results into two coherent beams that are made to cross at a point inside the vessel. In the intersection volume, parallel interference fringes are formed. When a particle crosses this small volume, it scatters light which is captured by a photodetector (Mavros, 2001).

The velocity of the particle crossing the intersection volume is measured by analysing the change in intensity fluctuations on the photodetector (Mavros, 2001). The LDV technique also has the ability to measure velocity vector components. The only disadvantage of the LDV technique is the need for the fluid to be transparent (Mavros, 2001).

Boissonneau & Byrne (2000) used LDV to measure the fluid and bubble velocities in the channel between electrodes at different heights along the length of the cell. The aerometrics LDV instrument used in the experiments separated green light (514 nm) from blue light (488 nm) and enabled a two component velocity measurement.

LDV uses light scattered from the bubbles to calculate velocity. Amongst the methods used in their experiments, (Boissonneau & Byrne, 2000) concluded that LDV was the most robust method for measuring the hydrodynamics of gas evolving systems.

2.5.5. Other techniques

There are some advanced techniques which have not been commonly used in flow visualisation but have been reported in certain studies in literature. These include nuclear magnetic resonance (NMR) imaging, neutron imaging, micro-tomography, and fluorescence microscopy. These techniques have mostly been used for liquid water visualisation in hydrogen fuel cells (Bazylak, 2009). Another advanced method that has been used in bubble

columns and crystallizers is the computer assisted radioactive particle tracking technique. An alternative to this is the positron emission particle tracking technique (Mavros, 2001).

2.6. Conclusions

Several design and operational factors that affect electrolysis performance and efficiency have been identified and discussed. These include gas bubble evolution, gas-liquid flow, mass transfer, current density, electrode configuration and design. Hence, every cell design will have a unique way in the manner in which it performs. With that said, it is important to have a thorough understanding of the effects caused by these factors on the cell performance. This is what this investigation is aiming to achieve in the system being investigated.

The most commonly used method for flow visualisation was found to be the direct flow visualisation technique. Direct flow visualisation is the simplest and cost effective way to observe fluid motion and provides valuable insight into the phenomena occurring in fluid flows. As a result, for the purpose of this work direct flow visualisation was chosen as it proved to be sufficient for the study at hand. Other powerful techniques such as PIV and LDV were considered; however, due to the financial constraints of the project these techniques were ruled out as options because they were not as cost effective as the direct flow visualisation technique.

Most of the work reported in the literature use a mathematical approach to study the operating parameters and associated factors in electrochemical systems. There are few studies that focus on experimental work to determine effects of design parameters on flow patterns and electrolysis cell performance. Hence, this study investigated the effect of a specific cell design on the flow patterns and cell performance. The effect of parameters such as the electrode configuration, electrode dimensions and current density on the flow patterns was tested.

3. EXPERIMENTAL SETUP

3.1. Introduction

The electrochemical cell that was used in the experimental work was based on a pilot plant scale electrochemical cell design for electrolysing a molten salt electrolyte. The aim of the laboratory scale cell was to verify the CFD model used for modelling the pilot plant scale electrochemical cell. The focus was on the gas bubble induced electrolyte flow patterns around the anode and the factors that affect the electrolyte flow. Hence, the laboratory scale cell was designed to simulate the pilot plant cell, particularly the electrolyte flow patterns.

There were notable differences between the two systems, as the pilot plant cell was designed for molten salt electrolysis and the laboratory scale cell was designed for the electrolysis of an aqueous solution. The main differences in the two systems were the applied current density, electrolyte, electrolyte conductivity, amount of gas evolved, and temperature. Despite the differences between the two systems, the laboratory cell was still a good physical model that would provide valuable insight on the operation and design of the cell investigated. This is mainly because the physical cell designs had a lot of similarities. Since the design and configuration of the two cells was similar, the resulting flow patterns were expected to be similar too. Hence, the laboratory scale cell design provided a good model to simulate the pilot scale cell and test the CFD model even though it was operated in a different electrolyte.

Due to the fact that not all the factors and parameters were emulated in the laboratory cell, some trade-offs were made in the design of the laboratory cell. The parameters that were considered in the cell design were the physical properties of the electrolyte, cell dimensions and configuration, gas evolution, current density and cell voltage. The laboratory cell was designed such that the cell configuration was similar to the pilot cell as this affects the electrolyte flow patterns. Moreover, the cell was designed such that the amount of gas evolved was appreciable and can lead to similar flow phenomena observed in the pilot plant cell.

3.2. Electrolysis cell design

Figure 3.1 below presents the design drawing of the electrolysis cell used in the experimental work for this investigation. The electrochemical system included a transparent electrolysis cell, electrodes, diaphragm, and supporting structure.

The cell consists of a supporting structure which houses the electrolysis cell in place with all the cell components attached to it. Because of the size of the electrolysis cell, the supporting structure was designed to enable ease of handling and transportation of the cell. The inner components of the electrolysis cell i.e. anode, cathode and diaphragm were required to be adjustable within the cell. For that reason, the supporting structure was designed to have rails at the top to allow for the anode, cathode and diaphragm to be moved horizontally in order to adjust the distances between them as required in the experimental work. The supporting structure also allowed easy removal of the electrode and diaphragm from the cell.

The diaphragm can also be removed and replaced with a different diaphragm design to test the effectiveness of the diaphragm type used in relation to separating the anode gas bubbles from entering the cathode half. However, only one diaphragm design was tested in this study.

The electrodes were attached to hangers which were electrically isolated; these are presented by label 3 in Figure 3.1. The electrode hangers were positioned on the rails of the supporting structure. This enabled the electrodes to be moved on the rails to adjust the inter-electrode spacing and also interchange the electrodes when required.

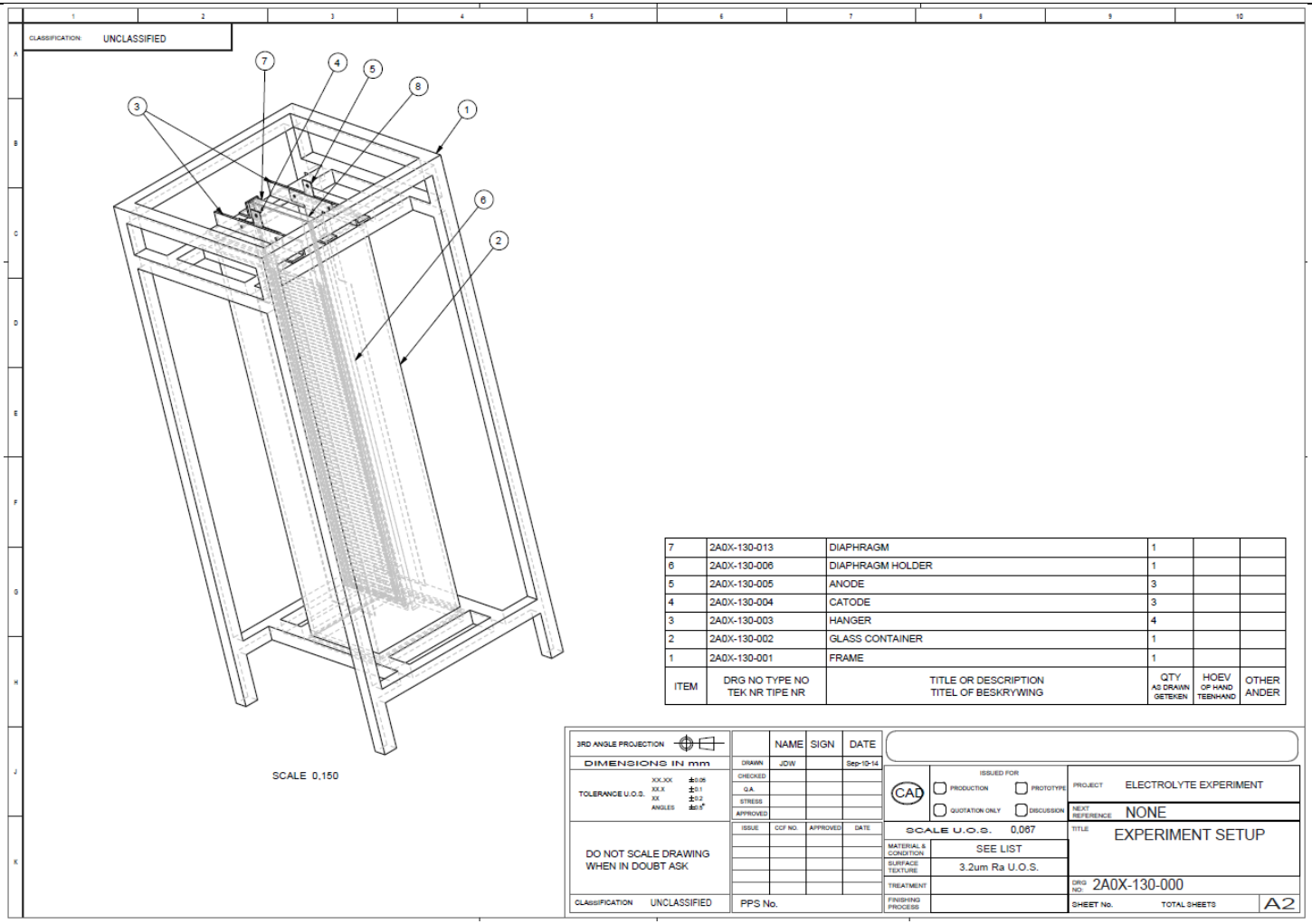

Figure 3.1: Design drawing of the electrolysis cell design

Figure 3.2 presents a schematic diagram of the experimental setup which included the electrolysis cell as shown in Figure 3.1, aqueous electrolyte solution, a high speed camera connected to a laptop and a DC power supply. The high speed camera system included external lights and tripod stands. The set up arrangement included the high speed camera positioned on the front side of the cell with the tripod stand used to adjust the camera level of view and angle. The external lighting was positioned from the top, back and on the side of the cell.

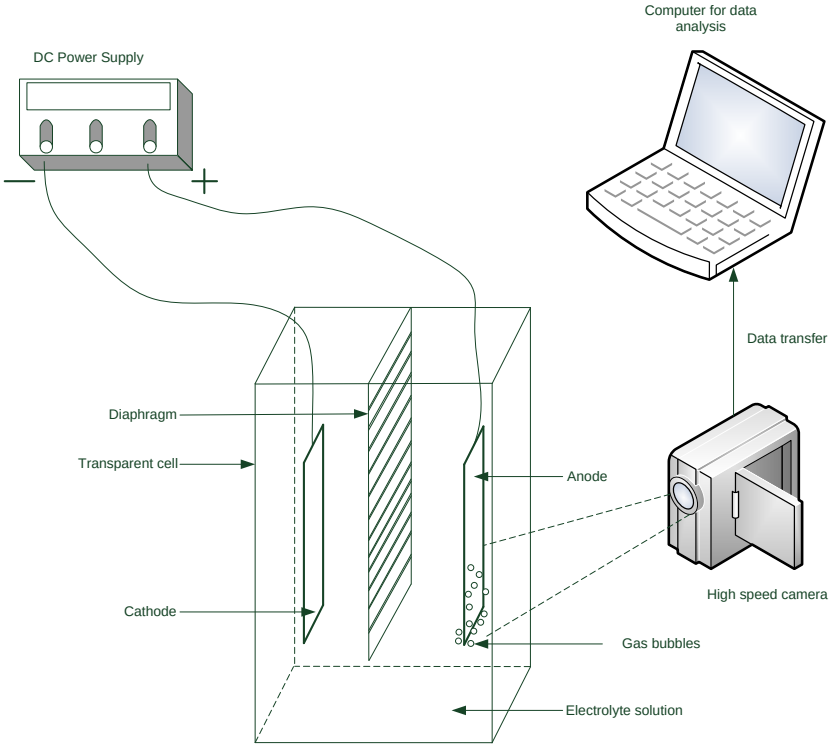

Figure 3.2: Schematic diagram of the experimental setup

Figure 3.3 shows a photograph of the experimental setup, indicating some of the key components of the setup. Further details of each of the components of the cell are presented in the following subsections.

Figure 3.3: Photograph of the experimental setup with all its components

3.2.1. Anode

The anode is an important element in the electrochemical system; it is the electrode at which the oxidation reaction occurs (Sandenbergh, 2014c). In this electrochemical system, the oxidation of water to O_2 occurs at the anode and oxygen gas bubbles are evolved at the anode surface.

The oxidation half-cell reaction follows the following reaction equation;

$$2H_2O \leftrightarrow O_2 + 4H^+ + 4e^-$$

The O_2 gas evolved at the anode surface induces a two-phase flow pattern in the space next to the surface of the anode. The focus of this study was to observe, measure and analyse this two-phase flow in particular and how it contributes to the electrolyte circulation around the anode. It was therefore essential to get an appreciable amount of gas evolution and subsequent electrolyte circulation for observation and analysis. For this reason, the anode was designed in such a way that it will enable large enough currents to generate large amounts of O_2 gas bubbles. This is due to the fact that the amount of gas produced is proportional to the applied current density.

One side (backside) of the anode was coated with an epoxy resin to isolate that side from the electrolyte. This was done to ensure gas evolution occurred only on one face of the anode and prevent any gas generation on the backside of the anode. Any gas at the back of the anode would subsequently affect the electrolyte circulation around the anode. Therefore, it was important to eliminate it in order to effectively study the electrolyte circulation caused by the O_2 gas evolution at the electrode surface facing the cathode.

When designing this electrochemical system it was desirable to have an anode that was a good conductor of electricity to limit IR losses, and also a low overpotential for the water oxidation to O_2 reaction in order to reduce the energy requirements of the electrochemical reaction (Sandenbergh, 2014c). The aqueous solution selected for this investigation was copper sulphate. Lead alloys are typically used as anodes in industrial copper electrowinning plants. The popular Pb-6%Sb alloy was considered as a possible anode material. However, due to procurement challenges in the acquisition of this alloy, it was not used as the anode. As a substitute for the lead alloy, a 304 stainless steel was used as the anode. The 304

stainless steel was chosen because it is a good electrical conductor which means low voltage drop across the anode, has high corrosion resistance and would be able to withstand the corrosive nature of the anodic reaction which produces acid.

Three different sized anodes were investigated in this study and this was to test the effect of the anode height on the electrolyte flow patterns and circulation. Figure 3.6 shows the design drawing for the different sized anodes which were initially used in the experimental work. The design for the three anodes used was the same; the only difference was the height. However, after the commissioning of the electrochemical system it was observed that this anode design had some restriction to the electrolyte flow. The flow restriction was mainly due to the middle part of the anode which acted as the hanger and electrical connection. This middle part was blocking a significant portion of the electrolyte and gas bubbles from circulating around the top of the anode. This flow restriction was not desired and hence the anode design had to be changed. Figure 3.4 shows a photograph of the initial anode design that was modified.

Figure 3.5 shows a photograph of the modified anode design. The design drawings for the modified anode design are presented in Figure 3.7. The difference in this design is that it had the hangers running next to the cell wall and hence opening up the space in the middle to allow the electrolyte circulation and gas bubbles to flow freely at the top of the anode. The modified anode was made to cover the entire the width of the cell, i.e. 300 mm to eliminate electrolyte circulation from the side of the anode. The anodes were laser cut to ensure that they were cut to the specified dimensions. The thickness of all the electrodes was 6.5 mm.

Figure 3.4: Photograph of the initial anode design

Figure 3.5: Photograph of the modified anode design

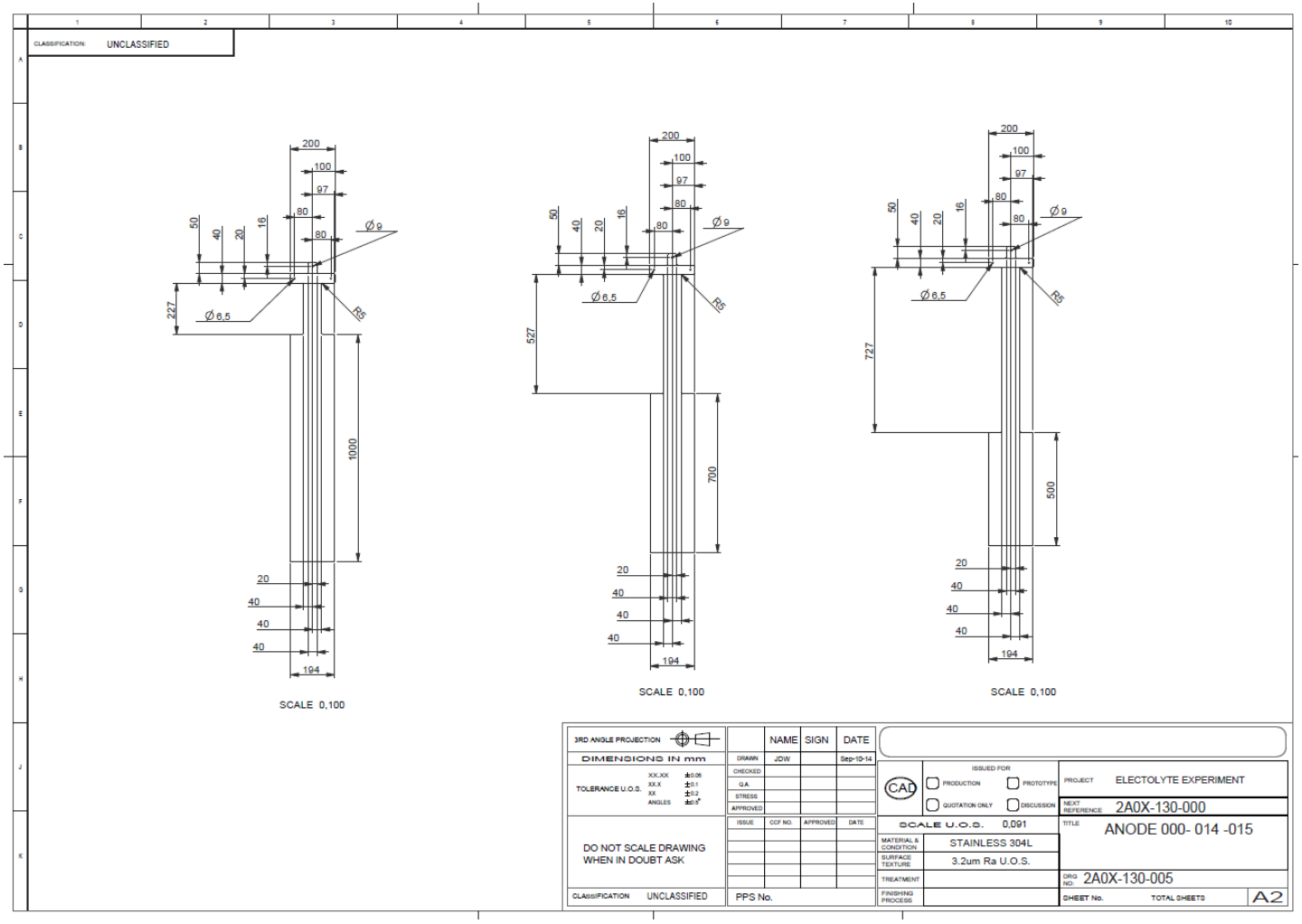

Figure 3.6: Design drawing of the initial anode for the three anodes of different lengths

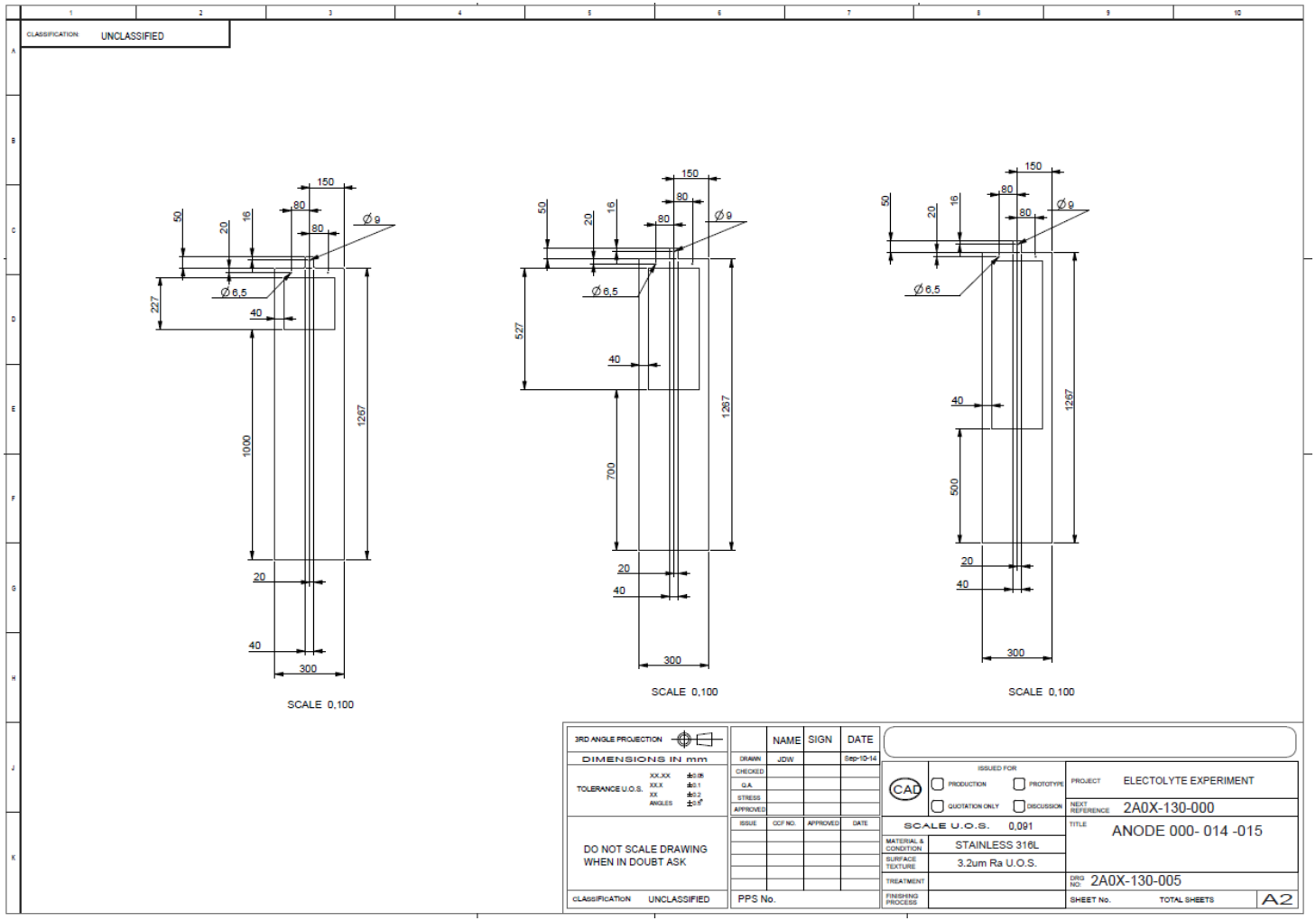

Figure 3.7: Design drawing of the modified anode design for the three anode sizes tested

3.2.2. Cathode

The reduction of copper ions in solution to form the copper metal occurs at the cathode surface.

The reduction half-cell reaction follows the following reaction equation:

$$Cu^{2+} + 2e^{-} \leftrightarrow Cu_{(s)}$$

As with the anode, the cathode material was required to be a good conductor of electricity, have a low overpotential for the copper reduction reaction, have a high overpotential for the hydrogen evolution reaction, i.e. the substrate should not promote the evolution of H_2 gas at the cathode as this would reduce the current efficiency of the cell (Sandenbergh, 2014c).

For this system, the 304 stainless steel grade was used as the cathode. Typically, the 316L stainless steel grade is used in the industrial electrowinning of copper, however, in this study the copper plating was not a critical component, hence, the 304 stainless steel was chosen.

Figure 3.10 shows the design drawing for the initial cathode design used in the cell. The initial design of the cathode was similar to that of the initial anode before the modification. A photograph of this cathode design can be seen in Figure 3.8. However, when the anode design was modified the cathode design was also modified. It was made to extend throughout the width of the cell to eliminate any electrolyte circulation around the cathode. Figure 3.9 shows a photograph of the modified cathode design. Figure 3.11 shows the design drawing for the modified cathode.

Figure 3.8: Photograph of the cathode design used initially

Figure 3.9: Photograph of the modified cathode design

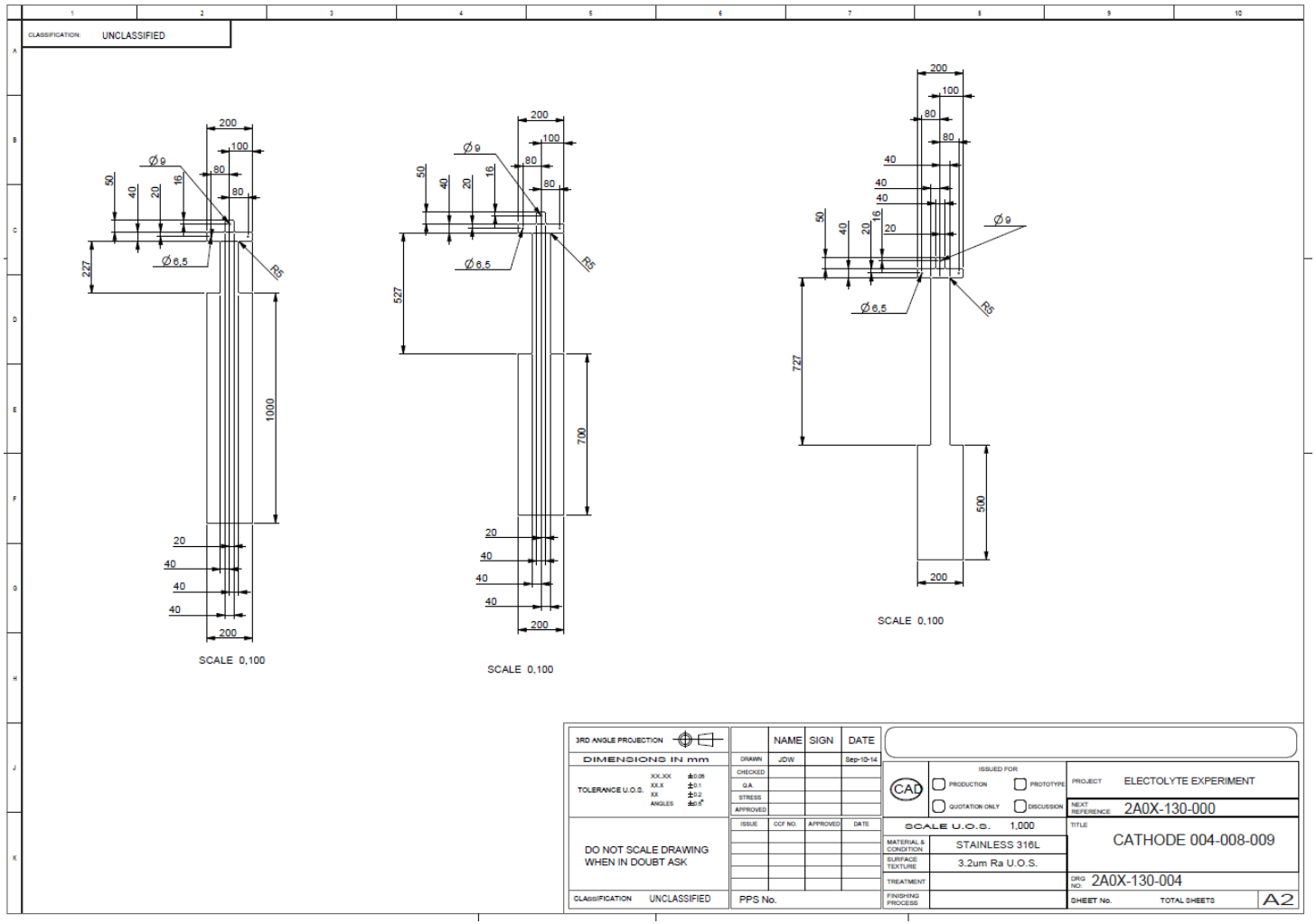

Figure 3.10: Initial cathode design drawing

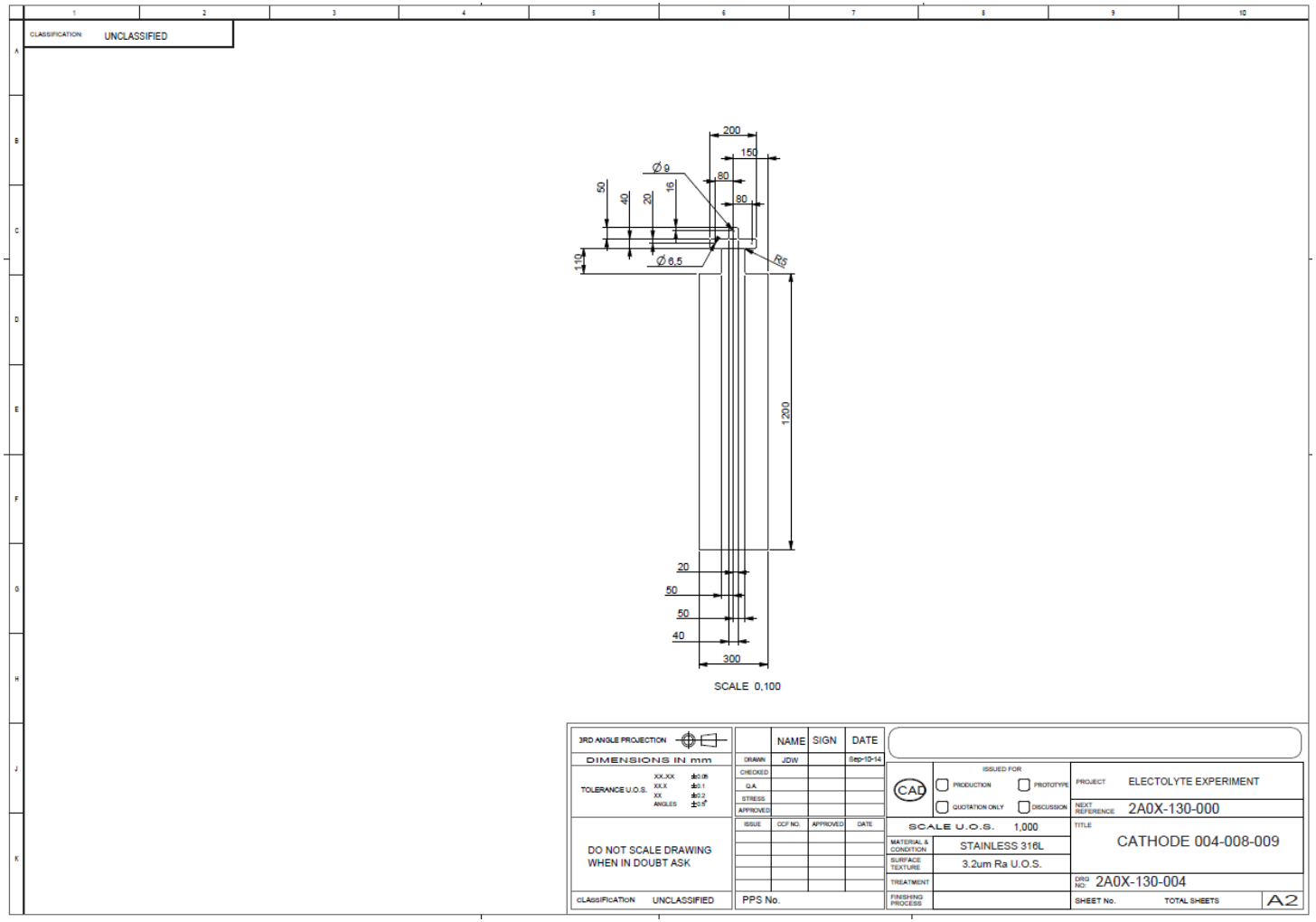

Figure 3.11: Modified cathode design with an increased length and width

3.2.3. Diaphragm

In the pilot electrolysis cell design, it is desirable to have the products from the anode half separated from the cathode half. Therefore, a particular diaphragm design was used in order to investigate the effectiveness it had in preventing the transport of the gas bubbles generated at the anode from entering the cathode compartment. Separating these two products is important because the gas may re-oxidize the plated metal to form the original reactant and this significantly reduces the current efficiency of the system. Figure 3.12 shows the photograph of the diaphragm design after construction. Figure 3.13 presents the design drawing of the diaphragm which was used in the study. This diaphragm was designed to allow only the electrolyte to circulate through the diaphragm slots and to disengage the gas bubbles as they rise up, to prevent them from entering the cathode half.

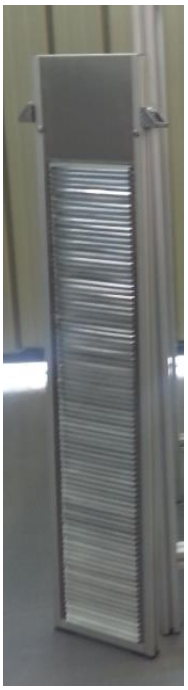

Figure 3.12: Photograph of the diaphragm design

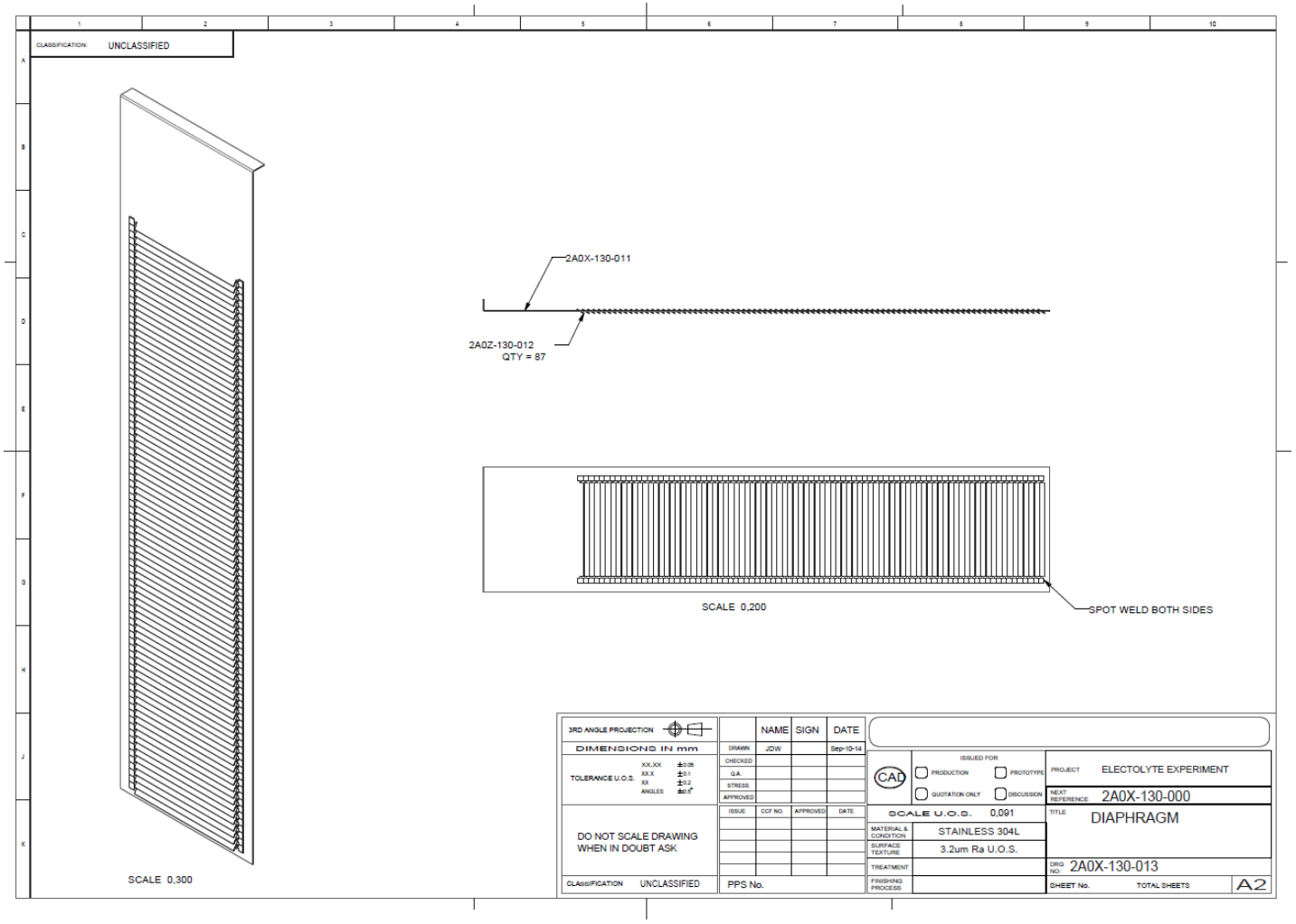

Figure 3.13: Design drawing of the diaphragm tested

3.2.4. Power supply

Electrochemical reactions are driven by the application of an electric potential to facilitate the chemical conversions. The external applied potential is used to overcome resistances to electron flow in electric conductors, spontaneous tendency of the reactions, charge transfer resistance and resistance to ionic conductance in the electrolyte (Sandenbergh, 2014a). The power supply used for this system was required to supply the voltage required for the electrowinning of copper from a copper sulphate solution.

One parameter that was investigated in the study was the effect of the current density on the electrolyte flow patterns and circulation rates. Three different current densities were applied; these were 50, 100 and 150 A/m^2. The capacity of the power supply used determined the maximum voltage and maximum current that could be applied. The actual current is a function of the applied voltage and the total resistance of the system. The power supply that was used had a maximum voltage of 10 V. The conversions between the current density and current were calculated by using Equation 3-1 below.

$$CD = \frac{I}{A} \tag{3-1}$$

where *CD* is the current density, *I* is the current and *A* is the area of electrode.

3.2.5. Transparent electrolysis cell

Since the study involved optical visualisation of the electrolyte flow patterns inside the electrolysis cell, the cell was required to be transparent. Glass was chosen as the transparent material of construction for the electrolysis cell. Clear float glass was used because it has good transparency, strong, non-conductive and corrosion resistant. The total volume of the cell and solution was relatively large, as a result 8 mm thick glass was chosen. The glass was glued together with silicon and since the glass thickness was relatively large it was easy to apply the silicon and tightly gluing the glass together. Figure 3.14 shows the electrolysis cell after the glass was glued together with silicon and inserted in the supporting frame.

Figure 3.14: Transparent electrolysis cell made of glass

3.2.6. Aqueous electrolyte solution

In the molten salt electrowinning process which was simulated in this investigation, there is gas evolution on the anode surface and molten metal production on the cathode. This experimental setup was designed to emulate the molten salt electrowinning cell by using an aqueous solution as the electrolyte in the physical model. The volumetric rate of molten metal production in the molten salt electrowinning process is relatively small (several hundred times less than the volumetric rate of gas production) and hence contributes very little compared to the gas in causing the electrolyte flow. The aqueous solution was therefore required to have metal production and gas evolution at the cathode and anode respectively. Furthermore, the aqueous solution was required to be transparent or at least allow a decent amount of optical visibility for observation of the flow patterns.

Three solutions were identified to have the potential qualities stated above and these were $CuSO_4$, $ZnSO_4$ and $CuCl_2$. These solutions were tested for transparency and the amount of gas evolution at the anode surface. All the solutions were prepared to be 1 M in concentration and tested in a small laboratory electrolysis cell. The small custom made electrolysis cell consisted of 500 ml glass beaker, graphite plate electrodes, small power supply and the 1 M electrolyte solutions.

The $ZnSO_4$ formed a transparent solution; it was clear and allowed good optical visualisation. The 1 M solution was electrolysed and there was a good amount of gas bubbles generated at the anode and Zn plating at the cathode. However, the problem with the Zn solution is that there is also H_2 gas evolution which is a major competing reaction at the cathode. Furthermore, Zn has a low exchange current density for hydrogen evolution so once the first layer is plated the Zn favours the H_2 evolution reaction (Sandenbergh, 2014b). As a result, there was Zn plating and H_2 gas evolution which was not desirable for the system investigated and thus the $ZnSO_4$ was eliminated.

The $CuCl_2$ formed a green cloudy solution; this was not clearly visible. The $CuCl_2$ solution was very cloudy and as a result it was very hard to observe what was happening inside the cell. The chlorine gas evolved at the anode presented another challenge as it was going to require some form of handling, possibly a gas scrubber or operating under a fume hood. For this reason, the $CuCl_2$ was ruled out as a potential solution to be used in the experimental work.

The $CuSO_4$ formed a blue solution; however, the 1M concentration prepared was clear enough to allow optical visualisation. The 1 M solution of $CuSO_4$ was electrolysed and it was found to generate an appreciable amount of gas bubbles and it was clear enough to observe the gas bubbles and the electrolyte flow. This was good for the purpose of this investigation. The copper sulphate solution proved to be the best option as it satisfied all the requirements for the desired electrolyte.

The 1 M concentration used in the laboratory experiments was very concentrated and going towards a dark blue colour. It was decided to reduce the concentration of the solution and use a similar concentration as used in industrial copper plants. A 100 g/l $CuSO_4$ solution was prepared and stored in a separate container. The solution was prepared in batches in a 20L container whereby it was stirred until fully dissolved and then transferred to the storage container.

3.2.7. Supporting structure

The supporting frame for the electrolysis cell was designed to provide a supporting base for the cell and to ensure ease of operating and handling of the cell. The electrolysis cell sits on the bottom of the supporting frame with the electrodes and diaphragm hanging from the top

and also supported by the frame. The supporting structure was made from aluminium and this was chosen as the MOC because aluminium is light in weight so the cell can be moved around with relative ease and it does not rust quickly. Figure 3.15 shows the supporting frame after the construction was completed. At this stage the glass was being glued together separately and once glued was slotted in its place at the centre of the frame. Figure 3.16 illustrates the design drawing of the supporting frame.

Figure 3.15: Photograph of supporting frame after construction

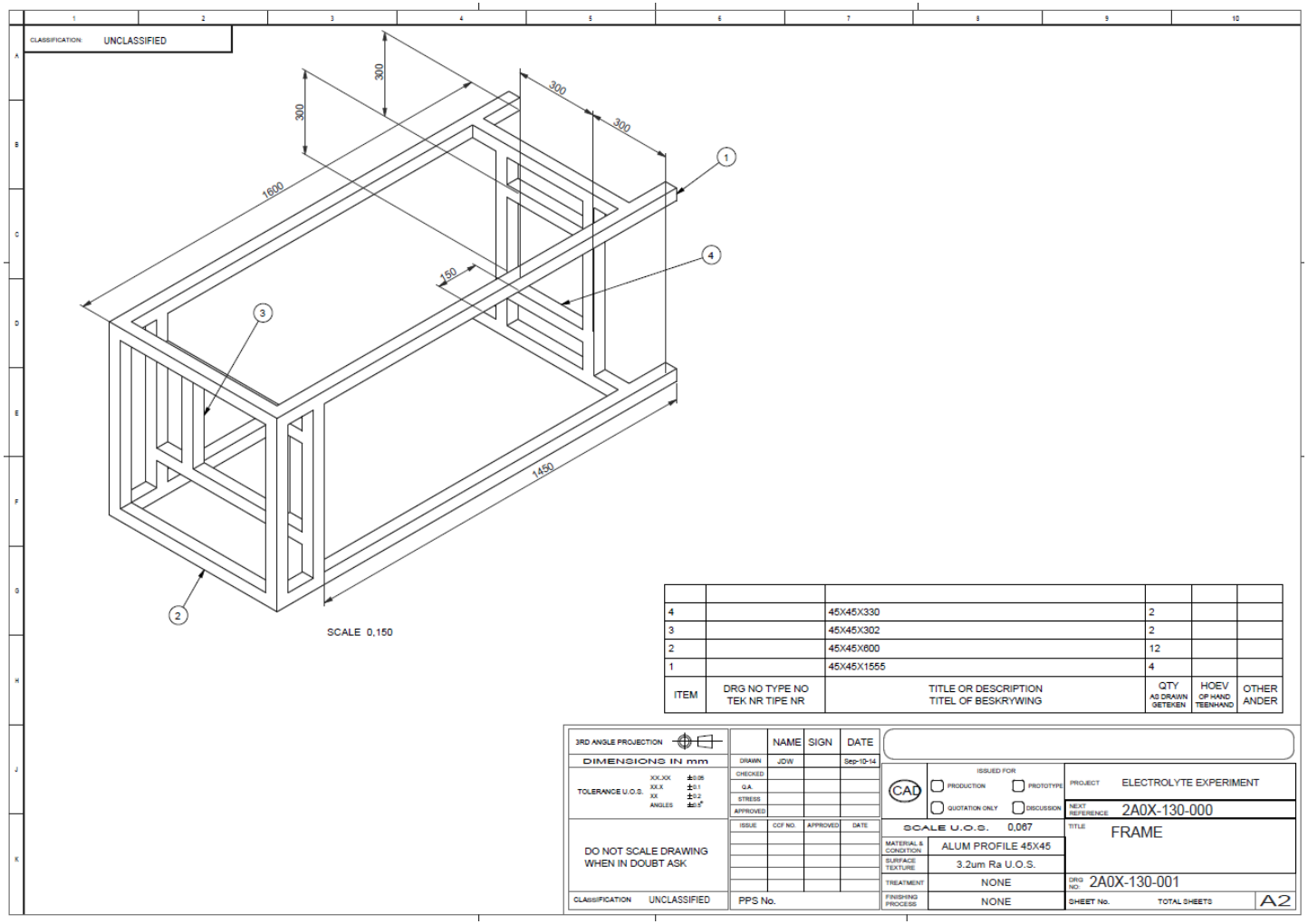

Figure 3.16: Design drawing of the supporting structure

3.3. Flow followers selected

One of the areas of interest in the electrolysis experiments was the electrolyte flow patterns at the bottom of the anode. This was the region where the electrolyte circulation could be observed. However, the circulation pattern could not be observed clearly as the motion of the electrolyte was not visible. As a result, there was a need to use flow followers in this region in order to clearly indicate the electrolyte circulation at the bottom of the anode. Two options were considered as flow followers, namely food dye and seeding particles. After a few laboratory tests, the food dye was ruled out. This was because, once injected into the electrolyte the food dye quickly disperses and does not track the flow field accurately. A review of a number of seeding particles used in flow visualisation studies was done. These included polyamide seeding particles, hollow glass spheres, solver coated glass spheres and fluorescent polymer particles. The flow followers were required to have the same density as the electrolyte solution in order to give an accurate account of the flow fields observed.

The flow followers that were used in this study were polyamide seeding particles (PSP) which are produced by a polymerisation process and thus have a round but not exactly spherical shape. These seeding particles are highly recommended for use in water or liquid flow applications as the density of the PSP is 1.03 g/cm^3 which is approximately the density of water. The polyamide seeding particles had a size distribution of 30-70 microns with a mean diameter of 50 microns. The PSP have a density of 1.03 g/cm^3 which was consistent with the density of the 100g/l copper sulphate solution (1.06 g/cm^3) which was used as the electrolyte.

The seeding particles were dispersed and suspended in electrolyte solutions prior to use in the experimental work. Because of the small size of the PSP tracking particles, they were visually in the form of agglomerated powder. This made it difficult to disperse the particles in the electrolyte solution as the particles were adhering together in agglomerates and were extremely hydrophobic. Ultrasonication was used to disperse the PSP tracking particles in the electrolyte solution. The ultrasonication device used was a Hielscher ultrasound technology UIP500hd sonicator. Since the PSP tracking particles were extremely hydrophobic, sodium dodecyl sulphate was used as a surfactant to reduce the surface tension and allow more dispersion. Applying the surfactant and ultrasonication was successful in dispersing the particles to form a homogenised dispersion with no agglomerates.

The PSP tracking particles were added into a beaker containing the electrolyte solution. Thereafter, a small amount of the surfactant was added in a trial and error manner into the solution containing the PSP particles. The addition of the surfactant partially dispersed the particles; however, it was not enough as the solution contained agglomerates. Figure 3.17 shows a photograph of the system used for dispersing the PSP particles in the electrolyte solution.

Figure 3.17: Photograph of the sonicator with dispersed solution

3.4. High speed camera system

A Photron FASTCAMSA4 high speed camera was used to record the gas bubbles and electrolyte flow patterns during the experiment work. The FASTCAM SA4 high speed camera comes with a high performance CMOS sensor technology which provides 3600 frames per second (fps) when operating at 1024 x 1024 pixel resolution. This high speed camera can go up to a maximum frame rate of 5000 fps. It is worth noting that with an increase in the frame rate there is a reduction in the resolution and consequently the quality of the images. Figure 3.18 shows an image of the high speed camera used in the study. Further details of the FASTCAM SA4 can be found in Appendix A.

Figure 3.18: Image of the Photron FASTCAM SA4 high speed camera

3.4.1. Lens

The lens was another important element of the setup because it determined the quality and clarity of the high speed video recordings. The lens was mainly used to adjust the focus and zoom of the image. A Nikon Micro-Nikkor 55mm f/2.8 was used in the high speed camera. The lens has high magnification ratio imaging which allows high quality performance at short focusing range. Figure 3.19 shows an image of the lens used in the experimental work.

Figure 3.19: Micro-Nikkor 55mm f/2.8 lens

3.4.2. Lighting

Proper lighting is one of the most important aspects of any photography (Lim & Smits, 2000a: 43-69). The lighting was an important feature of the camera setup as it contributed a lot to the quality of the recordings. Generally, gas bubbles can be observed with the naked eye; however, good illumination is required to create clear, definitive visualisation images that can be photographically recorded and analysed (Lim & Smits, 2000b: 27-41). For this reason, an array of super bright LED lights was used in the camera setup. The camera and the lens were very sensitive to the light; as a result, additional lighting was required to illuminate the areas of interest within the electrolysis cell. A series of super bright LED array technology was used to provide the high intensity illumination required for the high speed video imaging. High speed cameras require high levels of light for millisecond and microsecond shutter speed. Figure 3.20 shows the LED lights that were used in the camera setup.

Gas bubbles are most effectively illuminated by using angled back lighting of the bubble sheet (Lim & Smits, 2000b: 27-41). The brightness of the illuminated gas bubbles is a function of the angle formed between the axis of illumination and the line of sight of the camera (Lim & Smits, 2000b: 27-41). These factors were all considered while setting up the lighting. There are other factors that affect the illumination of the focus areas and subsequently the quality of the recordings. These include but are not limited to the visual access, background, test section being viewed, external illumination, type of camera etc. To optimize the illumination from the additional lighting, a trial and error approach was used until a satisfactory image was obtained.

Another critical factor in the lighting was the background. Regardless of the viewing direction and angle, the presence of a sharply contrasting background is important to capture good quality images (Lim & Smits, 2000b: 27-41). Typically, a high image contrast is achieved by using a black background (Lim & Smits, 2000b: 27-41). Taking into account the electrolysis cell setup and the available space, the black background was achieved by using black plastic bags. These were attached to the supporting frame of electrolysis cell by using a sticky tape.

Figure 3.20: The 4x6 and 3x4 super bright LED lights used in the camera setup

The super bright LED light arrays were connected to an AC and DC controller. The AC controller worked well as it was directly connected to the power supply; the DC controller on the other hand had to be charged after four hours of high intensity usage. There was only one of each of the controllers available for use; hence, both of them were used for the LED lights in the setup. Figure 3.21 shows a representation of the controllers used in the camera setup.

Figure 3.21: An AC and DC controller was used to power the LED lights

3.5. Parameters tested

To achieve the objectives and aims of this study, the following parameters were tested and their subsequent effects on the flow patterns were observed and measured. The tests included a base case as a comparative basis for the parameters investigated. Certain parameters were changed while keeping others constant. The parameters tested were the current density, inter-electrode spacing and anode height.

Current density

The current density was an important factor in determining the amount of gas bubbles evolved and thus had an effect on the subsequent electrolyte flow patterns and circulation. In this investigation the current density was changed from a 50, 100 to150 A/m^2 to study the effect it had on the flow patterns.

Inter-electrode distance

While keeping the other parameters constant at the base case conditions for the investigation, the inter-electrode distance was changed from 80 mm, 90 mm to 100 mm.

Electrode height

While keeping the other parameters constant at the base case conditions for the investigation, the electrode height was changed from 500 mm, 700 mm to 1000 mm.

Seven cases were tested in the experimental work. Table 3.1 presents the summary of the conditions that were tested. These cases include three main parameters, which are the current density, electrode height and inter-electrode spacing. A base case was established and the three parameters were changed in relation to the base case. Only one parameter was changed at a time for each of the cases tested, keeping the other parameters constant and consistent with the base case.

Test 1 and Test 2 involved the change in current density and the current density change was 50 A/m^2, 100 A/m^2 and 150 A/m^2 with the base case current density at 100 A/m^2. Test 3 and 4 involved the change in the anode height. Three different anodes were used in the experiments, with anode heights of 500, 700 and 1000 mm. The base case anode height was 700 mm. Test 5 and 6 involved the change in inter-electrode spacing and this varied from 80, 90 and 100 mm spacing with 90 mm the base case spacing.

Table 3.1: Summary of experimental conditions tested

Tests	Current density (A/m^2)	Anode height (mm)	Inter-electrode gap (mm)
Base case	100	700	90
Test 1	**50**	700	90
Test 2	**150**	700	90
Test 3	100	**500**	90
Test 4	100	**1000**	90
Test 5	100	700	**80**
Test 6	100	700	**100**

Diaphragm design

As stated above, the diaphragm design was tested to investigate its effectiveness in disengaging the bubbles formed at the anode and prevent them from entering the cathode half.

3.6. Experimental procedure

This section presents the experimental setup and the procedures used in setting up for the experimental work.

Camera setup

The critical part of the experimental work was obtaining good quality high speed video images in order to achieve good analyses of the flow patterns. The high speed camera setup included the positioning, lighting, image adjustment and calibration. The camera was placed in four different focus areas; these were Position A, Position B, Position C and Position D. The details of these positions are presented below. The lights were then connected and mounted in the required position. Thereafter, the camera zoom, focus, resolution, frame rate, shutter and lighting were adjusted until a good quality clear image was observed. The image adjustment step was both the most challenging and important step because it determined the quality of recordings and the post analysis of the recordings. The image adjustment was mostly done by trial and error until a good quality image was obtained.

Before any recordings were taken the camera was placed in the desired focus area and a camera calibration was done. The calibration was done by placing a ruler in the focus area and recording it. This was a way of measuring the actual distance covered by a single pixel of the image. The calibration was very important because it was used in measuring the bubble sizes as well as the bubble speed.

When recording at the top part of the electrolysis cell, a right angle illumination was used whereby the lights were positioned on the top of the cell above the flow field and the camera was positioned in front of the cell forming a right angle with the lights. When recording in the middle part of the cell, front and back illumination was used where by the lights were positioned at different angles on the front and back of the cell. A similar setup was used when recording at the bottom of the electrolysis cell. Below are the details of the camera positions used during the experimental work.

Position A

Position A represents the top front side of the anode. Figure 3.22 shows the location of Position A within the electrolysis cell. The camera was placed on the front of the cell at an angle and focusing on the front face of the anode where the arrow for Position A is pointed.

Position B

Position B represents the area slightly above the anode and between the left wall of the cell and anode backside. This is the area where the gas bubbles generated on the anode face accumulate and form a circulation flow pattern. Figure 3.22 illustrates the location of Position B within the cell.

Position C

The camera was placed in Position C to observe the behaviour of the electrolyte at the bottom of the cell. The PSP tracking particles were used in this region as the flow followers because there were no gas bubbles in the region under the anode. The electrolyte was expected to form a circulation loop around the bottom of the anode. Figure 3.22 illustrates the location of Position C at the bottom of the cell.

Position D

The gap between the anode and diaphragm was represented by Position D. The camera was placed here to observe whether or not the gas bubbles move through the diaphragm and cross over to the cathode half. Most of the gas bubbles are produced at the top part of the anode and hence, Position D was at the top part of the anode. Figure 3.22 illustrates the location of Position D within the electrolysis cell.

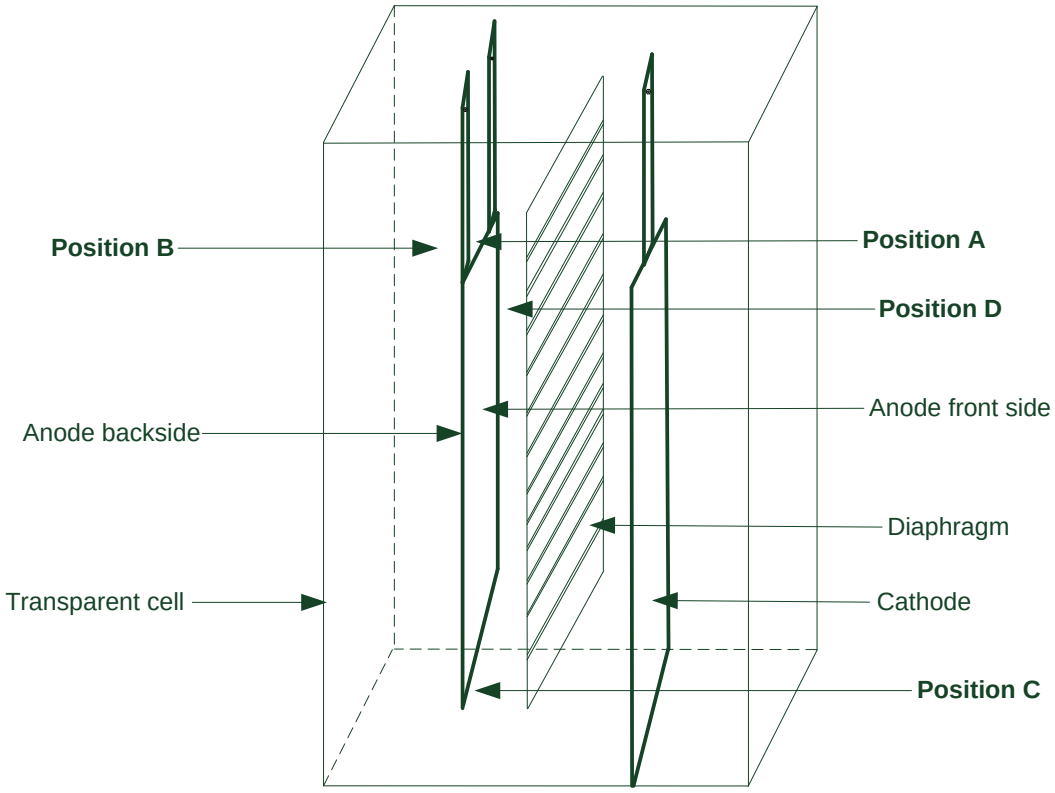

Figure 3.22: Full view of the electrolysis cell with the labels of camera positions. Positions A, B, C and D are clearly labelled in bold

Electrolysis cell setup

The electrolysis cell setup included the placement of the inner components of the cell. This included the electrodes, diaphragm and electrolyte. A measuring tape was used to measure the inter-electrode distance and also to align the diaphragm to the centre of the cell. Once the electrodes and diaphragm were aligned and the distances measured, they were tightened in their positions using the screws on the supporting frame. The desired electrolyte level was measured and marked on the cell. Thereafter, the electrolyte was transferred from the storage

container to the cell. The next step was to connect and tighten the power supply cables to the correct electrode.

The stepwise procedure that was used for setting up the system for experiments and data collection is as follows:

- Setup electrolysis cell (inter-electrode gap and anode height)
- Transfer solution to electrolysis cell
- Check power supply is disconnected
- Connect power supply cables and adjust to desired set points
- Setup the camera system
- Switch on the camera and computer
- Start the Photron FASTCAM viewer (PFV) software
- Position camera and lighting in the desired focus area
- Adjust the image settings by using PFV and the high speed camera lens
- Calibrate the camera in the selected position
- Adjust the camera lenses, focus, zoom, shutter rate, fps and resolutions until a clear image is obtained
- Initialise recording on the PFV software
- Edit the comments on the software to capture the details of the parameter tested
- When required, inject seeding particles into the area of interest. The seeding particles were mainly used to observe the circulation at the bottom of the anode.
- Record and save
- View and analyse the data using the PFV software

Current density test

The procedure for the current density test was the same as above. Since different current densities were tested, the additional step was to adjust the voltage supplied until the desired current was achieved for a particular current density setting.

Inter-electrode gap test

To change the inter-electrode spacing, the electrolyte solution was removed from the cell. This was done by siphoning the electrolyte back to the storage container. Once the cell was empty the inter-electrode gap was adjusted by using the rails on the supporting frame and measuring the gap until the desired spacing was achieved. The diaphragm and the cathode also had to be adjusted with the inter-electrode gap to ensure all the components were centred with even spacing throughout the cell. When the setup was completed the above procedure was then used to gather the high speed camera data.

Anode height test

The electrolyte was removed by siphoning it out and into the storage container. The previous anode was loosened from the supporting frame, removed and then the new anode was inserted in the cell as described in the electrolysis setup. The desired inter-electrode distance was measured and the anode was tightened in place. The above procedure was then used to conduct the high speed video imaging.

3.7. Data acquisition method

The high speed video recordings were used in the post analysis to study the flow patterns and to measure the bubble sizes, bubble speeds and the speeds of the PSP tracking particles which represented the electrolyte flow field at the bottom of the anode. To track and measure the flow patterns, the gas bubbles and PSP particles were used. In the areas that had gas bubbles the gas bubbles were used as flow followers to track the flow fields and in the areas with no gas bubbles the PSP particles were used.

The initial plan was to use the Photron FASTCAM Analysis (PFA) software to quantitatively measure the flow patterns. However, the PFA software was not applicable in this system. The software is more applicable in tracking solid objects and it struggled tracking the gas bubbles. The issue was bubble shading and multiple areas that were identical. Thus, the software could not track a single bubble as it followed all the points that were similar to the initial point selected. Alternatively, the PFV camera software was used to view and manually measure the bubble size and speed.

Method of measurement

The high speed video images which were taken in the experiments were reviewed and analysed in order to study the flow fields and to measure bubble size and velocity in different regions within the cell. A pixel counting method was used to measure the bubble size and velocity. An image is made up of pixels and thus an object in a particular image is made up of pixels. To obtain the actual distance covered by those pixels, a ruler was used for the calibration. The ruler was placed in the area of interest before the recordings were taken; this was done to measure the number of pixels that cover 1 mm of the ruler length. The number of pixels that make up a single bubble was counted and using the calibration figure, the number of pixels of the bubble was converted to a millimetre reading. Figure 3.23 shows a snapshot of the ruler used in the calibration. The image taken was zoomed in (image B) to count the number of pixels that make up 1 mm. In the example shown in Figure 3.23 the zoomed in image, the 1 mm gap is covered by 17 pixels. The bubbles were randomly selected and a total of thirty bubbles were selected and measured for each of the recordings captured.

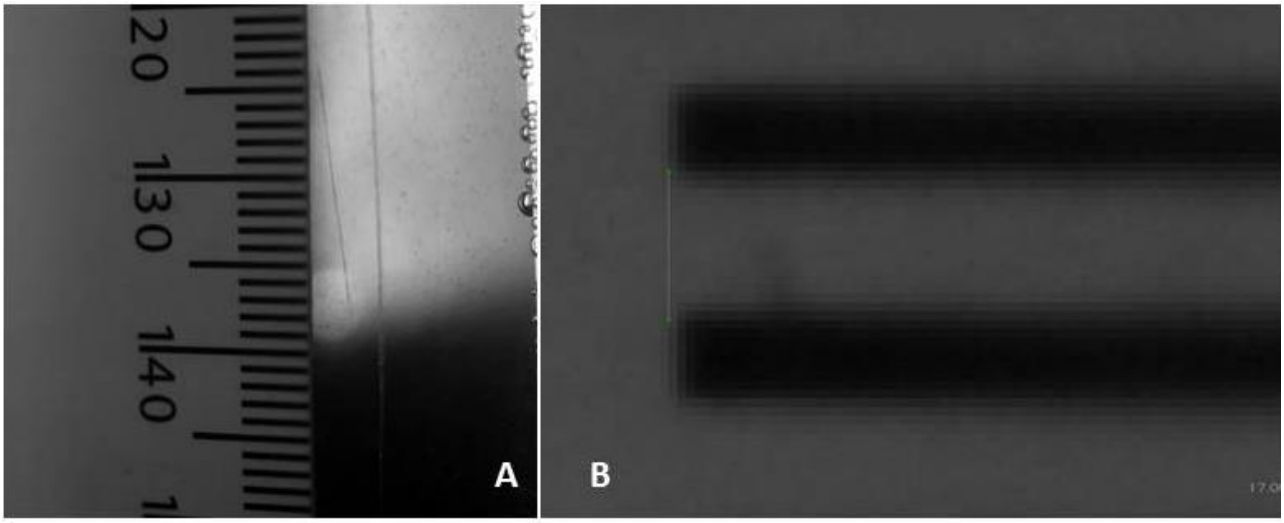

Figure 3.23: Picture of the calibration method. Image A shows the ruler placed at one of the positions of interest and B shows the same image in a zoomed format showing the pixels

To measure the bubble speeds, one bubble was selected and tracked over a number of frames and the distance it covered per frame was counted using the pixels. Since the number of frames per second was known, this was used to determine the time it took for that specific bubble to cover the measured distance. This information was then used to calculate the average bubble speed.

4. RESULTS AND DISCUSSIONS

4.1. Introduction

This chapter presents the results obtained from the high speed video imaging experiments. The high speed camera was placed in the Position A, B, C and D as shown in section 3.6. The high speed video images that were captured were then used for measuring the bubble size and the bubble speed. In Position A and D, the bubble speed was measured in the vertical direction only and the horizontal component was assumed to be negligible since the bubble were mostly rising vertically. In Position B and C the bubble speed was measured in the horizontal and vertical direction as the bubbles had both components in their motion. In this section the flow field patterns are presented for only one case with all the camera positions for that case. The other cases are presented in the appendices.

4.2. Current density test

4.2.1. Position A - Top front

It was observed that the average bubble speed increased with increasing current density. Table 4.1 shows this increasing trend in the average bubble speed as well as in the average bubble size. There was a significant increase in the bubble speed when the current density changed from 50 A/m^2 to 100 A/m^2 as illustrated in Table 4.1. However, the average bubble speed did not show a large increase when the current density changed from 100 A/m^2 to 150 A/m^2.

The increasing trend in average bubble speeds with increasing current density can be related to the amount of bubbles generated. Faraday's law states that the amount of electro generated gas is directly proportional to the current density of the cell (Abdelouahed *et al.*, 2014a; Sandenbergh, 2014a; Newman, 1973: 167-178). Therefore, as the current density was increased more gas bubbles were formed. The gas bubbles formed moved upwards due to the buoyancy force and in that process creating a natural convection in the area next to the anode. This results into the electrolyte being dragged upwards by the rising gas bubbles. This bubble motion induces the electrolyte flow next to the surface of the anode and hence initiates the

electrolyte circulation around the anode. The electrolyte circulation is important because it improves the mixing, mass transfer and also reduces the bubble coverage on the anode surface (Vogt, 2011; Ashraf Ali & Pushpavanam, 2011a; Vogt, 1978).

The increase in current density increases the nucleation rate of the bubbles as well as the activated nucleation sites for bubble growth (Al Shakarji *et al.*, 2011; Sillen *et al.*, 1982). Thus, more gas bubbles were produced at the higher current densities. The gas bubbles departing from the anode surface rise up and create buoyancy driven electrolyte flow parallel to the anode surface (Vogt, 1978). Hence, an increased fluid flow next to the anode surface was observed. The high fluid flow next to the anode surface has an added benefit of increasing the electrolyte circulation and mixing in the cell.

The increasing current density also had an effect on the bubble size, with the size increasing slightly with increasing current density. As a result of having more nucleation sites at higher current densities more of the bubbles grow next to each other on the anode surface. This can result into more bubble coalescences as the bubbles would grow very close to one another and hence larger bubbles detach from the anode surface.

However, because of the increased electrolyte flow caused by the increasing current density, the bubbles do not get sufficient time to coalesce to form very big bubbles. The slight increase in the observed bubble size can be attributed to the increased convection which potentially causes the bubbles to detach prematurely before they could grow bigger and also to coalesce with neighbouring bubbles. Furthermore, the natural convection of the electrolyte may disturb the growth of the small bubbles at the nucleation sites (Zhang & Zeng, 2012). There was a fraction of smaller bubbles which were observed in the experiments, particularly at 150 A/m^2.

There are a number of interacting mechanisms in gas evolving electrochemical systems. Having more gas bubbles generated with the increase in current density has other consequences such as increasing the gas void fraction, increasing the bubble coverage, reducing the electrolyte conductivity and increasing the electrolyte resistance in the space between the electrodes. All these factors have a negative impact on the cell performance and efficiency as they result in energy losses.

Table 4.1: Average bubble speed and bubble size at Position A for different current densities

Current density (A/m^2)	Average speed (mm/s)	Average bubble size (mm)
50	57 ± 1	0.33 ± 0.04
100	96 ± 2	0.35 ± 0.04
150	102 ± 2	0.37 ± 0.05

Figure 4.1 represents the bubble formation and progression as they depart from the anode surface and enter Position A. The image shown in Figure 4.1 presents different frames of a recording taken during the experimental work. The frames show the motion of the rising gas bubbles. The gas bubbles formed at the anode surface rise up due to the buoyancy force and at the top of the anode the bubbles move towards the left wall of the cell. The gas bubbles have a much lower density compared to the electrolyte solution as a result the main driving force for the upwards motion of the bubbles is the density difference. The electrolyte in Position A follows the motion of rising bubbles, also moving towards the cell left wall.

The bubble cloud shown in Figure 4.1 illustrates this bubble flow field at Position A whereby the bubbles move upwards and shape off towards the left side. These gas bubbles then proceed to disengage at the electrolyte free surface and others move towards Position B. While moving upwards the gas bubbles drag the electrolyte in the upwards direction.

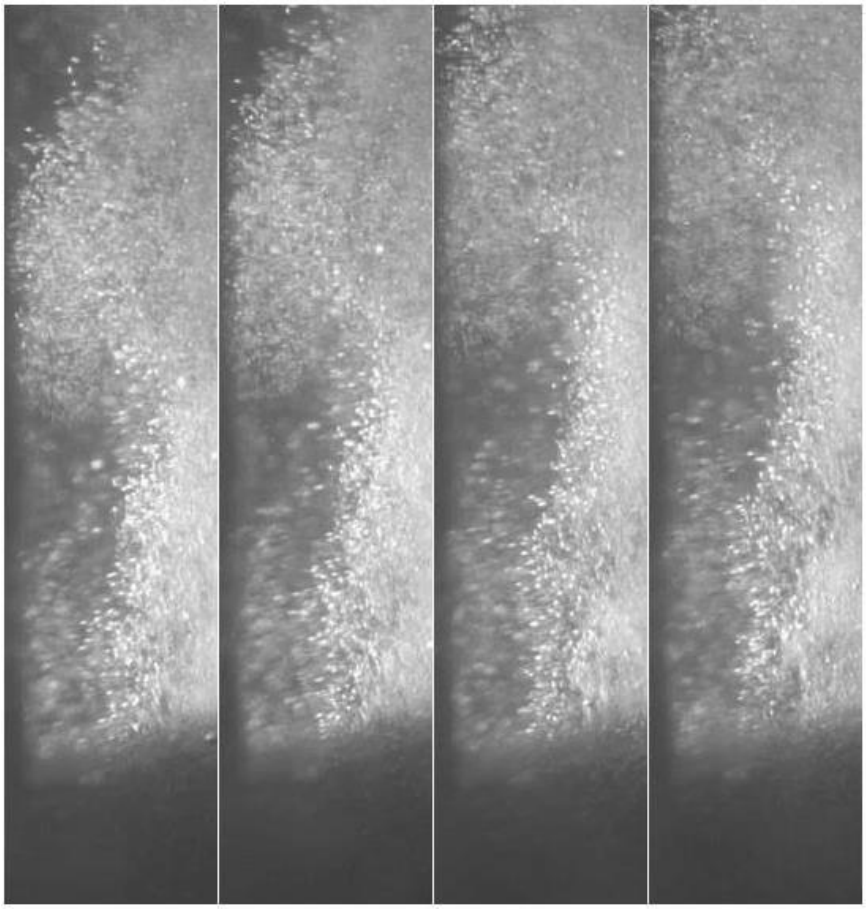

Figure 4.1: Gas bubble flow field pattern at Position A for the base case condition

The gas bubble flow field patterns in Position A for test 1, 2, 4, and test 6 can be seen in Appendix B1. The flow patterns observed in Position A were similar for all the cases; the only difference is in the amount of bubbles generated and the speed of the bubbles.

4.2.2. Position B - Top backside circulation

The average bubble speed increased with an increase in the current density at Position B. Table 4.2 indicates the increase in the bubble speed with increasing current density. The gas bubbles in Position B were the gas bubbles that passed through Position A and thus a similar trend in the bubble speeds can be expected. However, a fraction of the bubbles that passed Position A disengaged at the electrolyte free surface, thus not all of the bubbles move towards Position B. The average bubble speed in Position B was lower than in Position A for all the current densities. This was because there was no gas production in Position B and thus there was no driving force for the bubbles. The bubbles in Position B are merely the smaller bubbles that passed through Position A. The bubble speed is the sum of the bubble rise

velocity and the electrolyte velocity. The electrolyte velocity changed direction as the electrolyte flowed over the top of the anode and it also slowed down because the flow area became much wider above the anode than between the two electrodes.

The bigger bubbles on the other hand have a higher rise velocity relative to the electrolyte and hence have a larger probability to disengage than the smaller ones before being carried downwards by the electrolyte flow that reverses in the space above the anode.

Table 4.2: Average bubble speed and bubble size at Position B for different current densities

Current density (A/m^2)	**Average speed (mm/s)**		**Average bubble size (mm)**
	v_x	**v_y**	
50	3 ± 2	6 ± 3	0.18 ± 0.04
100	7 ± 3	12 ± 2	0.17 ± 0.03
150	13 ± 3	17 ± 2	0.26 ± 0.05

Figure 4.2 presents the flow field of the gas bubbles as they move from Position A and entering Position B. The frame labelled 1 show the bubble cloud entering Position B and deflecting from the electrolyte surface at the top. The label 2 shows the same bubble cloud after it has deflected off the electrolyte surface and moving downwards. As more gas bubbles move into Position B, the bubble cloud moves further to the left until it deflects off the left wall of the cell. This can be seen in the frame labelled 3 were the bubble cloud is accumulated on the left wall and moving downwards. To complete the flow pattern in Position B, after the bubble cloud hits the left wall it moves downwards and towards the right side. Due to the density differences, the bubble cloud does not cover a long distance in the downwards direction before it rises up. This can be seen in the image where the bubble cloud forms a circulation loop, as shown in label 3 and 4. The gas bubbles follow this flow pattern in Position B and accumulate in that region while other bubbles disengage at the top electrolyte surface. The complete flow field pattern in this region formed a circulation loop as more bubbles accumulated in Position B. This bubble motion also represents the motion of the electrolyte at Position B.

The rising bubbles passing Position A push the electrolyte in that space towards Position B and the electrolyte in Position B gets pushed towards the cell left wall. This electrolyte motion tends to pull the smaller sized bubbles towards Position B and also in the downwards direction in the region between the cell left wall and anode backside. Thus, the electrolyte flow pattern has a contributing factor in the observed flow field pattern of the gas bubbles, particularly at Position B.

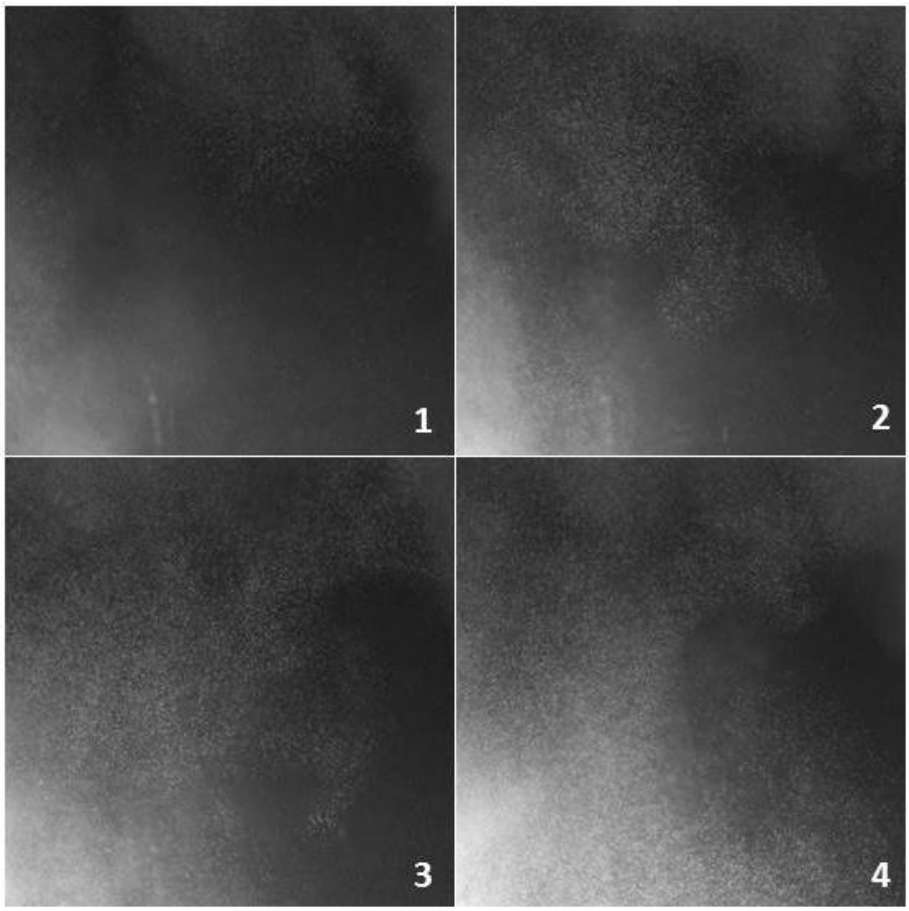

Figure 4.2: Gas bubble flow field pattern at Position B for the base case condition

The gas bubble flow field patterns in Position B for test 1, 2, 4, and test 6 can be seen in Appendix B2. The flow patterns observed in Position B were similar for all the cases, the only differences were in the amount of bubbles present, bubble size and the speed of the bubbles.

4.2.3. Position C - Bottom circulation

Table 4.3 shows the average electrolyte speeds and bubble sizes at the bottom of electrolysis cell for different current densities. The electrolyte speed showed an increasing trend with increasing current density. There was little change in the measured bubble sizes with increasing current density. The bubble sizes measure at 50 A/m^2 and 100 A/m^2 were the same at 0.25 mm and only 0.26 mm at 150 A/m^2.

Table 4.3: Average bubble size at the bottom anode surface and electrolyte speed at Position C for different current densities

Current density (A/m^2)	Average speed (mm/s)		Average bubble size (mm)
	v_x	v_y	
50	10 ± 5	6 ± 3	0.25 ± 0.04
100	12 ± 6	10 ± 5	0.25 ± 0.06
150	22 ± 7	25 ± 7	0.26 ± 0.06

Figure 4.3 shows the electrolyte flow pattern at the bottom of the anode. The tube seen in the image was used to inject the PSP particles into the electrolyte flow field and hence making the electrolyte flow field visible to the eye. The frames presented in the Figure 4.3 show the progression of the seeding particles as they move with the electrolyte flow. The particles were injected from the insulated backside of the anode. It can be observed that the particles circulated around the bottom of the anode and moved towards the anode-diaphragm gap.

The electrolyte circulation began at the anode right face when the gas bubbles were generated; these bubble created natural convection that caused the electrolyte to rise up with the bubbles. As the electrolyte reached the top part of the anode (Position A) it flowed over to Position B where it proceeded to flow downwards. All this motion resulted in the electrolyte flowing downwards on the backside of the anode until the electrolyte reached Position C. Since there were gas bubbles generated on the front side of the anode, this resulted in the electrolyte being pulled towards the front side. As a result, the electrolyte rising upwards on the front and the electrolyte moving downwards on the backside caused the circulation loop which can be observed in Figure 4.3. The electrolyte proceeded to move over towards the

cathode half and this motion enhances the mixing and potentially the mass transport of the ions to the electrodes.

Figure 4.3: Electrolyte flow field pattern represented by the PSP seeding particles at Position C for the base case condition

The electrolyte flow field pattern in Position C for test 1, 2, 4, and test 6 can be seen in Appendix B3. The flow patterns observed in Position C were similar for all the cases; the only difference was in the speed of the electrolyte.

4.2.4. Position D - Anode diaphragm gap

Position D represents the spacing between the anode and diaphragm. This was a very narrow gap as a result it was a challenge getting sufficient lighting into the gap. Because of the poor lighting the high speed video images that were captured were not clear enough to be able to extract the bubble size and bubble speeds measurements. Hence, there was missing data presented for this position. Table 4.4 presents the data that could be retrieved from the recordings.

The amount of bubbles generated increased with the increasing current density. At the higher current densities, the bubbles accumulated in the narrow gap making it difficult to conduct the measurements. Moreover, the lighting in the gap was not sufficient and the recordings

were not good quality. Hence, no data was reported for the 100 A/m^2 and 150 A/m^2 current densities.

Table 4.4: Average bubble size and bubble speed at the anode-diaphragm gap for different current densities

Current density (A/m^2)	Average speed (mm/s)	Average bubble size (mm)
50	49 ± 1	0.34 ± 0.05
100	N/A	N/A
150	N/A	N/A

Figure 4.4 shows the gas bubble flow field in the anode-diaphragm gap. The frames shown in the figure were taken from the test 1 (50 A/m^2). The white cloud next to the anode were the gas bubbles, as seen in the image the bubble cloud/curtain is close to the anode and does not extend towards the diaphragm. This was the observed flow pattern for the lowest current density tested whereby the gas bubbles tend to rise up along the anode surface. When the current density was low the gas bubble generation was low and the bubbles did not move across the diaphragm. However, as the current density increased more gas bubbles were generated at the anode. These bubbles moved towards the diaphragm and a fraction of the bubbles did go through the diaphragm. Although, the bubbles crossed the diaphragm they remained close to the other side of the diaphragm and moved upwards. The bubbles did not move laterally all the way to the cathode surface.

The diaphragm did manage to disengage some of the bubbles and it also trapped a number of bubbles on the diaphragm slots. The diaphragm was successful in performing the tasks mentioned; however, when the amount of bubbles increased the diaphragm did not completely prevent the bubbles from crossing over to the cathode half.

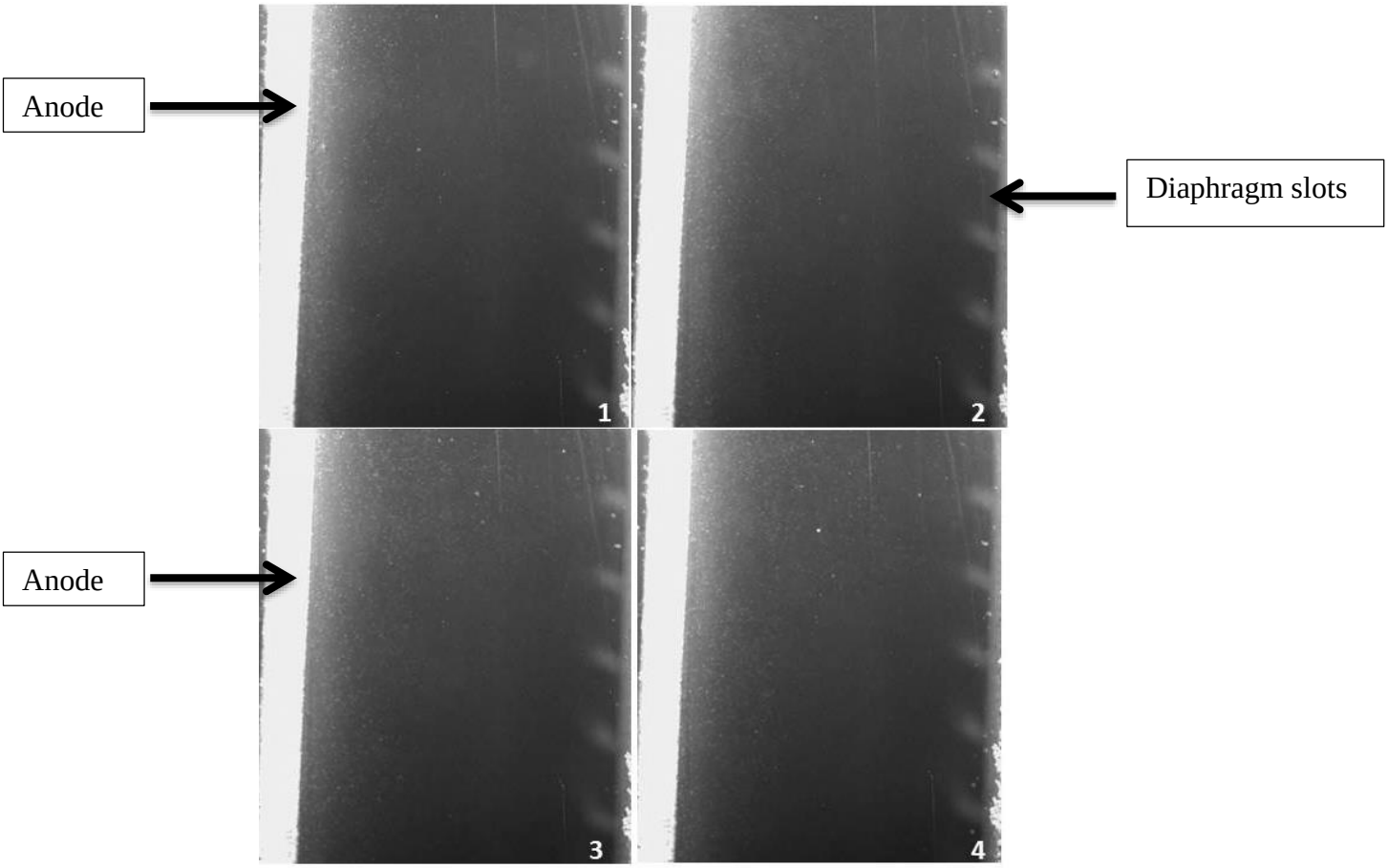

Figure 4.4: Gas bubble flow field pattern at Position D for the 50 A/m^2 current density test

4.3. Inter-electrode distance test

4.3.1. Position A - Top front

Table 4.5 shows the average bubble speeds and bubble size for different inter-electrode distances. The average bubble speeds showed a decreasing trend with an increase in the inter-electrode spacing as shown in Table 4.5. The average bubble speeds did not show a big change when the electrode spacing was increased from 80 mm to 90 mm, the measured speeds were 97 mm/s and 96 mm/s respectively. When the electrode spacing was changed to 100 mm the measured average bubble speed was 84 mm/s.

When the inter-electrode distance was 80 mm, the average bubble speed in Position A was measured to be 97 mm/s. On the other, the electrode spacing of 90 mm achieved an average bubble speed of 96 mm/s. There was a slight difference in the results obtained from these two conditions. In this case the inter-electrode spacing of 90 mm would be favourable since it has

a bigger space between the electrodes that will allow the bubbles concentration to be lower compared to the narrower 80 mm. Moreover, the average bubbles sizes measured at 90 mm were slightly larger than at 80 mm and large bubbles disengaged much easier than the smaller bubbles.

Table 4.5: Average bubble speed and bubble size at the top front side of the anode for different inter-electrode spacing

Inter-electrode gap (mm)	Average speed (mm/s)	Average bubble size (mm)
80	97 ± 1	0.32 ± 0.04
90	96 ± 2	0.35 ± 0.04
100	84 ± 2	0.35 ± 0.04

The challenge with very narrow electrode spacing is that the bubble concentration tends to increase quickly in the inter-electrode gap and thus causing a large gas void fraction which increases the electrolyte resistance. The void fraction can be reduced by having a high electrolyte circulation rate, ensuring the gas bubbles are removed quickly from the inter-electrode gap.

The electrolyte resistance is proportional to the inter-electrode distance (Hine *et al.*, 1980; Nagai *et al.*, 2003a). This relationship can be seen in Table 4.6, whereby the electrolyte increases with an increase in electrode spacing. The electrolyte used in this study was a 100 g/l solution of copper sulphate and at this concentration and at 25 °C the conductivity of the solution is 265 S/m (Bešter-Rogac, 2008). The values in Table 4.6 did not take into account the presence of gas bubbles. The presence of gas bubbles in the inter-electrode space has been shown to increase the electrolyte resistance (Hine *et al.*, 1980; Nagai *et al.*, 2003a). Moreover, gas bubbles have zero conductivity and their presence in the electrolyte reduces the conductivity of the electrolyte (Sandenbergh, 2014c). The large electrolyte resistance causes a reduction in the energy efficiency of the system as more energy is required to overcome the resistances. This leads to having only a fraction of the energy input going to the actual electrochemical reaction and the rest of the energy dissipated as heat.

Table 4.6: Electrolyte resistance for the different inter-electrode distances which were investigated

Inter-electrode distance (m)	Resistance (Ω)
0.08	1.18E-03
0.09	1.33E-03
0.1	1.48E-03

Figure 4.5 shows the gas bubble flow field in Position A. Different frames are presented in the figure to show the flow pattern of the gas bubbles in Position A. The flow fields observed in Figure 4.1 were similar to the other cases; they all had the same flow patterns. Hence, similar deductions of the flow patterns can be drawn for Figure 4.5. The only differences were the magnitudes of the velocities as well as the bubble sizes which are presented in Table 4.5.

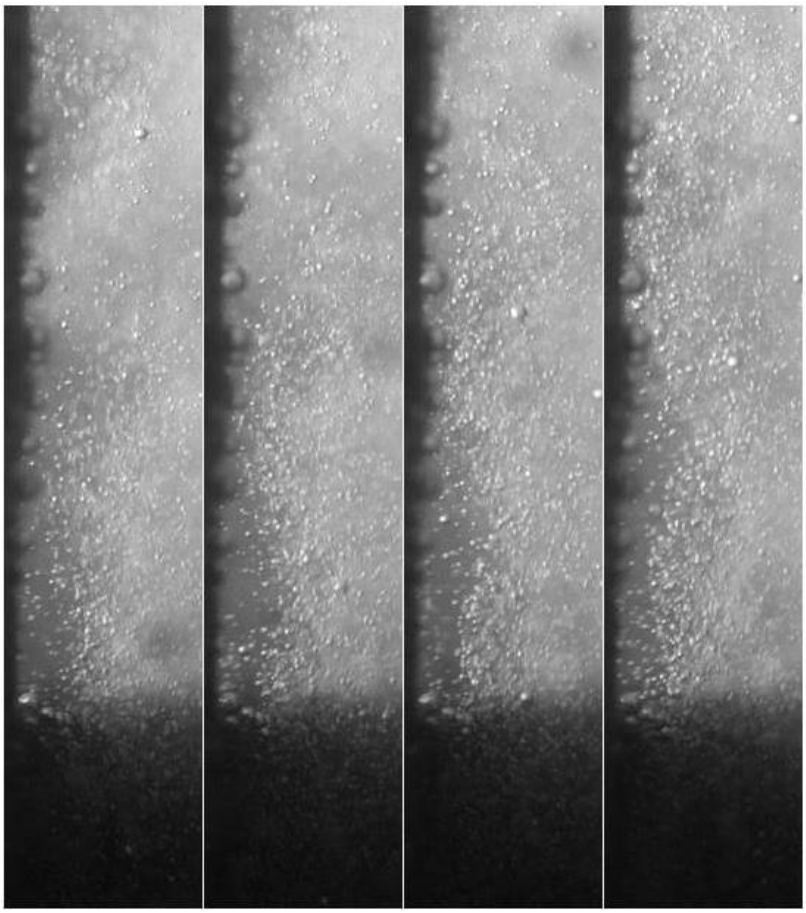

Figure 4.5: Gas bubble flow field pattern in Position A for test 5, the 80 mm inter-electrode gap

The gas bubble flow field patterns in Position A for test 1, 2, 4, and test 6 can be seen in Appendix B1.

4.3.2. Position B - Top backside circulation

Table 4.7 shows the average bubble speed and bubble size measured in Position B for different inter-electrode distance. The average bubble sizes were very similar for the three cases tested. It was evident that the bigger bubbles disengaged at the electrolyte surface and smaller bubbles were pulled towards Position B. When the inter-electrode spacing was increased, the average bubble speeds decreased. Similarly to Position A, the bubble speeds measured for the 90 mm gap were very close to the speeds for the 80 mm gap. In fact, the 90 mm gap showed higher bubble speeds. This can be attributed to the relatively high driving force in Position A compared to the other cases.

Table 4.7: Average bubble speed and bubble size at the top backside of the anode for different inter-electrode spacing

Inter-electrode gap (mm)	Average speed (mm/s)		Average bubble size (mm)
	v_x	v_y	
80	10 ± 3	7 ± 2	0.18 ± 0.04
90	7 ± 3	12 ± 2	0.17 ± 0.03
100	3 ± 2	3 ± 2	0.18 ± 0.03

Figure 4.6 illustrates the movement of the gas bubbles as the bubbles accumulate in Position B. The gas bubbles follow the same flow field as presented in Figure 4.2. The image presented in Figure 4.6 shows a fully developed flow pattern in Position B. The bubble cloud at top next to the electrolyte surface can be seen moving towards the left side (from label 1 to label 2). The progression of the circulation whirl shown in Figure 4.2 is not clearly visible in the developed flow. However, the whirl was formed and the centre of the whirl can be seen in the middle area of each of the frames, where bubble population is lower compared to the other areas.

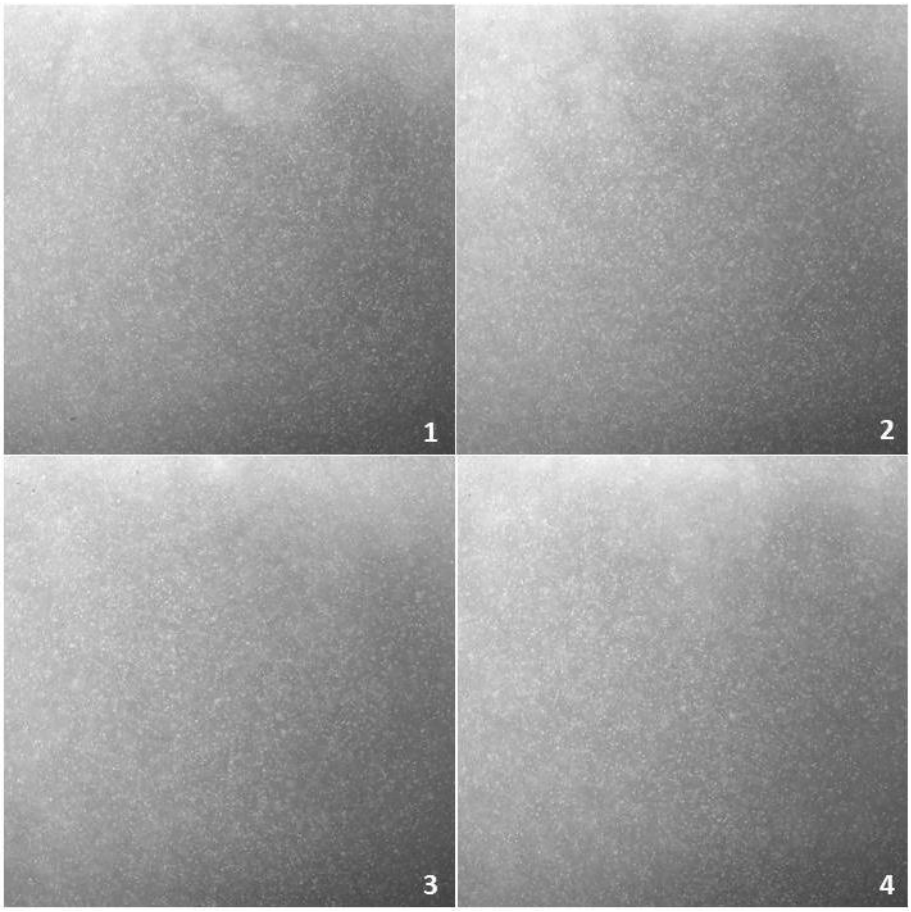

Figure 4.6: Gas bubble flow field pattern in Position B for the 80 mm inter-electrode gap

The gas bubble flow field patterns in Position B for test 1, 2, 4, and test 6 can be seen in Appendix B2.

4.3.3. Position C - Bottom circulation

Table 4.8 presents the average electrolyte velocities and average bubble sizes produced at the bottom part of the anode for different inter-electrode gaps. The driving force for the circulation at the bottom of the anode is a combination of the electrolyte circulation generated in Position A and B. There is minimal gas bubble generation at the bottom of the anode; however, the bubbles formed at the bottom also contribute in the circulation rates. The 80 mm inter-electrode gap gave the highest electrolyte speeds and the speeds decreased as the inter-electrode distance increased.

Table 4.8: Average bubble size at the bottom anode surface and average electrolyte speed at Position C for different inter-electrode spacing

Inter-electrode gap (mm)	Average speed (mm/s)		Average bubble size (mm)
	v_x	v_y	
80	17 ± 2	16 ± 2	0.24 ± 0.04
90	12 ± 6	10 ± 5	0.25 ± 0.06
100	13 ± 3	12 ± 4	0.29 ± 0.05

Figure 4.7 illustrates the electrolyte circulation at the bottom of the anode. The frames in the figure show the cloud of the seeding particles moving out the tube and then following the flow pattern of the electrolyte. The electrolyte circulation pattern was the same as the previous case. The only difference was the magnitude of the circulation which was mainly affected by the amount of gas generated.

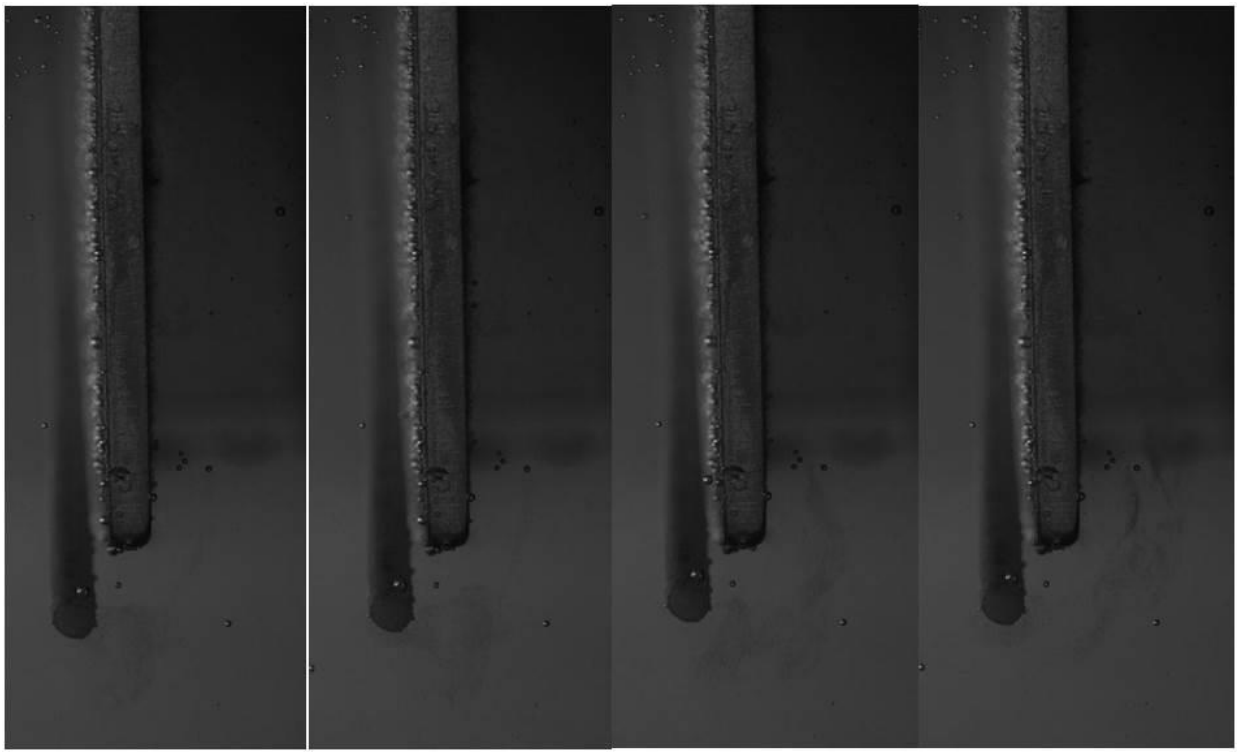

Figure 4.7: Electrolyte circulation at the bottom of the anode for the 80 mm inter-electrode gap. PSP tracking particles used to track the electrolyte flow field

The electrolyte flow field pattern in Position C for test 1, 2, 4, and test 6 can be seen in Appendix B3.

4.3.4. Position D - Anode diaphragm gap

Position D was the narrow gap between the anode-diaphragm. The main challenge here was getting sufficient lighting through this narrow region as a result blurry images were taken and it was difficult to get the required measurements. Hence, no data has been reported for this position.

4.4. Anode height test

4.4.1. Position A - Top front

Table 4.9 presents the average bubble speeds and bubble sizes obtained from the experiments with different anode heights. The average bubble speeds increased as the anode increased in length. The largest anode showed a higher average bubble speed as well as larger bubble size. The anode height increased the current in order to maintain the same current density. This resulted in the formation of more bubbles. This caused both a higher driving force or induced electrolyte flow and an increase in the bubble concentration in the electrolyte as it flowed out of the inter-electrode space. A higher concentration of bubble in the electrolyte can be expected to increase the rate of bubble coalescence.

Table 4.9: Average bubble speed and bubble size at Position A for different anode heights

Anode height (mm)	Average speed (mm/s)	Average bubble size (mm)
500	48 ± 1	0.31 ± 0.05
700	96 ± 2	0.35 ± 0.04
1000	101 ± 2	0.39 ± 0.05

Figure 4.8 shows the gas bubble flow field pattern at Position A for the anode height of 500 mm. The frames in the figure show the progression of the gas bubbles as they passed through Position A. There were fewer bubbles produced when the 500 mm anode was used, this was expected because of the reduced surface area and hence reduced current. The bubbles

observed were also smaller in size compared to the other cases and this can be seen from the frames in Figure 4.8. The bubble flow field pattern in Position A was the same as the other cases with the only difference observed in the amount of bubbles, bubble speeds and bubble sizes.

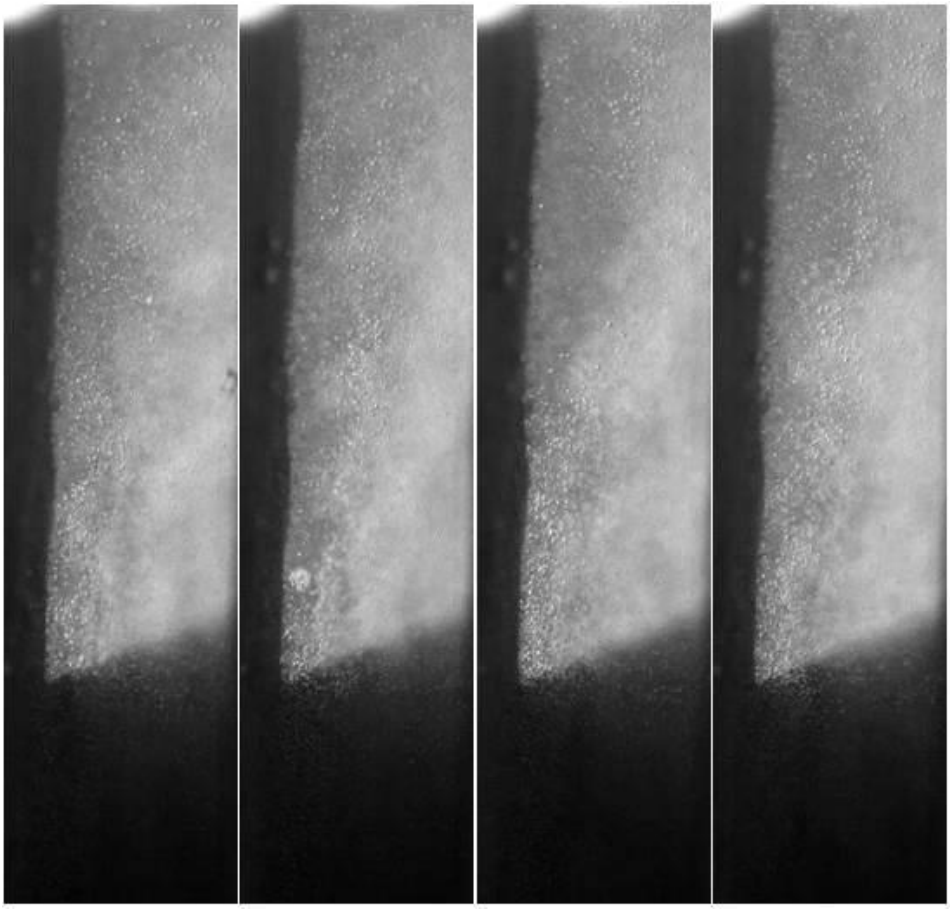

Figure 4.8: Gas bubble flow field pattern at Position A for test 3, the anode height of 500 mm

The gas bubble flow field patterns in Position A for test 1, 2, 4, and test 6 can be seen in Appendix B1.

4.4.2. Position B - Top backside circulation

Table 4.10 presents the average bubble speed and bubble size in Position B for the different anode sizes tested. As expected the bubble speeds in Position B were much lower than the speeds in Position A. The bubble speed increased with the increasing anode height. The largest anode generated more gas bubbles and hence there was a higher driving force for the bubbles accumulating in Position B. This was indicated by the higher average bubble speed for the 1 m anode. On other hand, the smallest anode showed lower average bubble speeds.

This was mainly attributed to the lower driving force for electrolyte circulation around the anode as the bubble production rate was much lower compared to the other cases.

Table 4.10: Average bubble speed and bubble size at the top backside of the anode for different anode heights

Anode height (mm)	**Average speed (mm/s)**		**Average bubble size (mm)**
	v_x	v_y	
500	5 ± 3	5 ± 3	0.17 ± 0.04
700	7 ± 3	12 ± 2	0.17 ± 0.03
1000	8 ± 4	20 ± 4	0.29 ± 0.05

Figure 4.9 illustrates the flow pattern of the gas bubbles as they accumulate in Position B. The gas bubbles entered Position B, formed the circulation loop in the region while accumulating in that space. The white cloud observed in the frames presented in Figure 4.9 was the gas bubbles. These bubbles were very small as can be seen from the image. The average bubble size in this region was 0.17 mm. The bigger bubbles on the right side of each of the frames were bubbles that were attached on the backside of the anode and coalesced until they were big enough to detach and rise up. These bubbles were considered to be outliers in the bubble size measurements because they were not representative of the bulk of the gas bubbles in the region. The size difference is clearly visible in the frames in Figure 4.9.

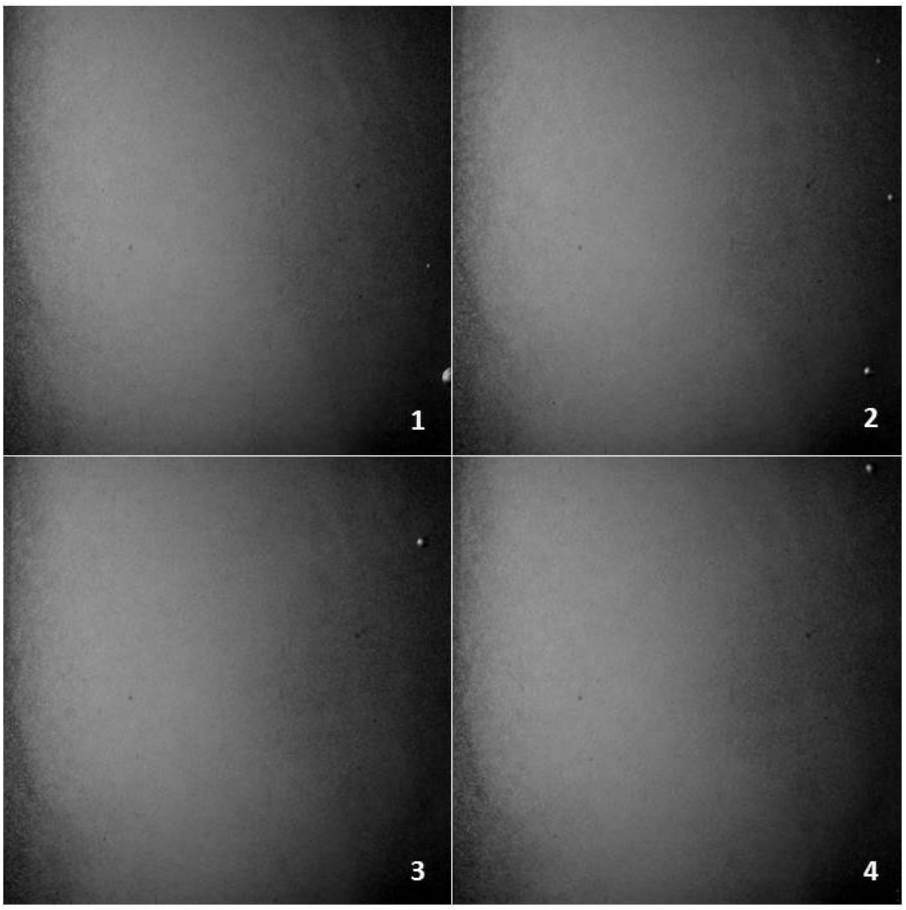

Figure 4.9: Gas bubble flow field pattern in Position B for test 3, the 500 mm anode height

The gas bubble flow field patterns in Position B for test 1, 2, 4, and test 6 can be seen in Appendix B2.

4.4.3. Position C - Bottom circulation

Table 4.11 shows the average electrolyte speed and average bubble size at the bottom of the anode for each of the anode sizes tested. The electrolyte speed increased with the increase in anode height. This was mainly due to the amount of gas bubbles produced with the different anode sizes. When the bubble production is enhanced the electrolyte circulation is increased. Hence, the largest anode had the highest electrolyte speed. The largest anode showed a better performance with regards to the electrolyte speeds. This is important because the higher the circulation the better the mixing and subsequently the better the performance of the electrolysis cell.

Table 4.11: Average bubble size at the bottom anode surface and average electrolyte speed at Position C for different anode heights

Anode height (mm)	**Average speed (mm/s)**		**Average bubble size (mm)**
	v_x	v_y	
500	5 ± 3	7 ± 4	0.24 ± 0.05
700	12 ± 6	10 ± 5	0.25 ± 0.06
1000	17 ± 5	11 ± 4	0.28 ± 0.05

Figure 4.10 illustrates the electrolyte circulation at the bottom of the smallest anode tested. The electrolyte circulation pattern observed was similar to the other cases. The electrolyte circulation in this case was very low, because the seeding particles took longer to rise up compared to the other cases. The driving force was very low and the seeding particles moved more towards the diaphragm bottom, the upwards movement was not as dominant as observed in the other cases. This can be attributed to the reduced number of bubbles produced by the small anode. As a result, the electrolyte circulated around the anode at a lower rate.

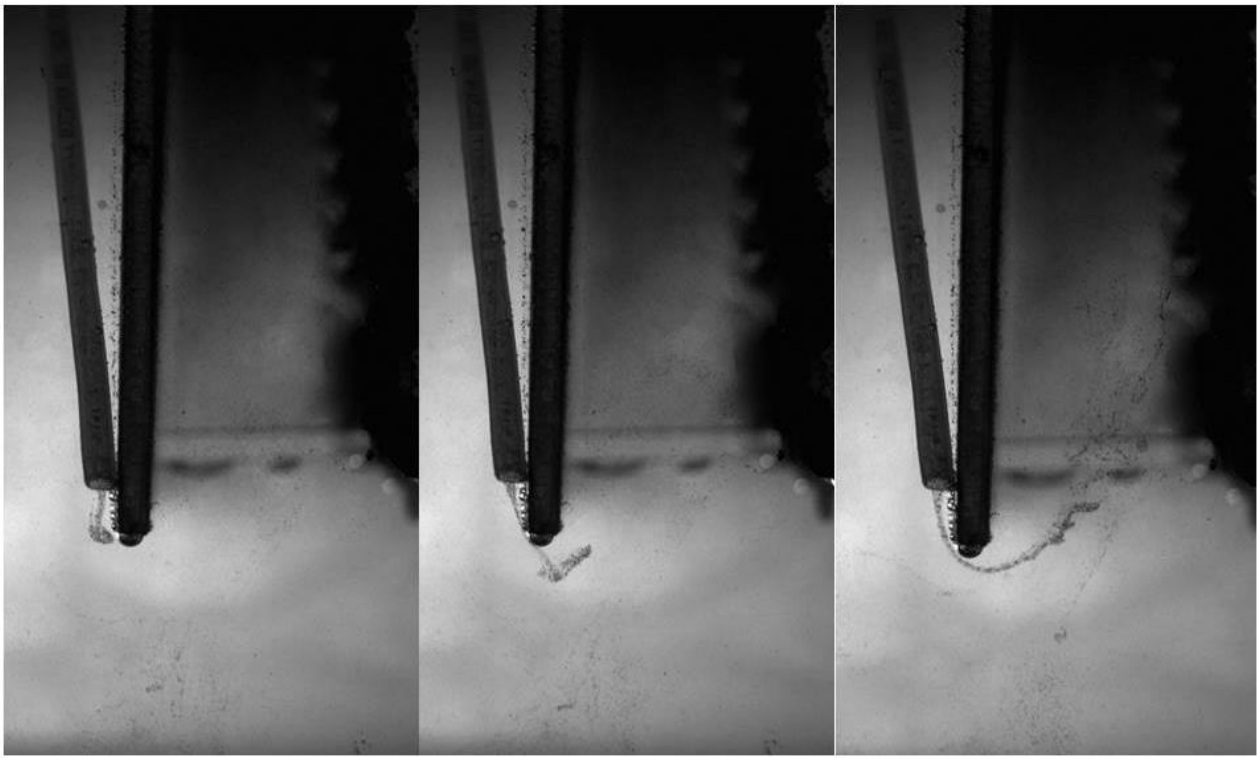

Figure 4.10: Electrolyte circulation at the bottom of the anode for test 3, the 500 mm anode height. PSP seeding particles were used to track the electrolyte flow field

The electrolyte flow field pattern in Position C for test 1, 2, 4, and test 6 can be seen in Appendix B3.

4.4.4. Position D - Anode diaphragm gap

The anode-diaphragm gap was very narrow as a result it proved challenging to sufficiently illuminate the gap. For that reason, the illumination was poor and the high speed video recordings captured were not clear enough to be able to extract the bubble size and bubble speed measurements. Hence, there was no data presented for this position.

5. CFD MODEL

5.1. Introduction

A CFD model was developed in a previous study to predict the flow patterns of a molten salt electrolyte (Baloyi *et al.*, 2014). However, there were uncertainties in the findings of the model. This was mainly because there was no experimental data to validate the modelling work. As a result, an experimental study was required to observe and measure the flow patterns. The experimental investigation would then be used to validate the modelling approach which was used in the previous study. The model validation would provide more confidence in the approach used and be able to apply it in future studies to make further improvements in the system investigated.

The model used in the molten salt study was adopted and applied by Mr Baloyi to the system which was used in the experimental investigation. Basically, the cell dimensions and the physical conditions were adopted and applied in the model. Ansys Fluent version 16.2 was used to perform the CFD simulations. The computer used to run the simulations was a DELL precision T5500 with 12 GB of RAM. The simulations took between 7 and 10 hours real time to converge to a solution. This section presents the model approach and the results obtained from the model simulation.

5.2. Methodology

The electrolysis cell was approximated by a planar two-dimensional domain, where the in-plane momentum components were assumed to be negligible and to have no effect on the steady state solution. This simplified the domain to be modelled. The fluid flow pattern of the two fluids were assumed to be affected only by the change in momentum of the two fluids, since all other physical, chemical and electro-magnetic phenomena were not modelled in this study.

5.3. Numerical modelling

The multiphase flow problem under study was modelled by using the Eulerian multiphase flow with two phases, without taking into consideration breakage, coalesce and nucleation of the bubbles. The oxygen gas bubbles produced on the anode surface differ in size. These bubbles as they rise in the aqueous electrolyte solution could coalesce and combine to form bigger bubbles or even break up to form smaller ones. All these possible phenomena were simplified by assuming a constant bubble diameter of 0.35 mm.

The study was conducted by approximating the steady state solution by a pseudo-steady state formulation of the Navier-Stokes equations that mathematically describe the flow field of the multiphase problem. The pseudo-steady state formulation has the advantage of stabilising the solution towards convergence in the case where it would otherwise diverge if steady state formulation was utilised, yet the resulting solution is a steady state solution. The multiphase problem between an aqueous copper sulphate solution as a liquid and oxygen gas as bubbles was solved by using the Eulerian multiphase model with a mixture model. The volume fraction of each phase was calculated from the continuity equation below:

$$\frac{1}{\rho_{rq}}\left(\frac{\partial}{\partial t}\left(\alpha_q\rho_q\right)+\nabla\cdot\left(\alpha_q\rho_q\vec{v}_q\right)=\sum_{p=1}^{n}\left(\dot{m}_{pq}-\dot{m}_{qp}\right)\right) \tag{5-1}$$

Here ρ_{rq} is the phase reference density or the volume averaged density of the q phase in the solution domain, $\vec{v}_q$ is the velocity of phase q, α_q is the volume fraction of phase q, $\dot{m}_{pq}$ and $\dot{m}_{qp}$ are mass transfer rates from phase p (gas phase) to phase q (liquid phase) and vice versa (they are both zero in our simulations).

The conservation of momentum for the fluid phase q is given by Equation 5-2:

$$\begin{aligned}&\frac{\partial}{\partial t}\left(\alpha_q\rho_q\vec{v}_q\right)+\nabla\cdot\left(\alpha_q\rho_q\vec{v}_q\right)=-\alpha_q\nabla p+\nabla\cdot\bar{\bar{\tau}}_q+\alpha_q\rho_q\vec{g}\\&+\sum_{p=1}^{n}\left(K_{pq}\left(\vec{v}_p-\vec{v}_q\right)+\dot{m}_{pq}\vec{v}_{pq}-\dot{m}_{qp}\vec{v}_{qp}\right)\\&+\left(\vec{F}_q+\vec{F}_{lift,q}+\vec{F}_{wl,q}+\vec{F}_{vm,q}+\vec{F}_{td,q}\right)\end{aligned} \tag{5-2}$$

Here $\bar{\bar{\tau}}_q$ is the stress-strain tensor for phase q, and is given by Equation 5-3:

$$\bar{\bar{\tau}}_q=\alpha_q\mu_q\left(\nabla\vec{v}_q+\nabla\vec{v}_q^{\,T}\right)+\alpha_q\left(\lambda_q-\frac{2}{3}\mu_q\right)\nabla\cdot\vec{v}_q\bar{\bar{I}} \tag{5-3}$$

Here μ_q and λ_q are the shear and bulk viscosities of phase q, and $\vec{g}$ is the acceleration due to gravity. K_{pq}, the interphase momentum exchange coefficient, given by Equation 5-4:

$$K_{pq} = \frac{\rho_p f d_p A_i}{6\tau_p} \tag{5-4}$$

τ_p is the dispersed phase relaxation time given by Equation 5-5:

$$\tau_p = \frac{\rho_p d_p^2}{18\mu_e} \tag{5-5}$$

A_i is the symmetric model interfacial area concentration given by Equation 5-6:

$$A_i = \frac{6\alpha_p(1-\alpha_p)}{d_p} \tag{5-6}$$

where d_p is the bubble diameter. f is the drag function given by Equation 5-7:

$$f = \frac{C_D \,\mathrm{Re}}{24} \tag{5-7}$$

μ_e is the effective viscosity for the bubble-liquid mixture given by Equation 5-8:

$$\mu_e = \frac{\mu_q}{(1-\alpha_p)^{2.5}} \tag{5-8}$$

$\vec{v}_{pq}$ and $\vec{v}_{qp}$ are the interphase velocities which were not computed because $\dot{m}_{pq}$ and $\dot{m}_{qp}$ were zero.

Further, $\vec{F}_q$ is the external body force, $\vec{F}_{lift,q}$ is the lift force, which is neglected in the simulations, $\vec{F}_{wl,q}$ is the wall lubrication force, which is neglected in our simulations, $\vec{F}_{vm,q}$ is the virtual mass force, which is neglected in our simulations, and $\vec{F}_{td,q}$ is the turbulent dispersion force.

The Reynolds Stress model (RSM) was used to model the turbulence experienced by both liquid and gaseous phases. It was assumed that the dispersed phase, which is the oxygen gas

bubbles and the continuous phase ($CuSO_4$ solution) share the same turbulence field. The RSM mixture turbulent model implemented in the numerical software used in the study was expressed mathematically as given by Equation 5-9.

$$\frac{\partial}{\partial t}\left(\rho_m \overline{\alpha}\tilde{R}_{ij}\right)+\frac{\partial}{\partial x_m}\left(\rho_m \overline{\alpha}\tilde{U}_m \tilde{R}_{ij}\right)=-\rho\overline{\alpha}\left(\tilde{R}_{im}\frac{\partial \tilde{U}_j}{\partial x_m}+R_{jm}\frac{\partial \tilde{U}_i}{\partial x_m}\right)+\frac{\partial}{\partial x_m}\left[\overline{\alpha}\mu\frac{\partial}{\partial x_m}\left(\tilde{R}_{ij}\right)\right]$$
$$-\frac{\partial}{\partial x_m}\left[\overline{\alpha}\rho\overline{u_i' u_j' u_m'}\right]+\overline{\alpha\, p\left(\frac{\partial u_i'}{\partial x_j}+\frac{\partial u_j'}{\partial x_i}\right)}-\rho_m\overline{\alpha}\tilde{\varepsilon}_{ij} \qquad (5\text{-}9)$$

Here:

ρ_m is the mixture density given by Equation 5-10:

$$\rho_m=\sum_{i=1}^{2}\overline{\alpha}_i\rho_i \qquad (5\text{-}10)$$

$\tilde{U}_m$ is the mixture velocity given by Equation 5-11:

$$\tilde{U}_m=\frac{\sum_{i=1}^{2}\overline{\alpha}_i\rho_i\tilde{U}_i}{\sum_{i=1}^{2}\overline{\alpha}_i\rho_i} \qquad (5\text{-}11)$$

$\tilde{R}_{ij}$ is the mixture Reynolds stresses given by Equation 5-12:

$$\tilde{R}_{ij}=\rho_m\overline{u_i' u_j'} \qquad (5\text{-}12)$$

$\tilde{\varepsilon}_{ij}$ is the turbulent dissipation rate given by Equation 5-13:

$$\tilde{\varepsilon}_{ij}=2\mu\overline{\frac{\partial u_i'}{\partial x_m}\frac{\partial u_j'}{\partial x_m}} \qquad (5\text{-}13)$$

The time derivative terms in all the conservative expressions listed above were all treated in a pseudo transient manner in order smooth out instabilities in the solution of the numerical simulation and get better convergence of the continuity expression.

Geometries of the domains for the seven cases were created with the dimensions correspond to those listed in Table 3.1. The domains were discretised using quadrilateral cells, and as an example the mesh for Test 3 is shown in Figure 5.1.

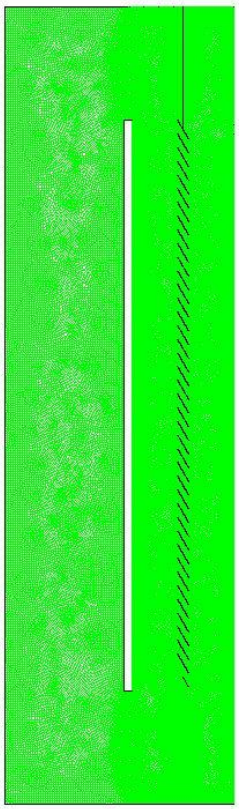

Figure 5.1: A plot of the domain meshed with quadrilateral cells

5.4. Boundary conditions

The boundary conditions are presented in the figures below; these show the geometry as represented in the CFD code used for the numerical simulation. Figure 5.2 shows the overall view of the cell with all the important boundaries of the cell shown. The liquid free surface was modelled using a degassing boundary condition which allowed only gas to pass through it, and acts as a slip symmetry plane to the liquid. All the walls were modelled by using a non-slip plane boundary condition.

The following boundaries were modelled as walls:

- Cell left wall
- Cathode left wall

- Diaphragm vertical plate
- Diaphragm slots
- Cell floor
- The left, top (see Figure 5.3 and Figure 5.4) and bottom faces of the anode

The diaphragm was modelled as zero thickness walls. The anode was modelled with a thickness of 6.5 mm. A more detailed view of the anode and diaphragm can be seen in Figure 5.3. A better view of the top of the cell can be seen in Figure 5.4.

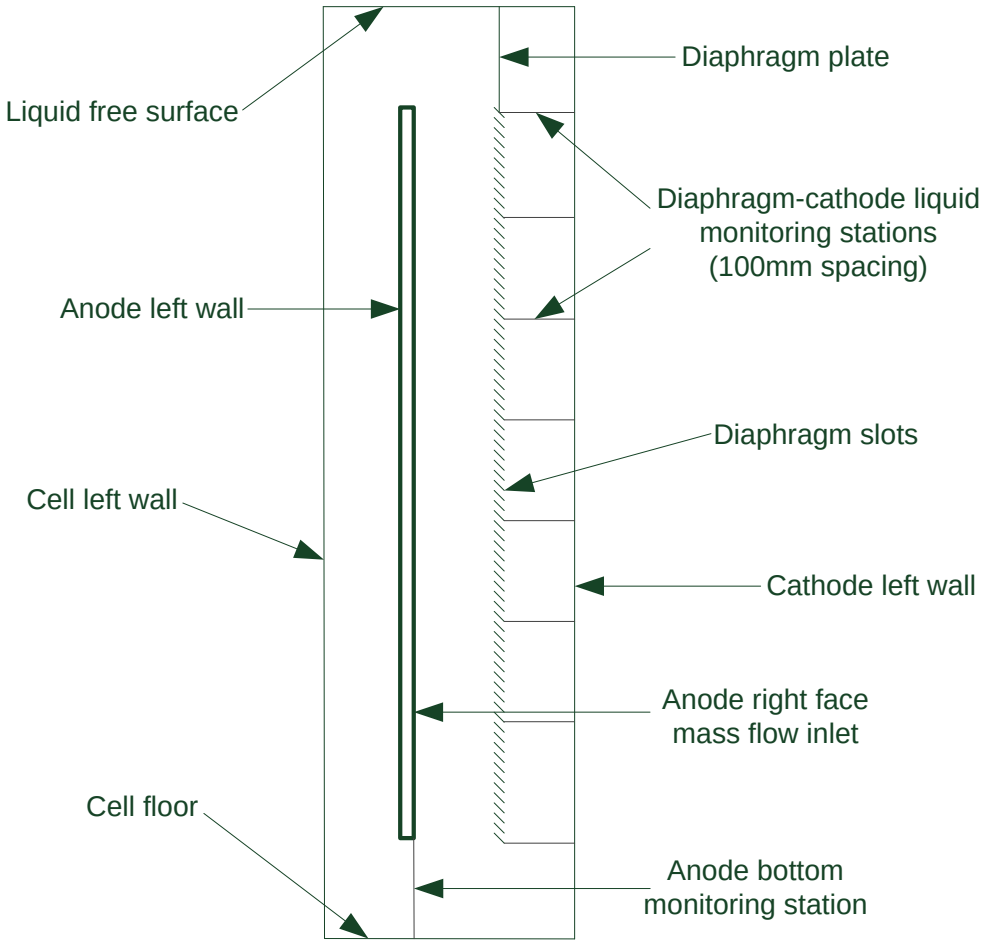

Figure 5.2: Sketch showing the overall view of the cell with the boundaries

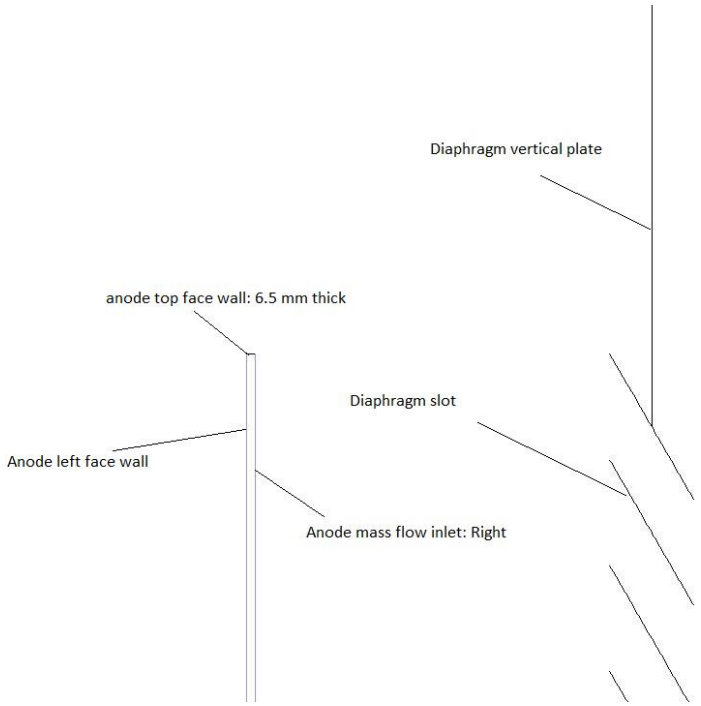

Figure 5.3: Sketch showing the close up view of the anode and diaphragm

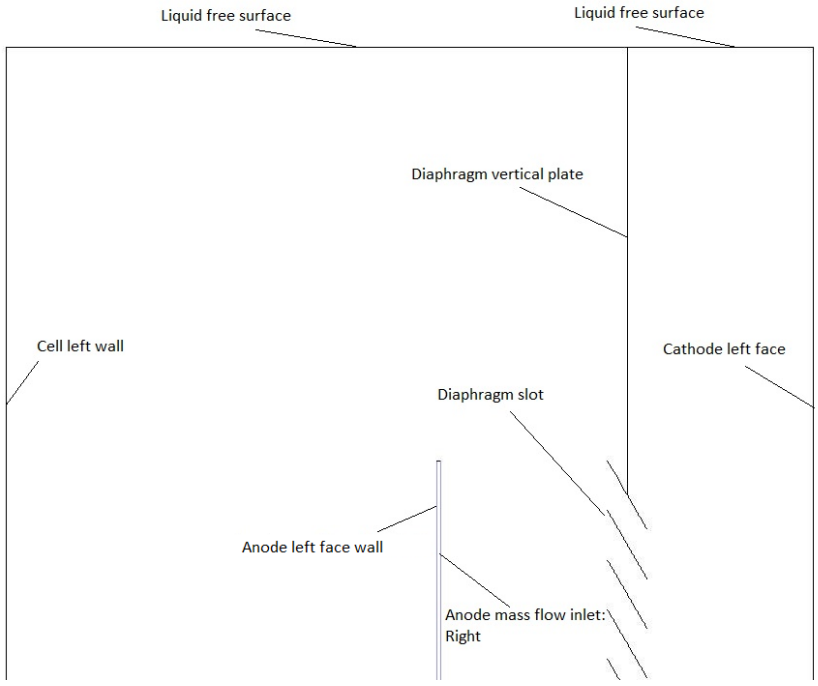

Figure 5.4: Sketch showing a close up view of the top of the cell

5.5. Mass flow inlet: Anode right face

The right face of the anode was a mass flow inlet boundary, as shown in Figure 5.3. The mass flow inlet boundary was an approximation of the electrochemical reaction occurring on the right face of the anode. The electrochemical cell was operated at room temperature and atmospheric pressure. The anode and cathode reactions are presented below.

In this electrochemical system, the oxidation of water to O_2 occurs at the anode and oxygen gas bubbles are evolved at the anode surface. The oxidation half-cell reaction is shown by Equation 5-14:

$$2H_2O \leftrightarrow O_2 + 4H^+ + 4e^- \tag{5-14}$$

On the other hand, the copper ions in solution are reduced at the cathode surface to form copper metal which is then plated on the cathode surface. The reduction half-cell reaction is presented by Equation 5-15:

$$Cu^{2+} + 2e^- \leftrightarrow Cu_{(s)} \tag{5-15}$$

The amount of O_2 gas produced at the anode surface can be calculated by using Faraday's Law which states that the amount of electro-generated gas per unit area is directly proportional to the current density of the cell, as shown in Equation 5-16:

$$\dot{N} = \frac{C_D}{nF} \tag{5-16}$$

where C_D is the current density in C/s/m^2, F is faraday's constant (96485 C/mol), n is the number of electrons transferred in the reaction and n = 4 for the oxygen reaction, $\dot{N}$ is the molar flux in mol/(s m^2).

To convert the molar flux to a volumetric flux, the ideal gas law can be applied. Thus, the volume occupied by one mole of gas can be estimated by using Equation 5-17. The temperature of the system was approximately 298 K and the atmospheric pressure in Pretoria approximately 90 kPa.

$$V = \frac{RT}{P} \tag{5-17}$$

where R is the gas constant at 8.314 J/(mol K), T is the temperature, P is pressure and V is the specific volume in m^3/mol.

The volumetric flux can then be estimated by using Equation 5-18:

$$Q = V\dot{N} \tag{5-18}$$

where Q is the volumetric flux in $m^3/(s\ m^2)$.

To convert the molar flux to a mass flux, the molar mass of O_2 (32 g/mol) can be used as shown in Equation 5-19:

$$m = M_{O_2}\dot{N} \tag{5-19}$$

where m is the mass flux in $g/(s\ m^2)$.

The mass flow inlet condition of oxygen gas production on the anode right face was represented in the form of a mass flow rate, and the mass flow rates for the seven cases investigated are listed in Table 5.1.

Table 5.1: A list of cases tested and their respective mass oxygen gas mass flow rates

Case	Mass flow rate (kg/s)
Base	1.74E-06
Test 1	8.71E-07
Test 2	2.61E-06
Test 3	1.24E-06
Test 4	2.49E-06
Test 5	1.74E-06
Test 6	1.74E-06

5.6. CFD model results

5.6.1. Base case

Figure 5.5 shows the velocity profile of the oxygen gas bubbles as they are produced on the anode surface for the base case. The bubbles rise up due to buoyancy forces and move towards Position A and continue to rise until they disengage at the electrolyte free surface. As seen in Figure 5.5 the velocity of the gas bubbles is at its highest at the anode surface where the gas is generated. As the gas bubbles move further upwards the velocity drops as can be seen in the figure. The bubble velocity immediately above the anode top i.e. Position A was in the range between 0.05 to 0.11 m/s. The highest bubble speed is 0.11 m/s at the anode surface.

The gas bubble flow field observed in the experimental work was slightly different from the model predictions. In the experimental work, the small bubbles accumulated in Position B and in the model velocity profile the bubbles were predicted to exit the system with no bubble accumulation. This might be attributed to the fact that a constant bubble size was assumed in the model and hence these bubbles were predicted to disengage without any accumulation. In the experimental results the bubbles which were observed to accumulate in Position B where the small bubbles.

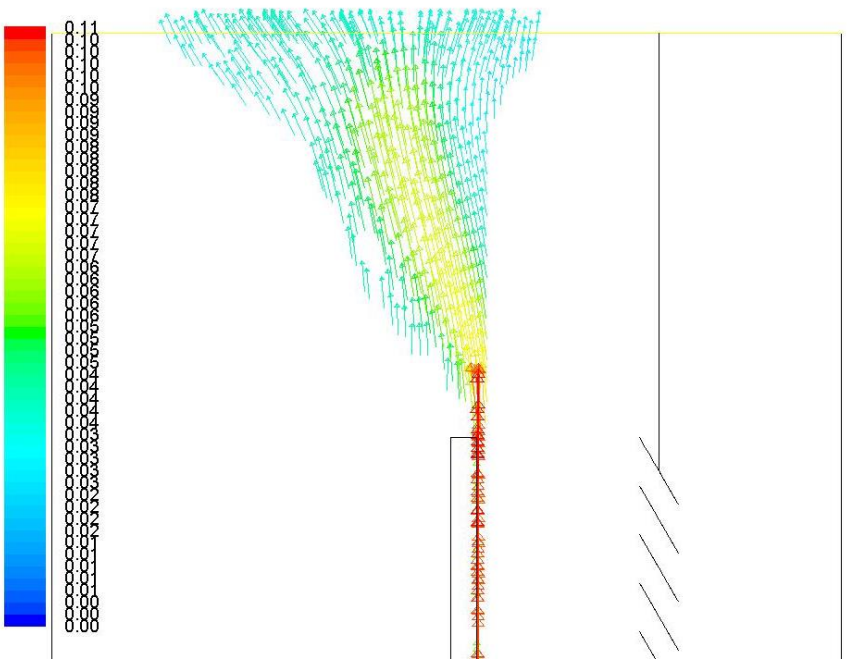

Figure 5.5: Velocity profile of oxygen bubbles at Position A & B for the base case

Figure 5.6 shows the velocity profile of the electrolyte solution at Position A and B for the base case. The electrolyte rises up due to the natural convection created by the rising gas bubbles. The electrolyte follows the flow field of the gas bubbles near and above the anode. It then proceeds to enter Position B where it forms a circulation loop. This is consistent with the observations at Position B in the experimental work whereby the gas bubbles were observed to form a circulation loop at Position B. In the experiments the gas bubbles were used to track the flow field of the electrolyte

In Position A, the electrolyte velocity is in the range 0.04 to 0.07 m/s and in Position B it is in the range 0.01 to 0.03 m/s.

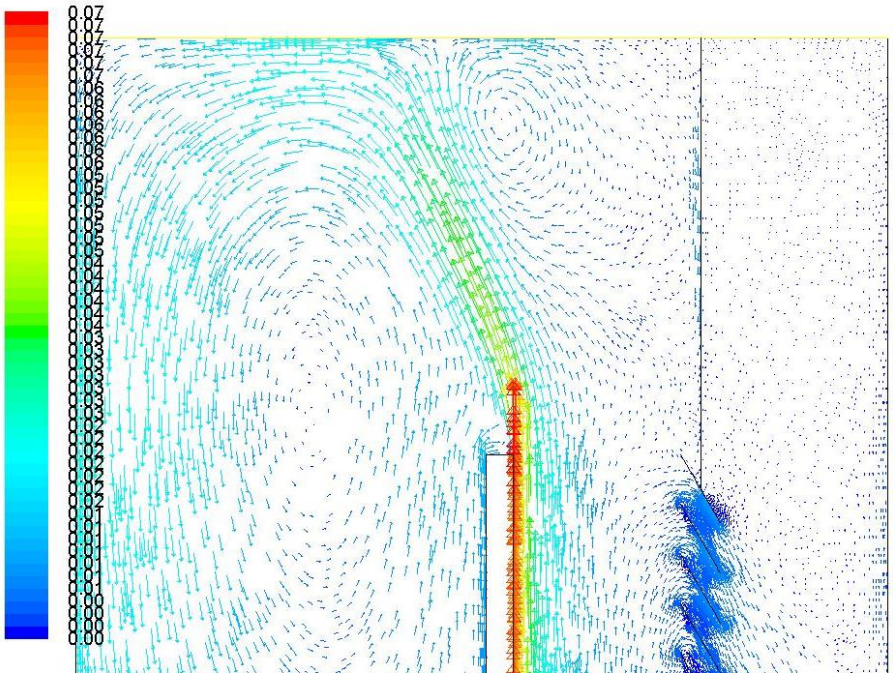

Figure 5.6: Velocity profile of the aqueous $CuSO_4$ solution at Position A & B for the base case

Figure 5.7 shows the velocity profile of the electrolyte solution at Position C for the base case. The electrolyte flow field can be seen forming a circulation pattern at the bottom of the anode. The electrolyte comes down from Position B and circulates at the bottom of the anode before coming up the right face of the anode and also around the diaphragm towards the cathode half. This flow pattern is similar to the one observed in the experimental work, thus confirming the motion of the electrolyte at Position C. The velocity profile predicted by the model is in the range 0 to 0.03 m/s for the base case.

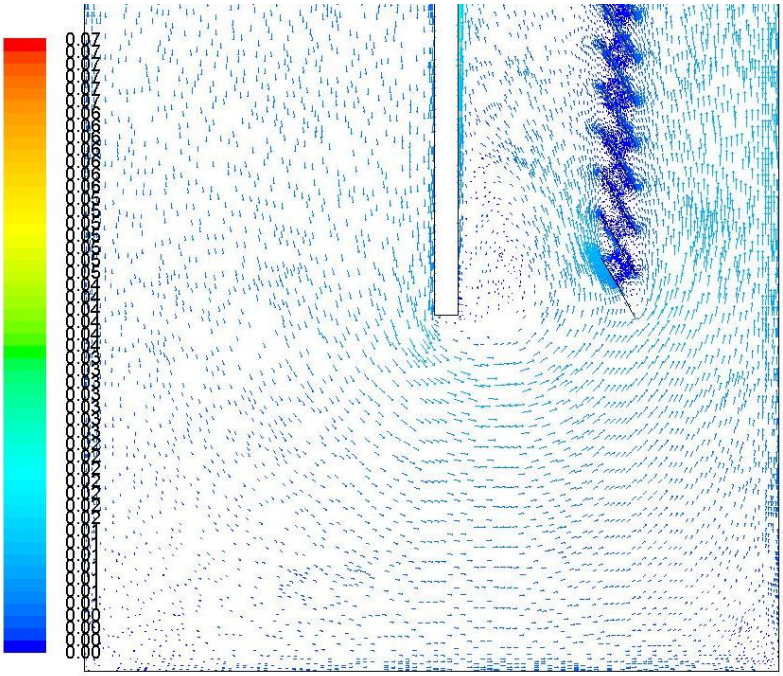

Figure 5.7: Velocity profile of the aqueous $CuSO_4$ solution at Position C for the base case

Figure 5.8 shows the velocity profile of the electrolyte solution in the gap between the anode and diaphragm for the base case. The velocity at the surface of the anode does not seem to change much and it is at its highest value. This is mainly because the bubbles are produced at the anode surface where the forces causing the upwards movement are the highest.

Another important thing to note is the movement of the electrolyte near the diaphragm, it seems like the electrolyte is almost stagnant around the diaphragm slots. This has a potential to cause the gas bubbles to be also stuck in between the diaphragm slots and not crossover to the cathode half. Since the electrolyte velocity is lower near the diaphragm slots, it shows that the driving force for the electrolyte flow in that area is low. With that said, it can be deduced

that there are less gas bubbles in the area next to the diaphragm. This was in fact observed in the experimental work conducted.

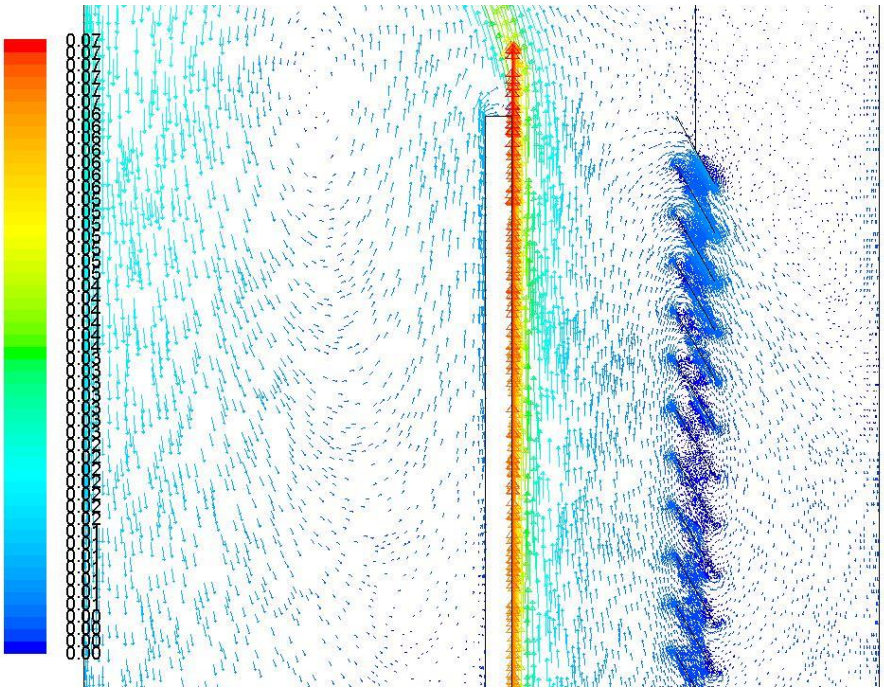

Figure 5.8: Velocity profile of the aqueous $CuSO_4$ solution at Position D for the base case

5.6.2. Test 1: Current density

Figure 5.9 shows the velocity profile of the oxygen gas bubbles at Position A and B. The bubble flow field seems to be following a similar flow pattern to the base case. The only difference is the magnitude of the flow since Test 1 was conducted at 50 A/m^2. The amount of bubbles generated is lower than the base case and the velocity profile is also lower. The velocity profile shows a range of 0.04 to 0.10 m/s with the highest velocity at the anode surface.

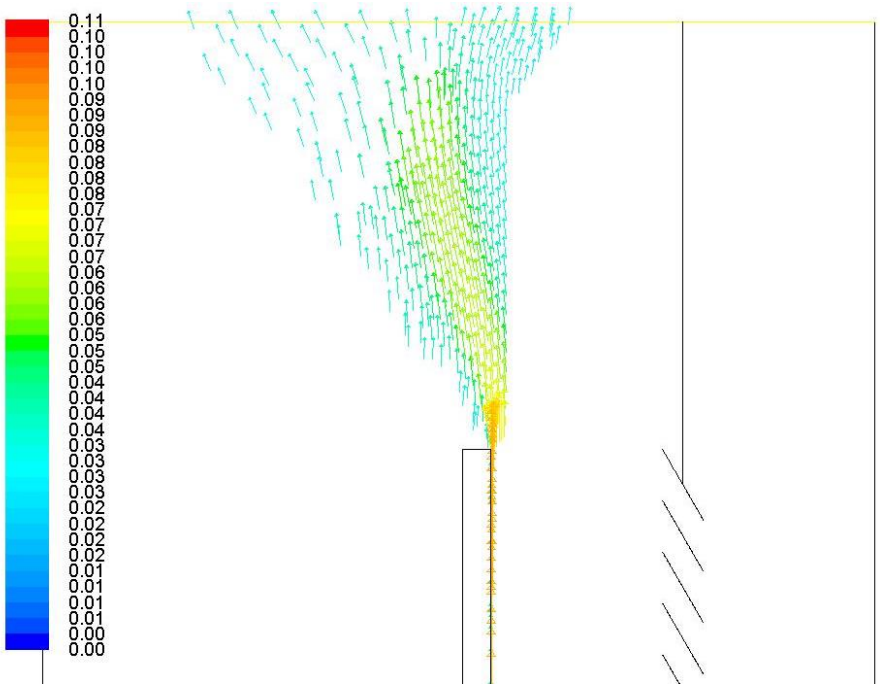

Figure 5.9: Velocity profile of oxygen bubbles at Position A & B for Test 1

Figure 5.10 shows the velocity profile of the electrolyte solution at Position A and B for Test 1. The electrolyte flow field is similar to the one observed in the base case with the only difference in the velocity of the electrolyte. The circulation loop formed is not as fast as in the base case. There is a lower driving force in Test 1 and hence the velocities were expected to be slightly lower than the base case. The highest velocity which is near the anode surface 0.06 m/s in Test 1 compared to the 0.07 m/s in the base case. As the electrolyte moves towards Position B, the velocity drops and the velocity profile in Position B is 0.01 to 0.02 m/s.

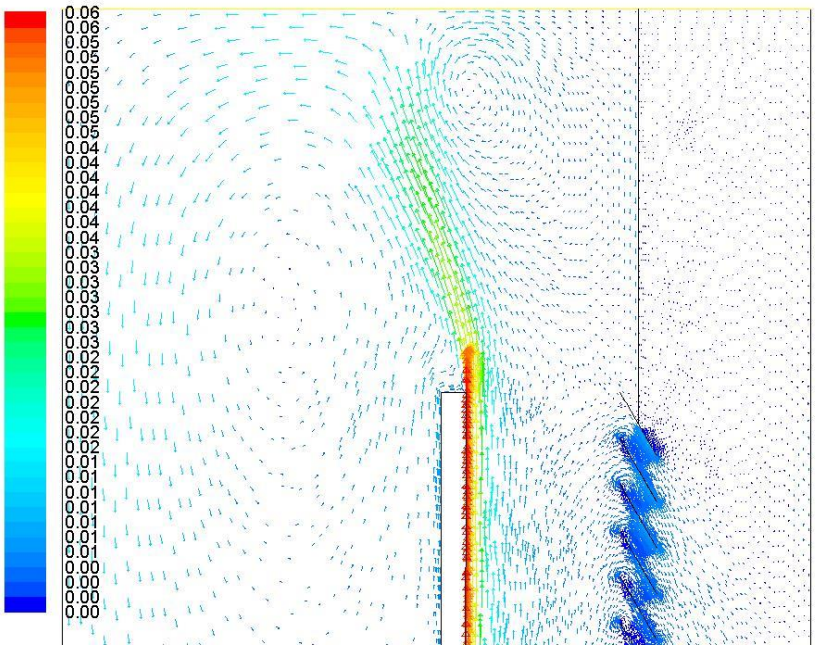

Figure 5.10: Velocity profile of the aqueous $CuSO_4$ solution at Position A & B for Test 1

Figure 5.11 shows the velocity profile of the electrolyte solution at Position C for Test 1. The electrolyte follows a similar circulation pattern as observed in the base case with electrolyte the circulation loop at the bottom of the anode. The velocity profile predicted for the electrolyte at Position C is in the range from 0.01 to 0.02 m/s.

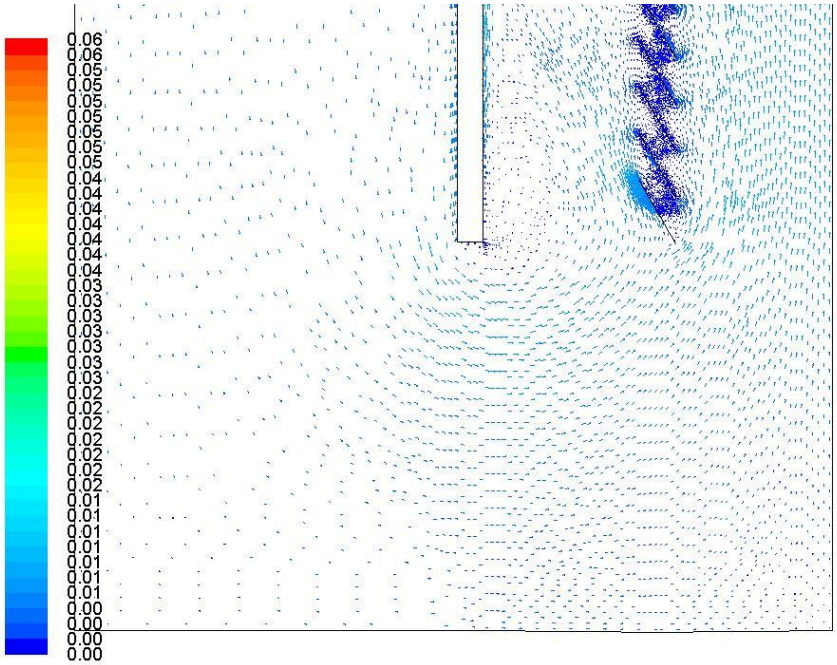

Figure 5.11: Velocity profile of the aqueous $CuSO_4$ solution at Position C for Test 1

Figure 5.12 shows the velocity profile of the electrolyte solution at Position D for Test 1. The electrolyte has the highest speed at the anode surface where the bubbles are generated. As expected, the velocity profiles for Test 1 are slightly lower than in the base case. Furthermore, it seems like the lower electrolyte velocities result into more of the electrolyte being trapped in between the diaphragm slots. This might be attributed to the lower driving force due to the lower amount of bubbles produced at the anode.

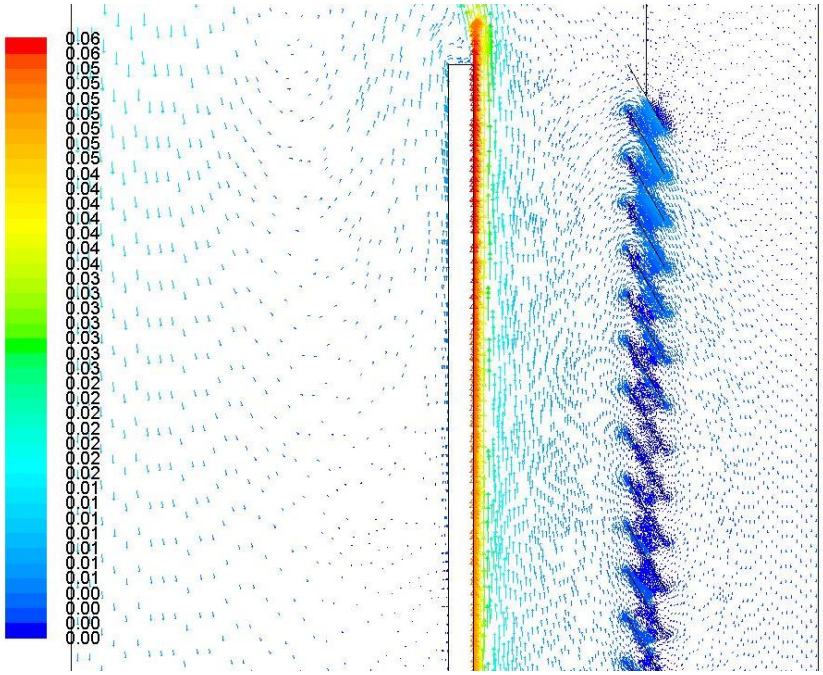

Figure 5.12: Velocity profile of the aqueous $CuSO_4$ solution at Position D for Test 1

5.6.3. Test 2: Current density

Figure 5.13 shows the velocity profile of the oxygen gas bubbles at Position A and B. The bubble flow field seems to be following a similar flow pattern to the base case with slightly more bubble flowing towards the left wall of the cell. The velocity profile in Test 2 is higher than that of the base case. This was expected as the amount of gas bubbles produced in Test 2 is proportional to the higher current density. As a result, the buoyancy induced flow was enhanced due to the higher driving forced caused by the bubble evolution. The model prediction shows a maximum bubble velocity of 0.13 m/s at the surface of the anode.

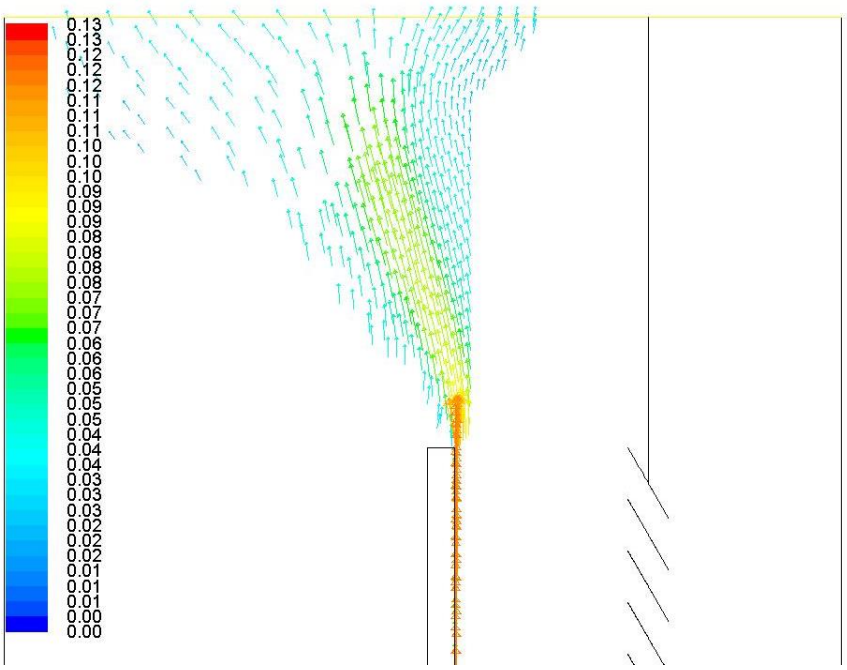

Figure 5.13: Velocity profile of oxygen bubbles at Position A & B for Test 2

Figure 5.14 shows the velocity profile of the electrolyte solution at Position A and B for Test 2. The electrolyte flow field is similar to the one observed in the above cases and the differences are in the magnitude of the profile. The current density in Test 2 is the highest and there are more gas bubbles generated which causes a higher driving force for the electrolyte flow. Hence, the velocity profile predicted for Test 2 gave a maximum of 0.09 m/s at the anode face and this was higher than the velocities in Test 1 and the base case. The circulation loop formed in Position B is in the range of 0.01 to 0.04 m/s which is higher than Test 1 and the base case.

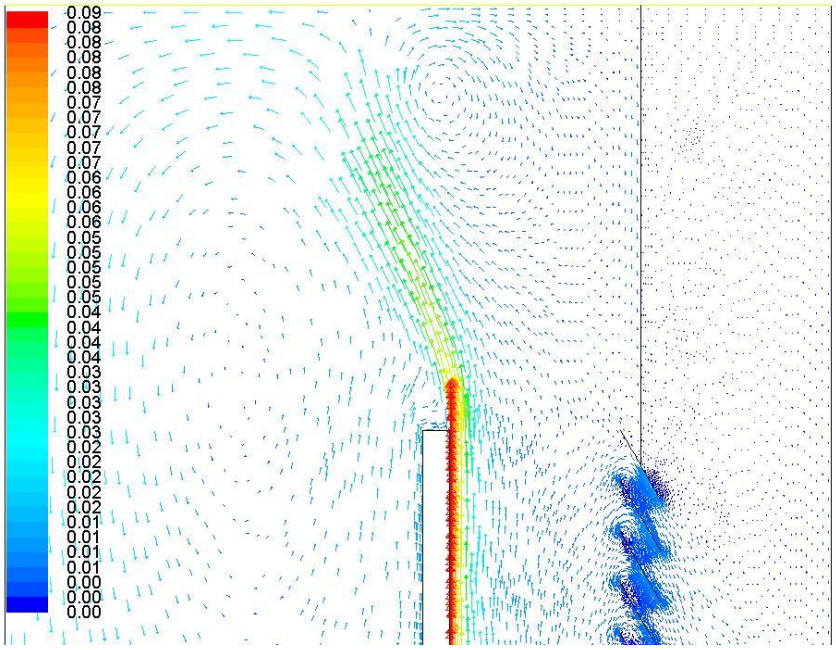

Figure 5.14: Velocity profile of the aqueous $CuSO_4$ solution at Position A & B for Test 2

Figure 5.15 shows the velocity profile of the electrolyte solution at Position C for Test 2. The electrolyte follows a similar circulation pattern as observed in the above cases. The velocity profile predicted for the electrolyte at Position C is in the range from 0 to 0.03 m/s.

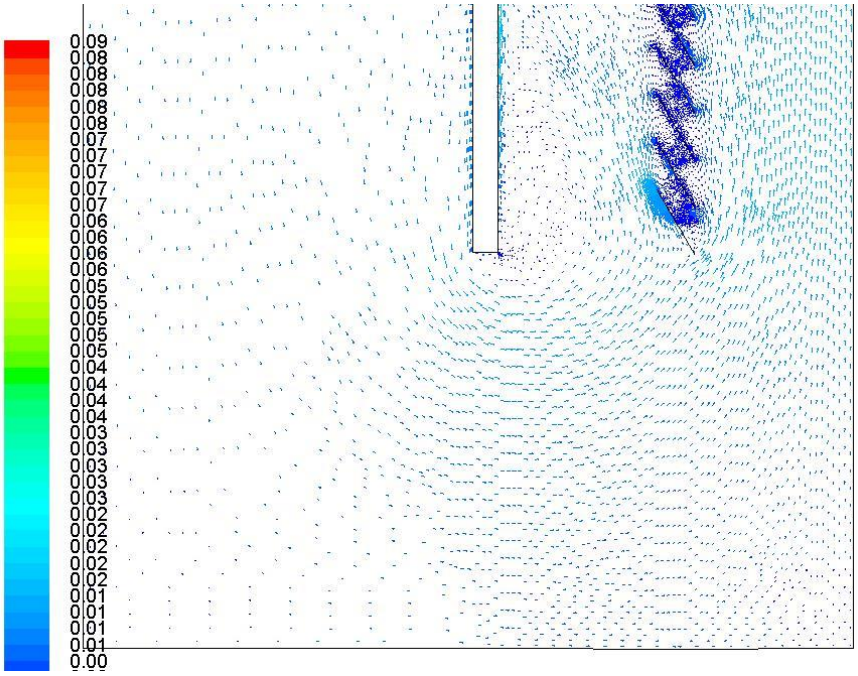

Figure 5.15: Velocity profile of the aqueous $CuSO_4$ solution at Position C for Test 2

Figure 5.16 shows the velocity profile of the electrolyte solution at Position D for Test 2. The electrolyte velocity is the highest in the area close to the anode surface. The electrolyte has the highest speed at the anode surface where the bubbles are generated. The velocity profiles for Test 2 are higher than in the other cases because of the high current density. As observed in the other cases, it seems like the electrolyte gets trapped in the space between the diaphragm slots.

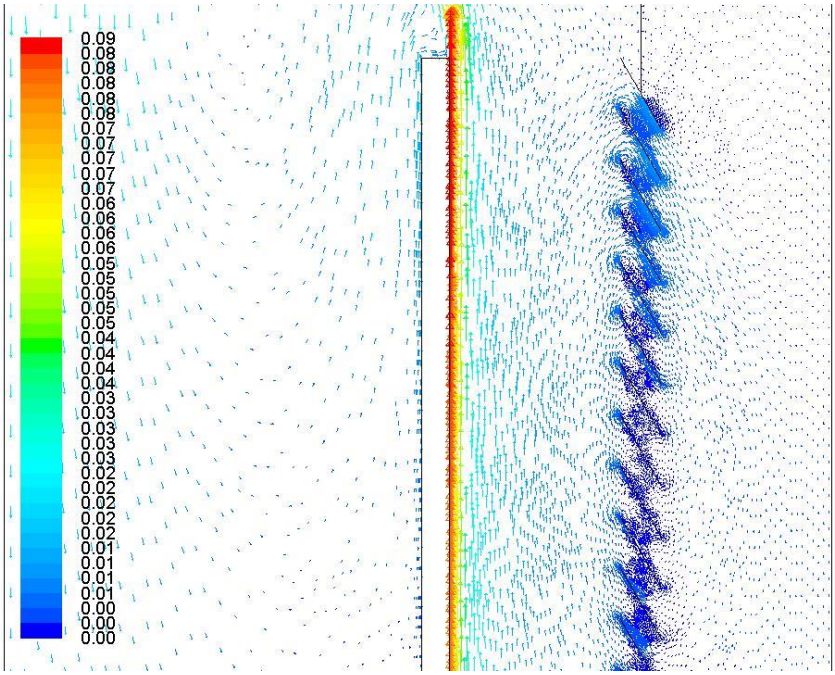

Figure 5.16: Velocity profile of the aqueous $CuSO_4$ solution at Position D for Test 2

5.6.4. Test 3: Anode height

Figure 5.17 shows the velocity profile of the oxygen gas bubbles at Position A and B for Test 3. The bubbles are concentrated in the region above the anode and they do not move towards Position B. The highest bubble velocities are observed not only on the anode surface but also immediately above the anode in Position A. The model prediction shows a maximum bubble velocity of 0.09 m/s in those areas indicated by the red arrows in Figure 5.17. Test 3 had the smallest anode height and the reduced area of the anode caused a reduction in the amount of evolved gas bubbles.

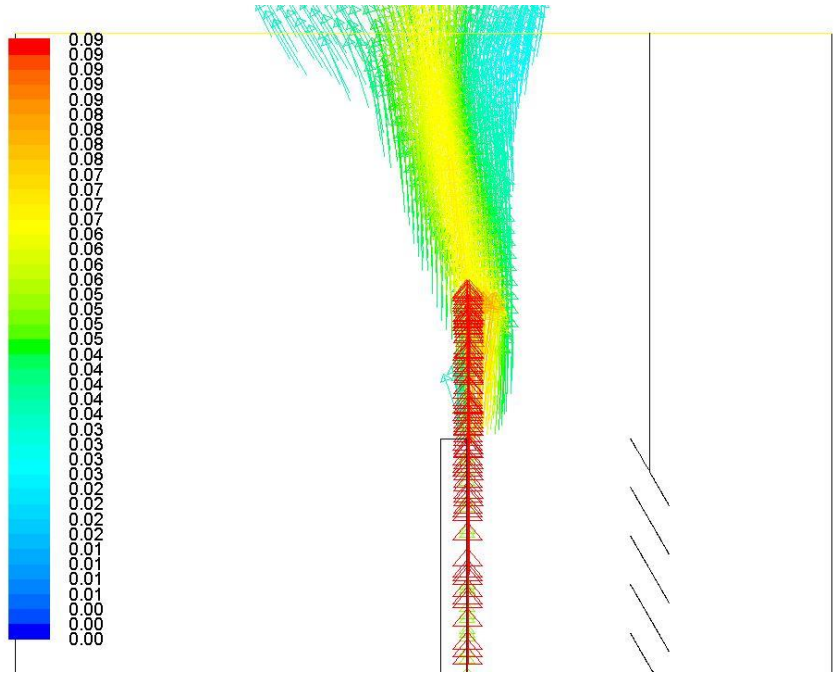

Figure 5.17: Velocity profile of oxygen bubbles at Position A & B for Test 3

Figure 5.18 shows the velocity profile of the electrolyte solution at Position A and B for Test 3. The electrolyte flow field is similar to the other cases and as described in the base case. The circulation loop in Position B is in the range of 0.01 to 0.03 m/s.

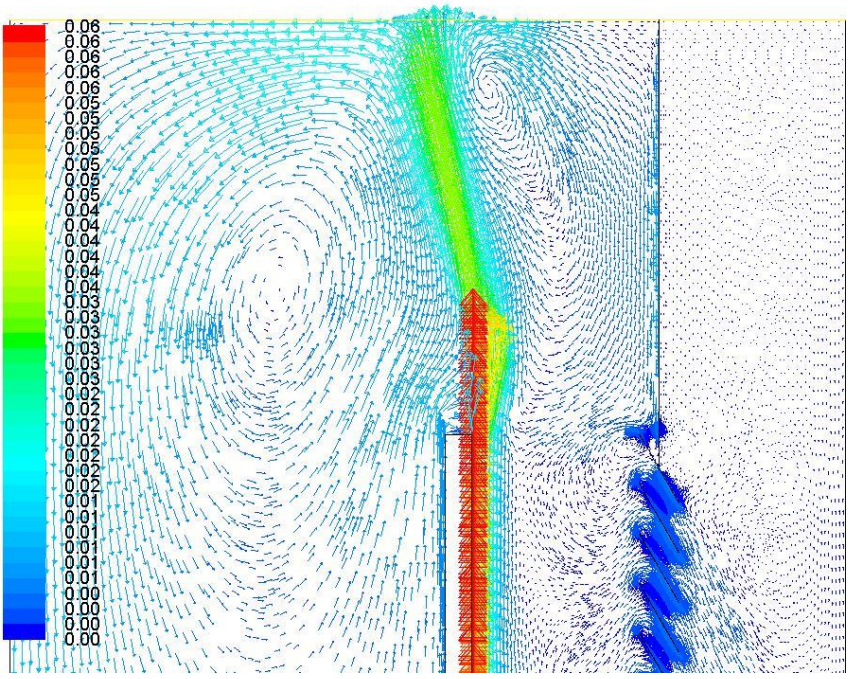

Figure 5.18: Velocity profile of the aqueous $CuSO_4$ solution at Position A & B for Test 3

Figure 5.19 shows the velocity profile of the electrolyte solution at Position C for Test 3. The electrolyte follows a similar circulation pattern as observed in the above cases. The velocity profile predicted for the electrolyte at Position C is in the range from 0 to 0.02 m/s.

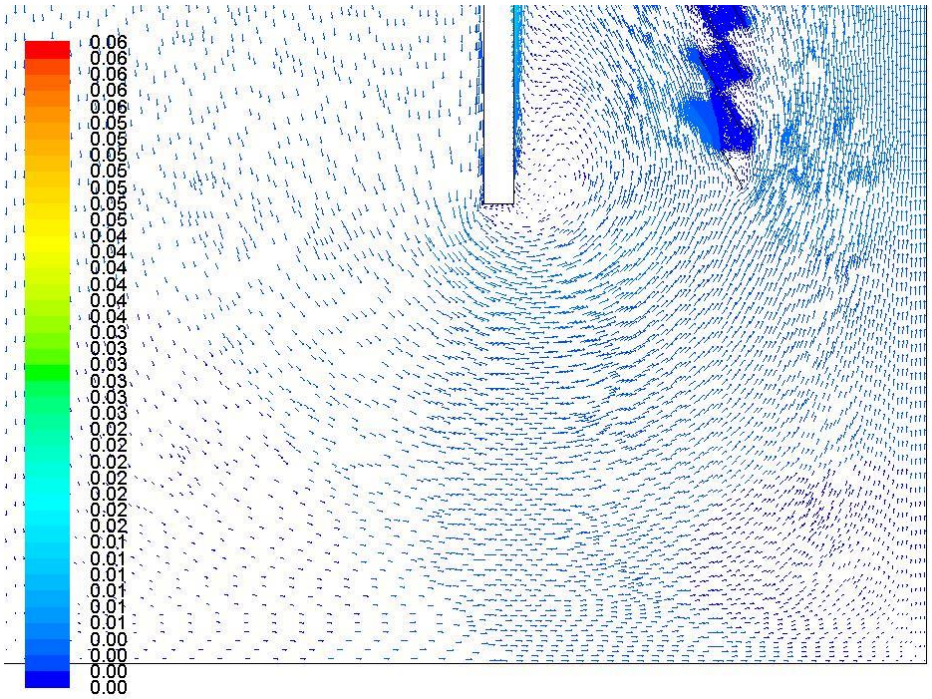

Figure 5.19: Velocity profile of the aqueous $CuSO_4$ solution at Position C for Test 3

Figure 5.20 shows the velocity profile of the electrolyte solution at Position D for Test 3. The electrolyte velocity is the highest in the area close to the anode surface and the velocity drops with the distance away from the anode. The electrolyte has the highest speed at the anode surface where the bubbles are generated due to the high driving force in that area. The highest electrolyte velocity in Position D is 0.06 m/s and this is at the anode surface.

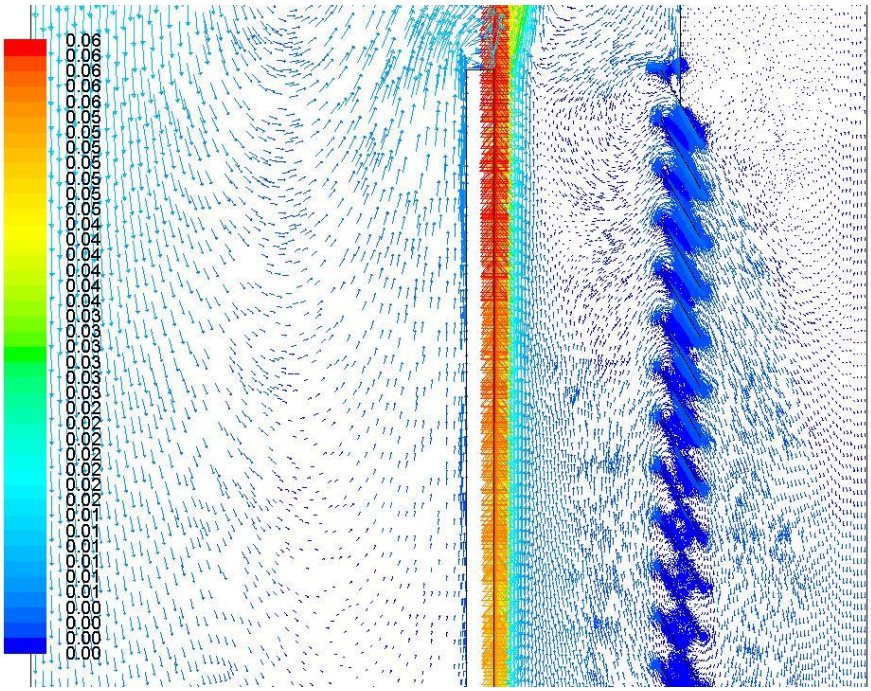

Figure 5.20: Velocity profile of the aqueous $CuSO_4$ solution at Position D for Test 3

5.6.5. Test 4: Anode height

Figure 5.21 and Figure 5.22 shows the velocity profiles of the oxygen gas bubbles as they are produced on the anode surface and rise up towards Position A and B. Test 4 used the largest anode height (1 m) and thus the surface area for gas evolution was bigger in this case. Consequently, the amount of gas bubbles generated on the anode was higher than the other cases. The buoyancy force driving the fluid flow is affected by the amount of gas bubbles produced and this can be observed in Figure 5.21 and Figure 5.22.

This was also observed in the experimental work as discussed in section 4.4. The large amounts of bubbles produced create a higher buoyancy force which is the main force responsible for the upwards fluid flow. The effect of this increased driving force can be seen in the velocity profiles shown in Figure 5.21 which shows high bubble velocities. The predicted bubble velocity near the anode surface is in the range of 0.13 to 0.25 m/s.

This high driving force causes the bubble flow field to extend towards the left wall of the cell. The bubbles tend to push more of the electrolyte towards the left wall and in the process some of the bubbles are dragged towards the wall by the electrolyte. Additionally, when the amount of bubbles generated is high, the bubbles do not disengage quickly and they tend to accumulate in Position B. This flow pattern was also observed in the experimental and it is

discussed in section 4.4. The resulting electrolyte flow in Position B is so high that it forces some of the bubbles accumulating in Position B downwards. This phenomenon is evident in Figure 5.21 where the bubbles are shown to be moving downwards in the space behind the anode.

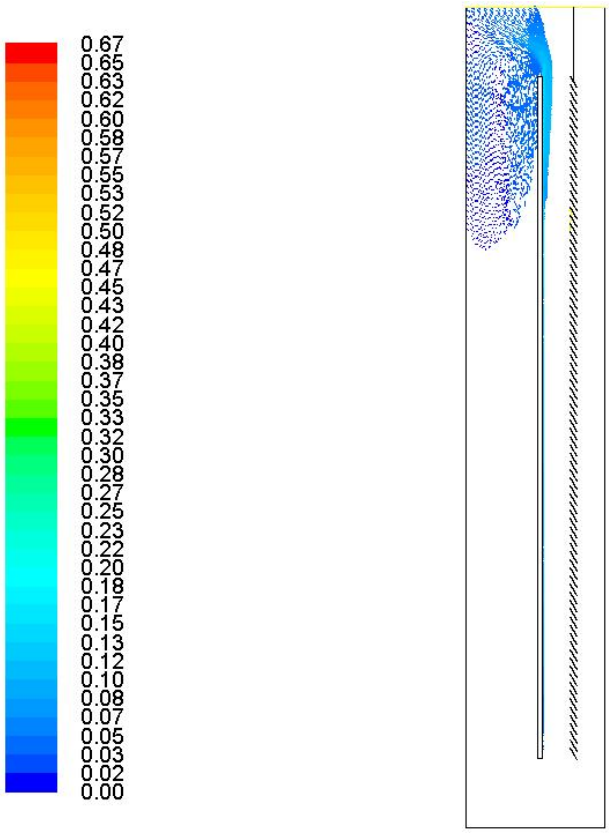

Figure 5.21: Velocity profile of oxygen bubbles at Position A & B for the Test 4

The circulation loop in Position B is formed further down than observed in the other cases. This can be attributed to the higher electrolyte flow in Position B which was mainly due to the increased amount of gas bubble produced on the anode.

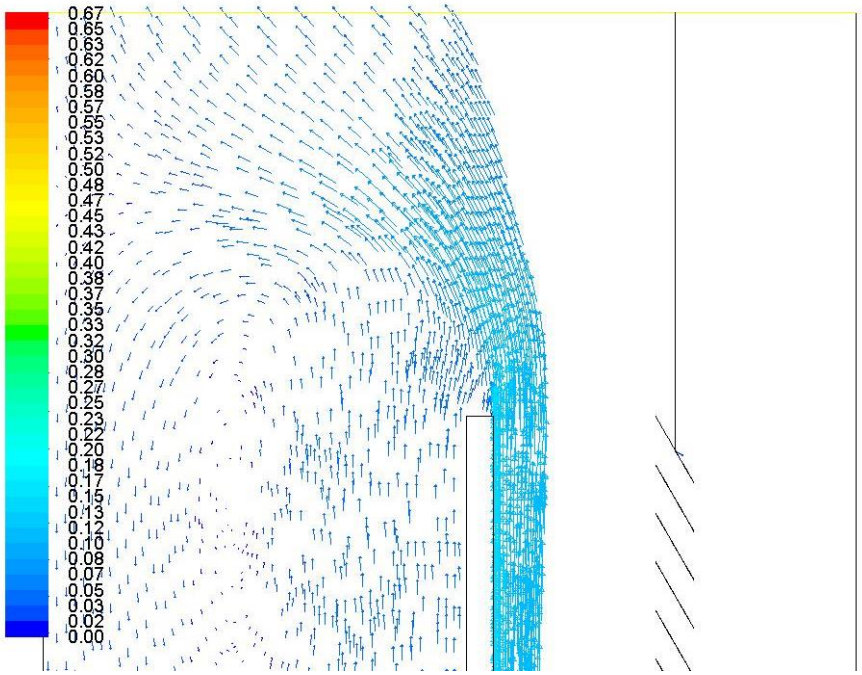

Figure 5.22: A closer look at the velocity profile of the oxygen bubbles at Position A & B

Figure 5.23 shows the velocity profile of the electrolyte solution at Position A and B for Test 4. The high driving force created by the evolved bubbles results into a higher bubble speed and electrolyte speed. This in turn creates a higher electrolyte flow as can be observed in Figure 5.23. The electrolyte flow field is shown to move towards the electrolyte level at the top and the left wall of the cell, deflecting from these surfaces and then moving downwards. The electrolyte velocity in Position A is in the range of 0.02 to 0.1 m/s.

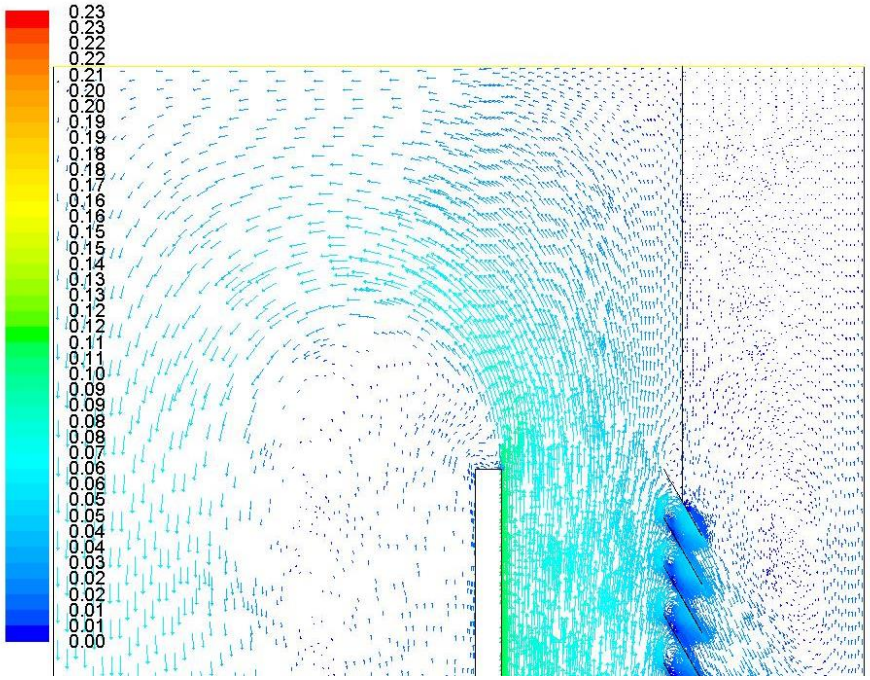

Figure 5.23: Velocity profile of the aqueous $CuSO_4$ solution at Position A & B for Test 4

Figure 5.24 shows the velocity profile of the electrolyte solution at Position C for Test 4. Since there is a higher driving force in the system, the circulation loop at the bottom has higher velocities. The flow field at the bottom of the cell is shown to extend more towards the diaphragm-cathode gap. The electrolyte velocity in this gap is in the range of 0.05 to 0.08 m/s which is much higher than the velocities observed in the other cases. The velocity profile predicted for the electrolyte at Position C is in the range from 0.01 to 0.08 m/s.

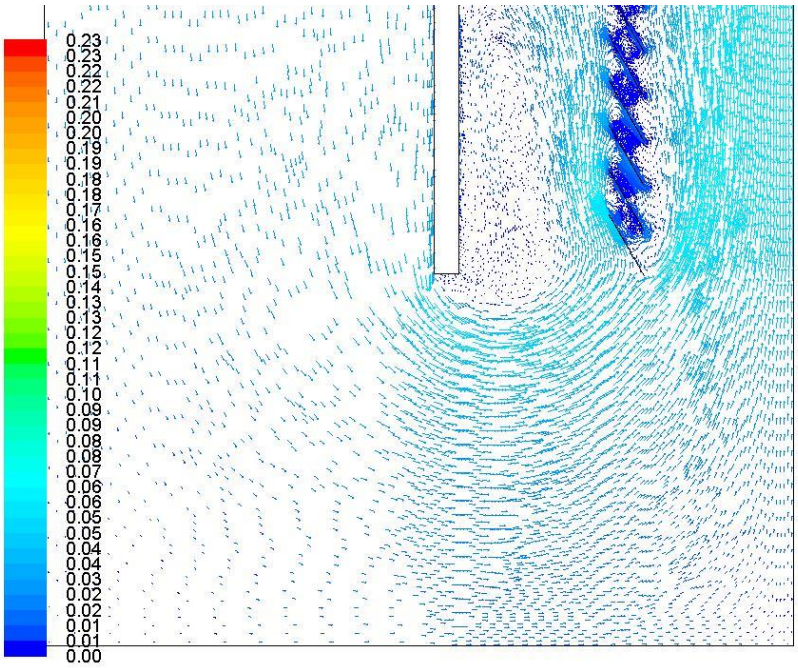

Figure 5.24: Velocity profile of the aqueous $CuSO_4$ at Position C for Test 4

Figure 5.25 shows the velocity profile of the electrolyte solution at Position D for Test 4. The electrolyte velocity in this case is higher than all the other cases. The electrolyte velocity in the anode-diaphragm channel is high; it is in the range from 0.04 to 0.09 m/s. The highest electrolyte velocity in Position D is 0.13 m/s and this is at the anode surface.

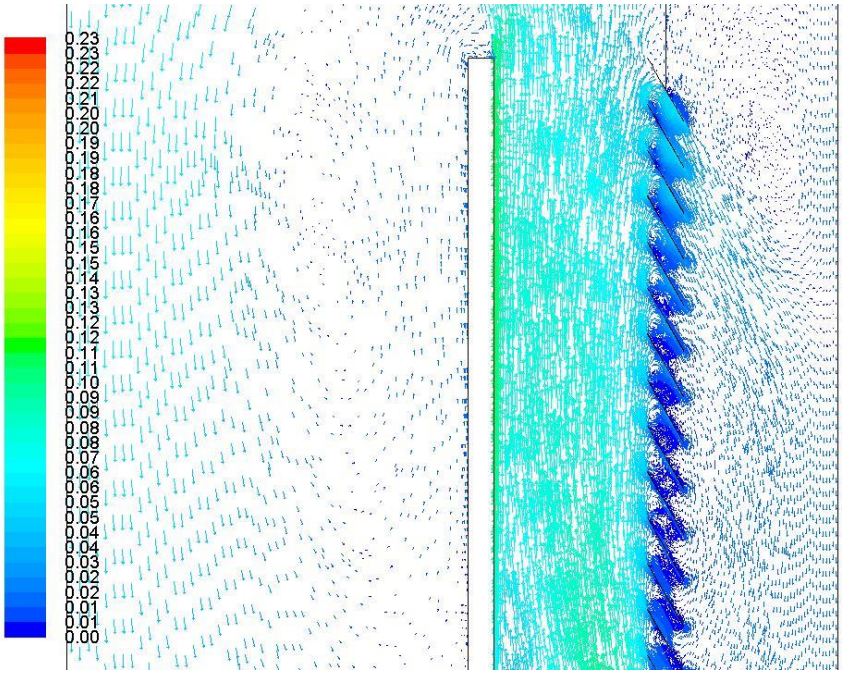

Figure 5.25: Velocity profile of the aqueous $CuSO_4$ at Position D for Test 4

The velocity profiles predicted from Test 4 were much higher than all the other cases. The higher bubble and electrolyte velocities create a higher electrolyte circulation rate in the system. This has a number of benefits to the performance of the cell and some of these were discussed in section 4.4.

5.6.6. Test 5: Inter-electrode gap

Figure 5.26 shows the velocity profile of the oxygen gas bubbles at Position A and B for Test 5. The bubble flow field pattern shows the bubbles flowing above the anode and slightly towards the left wall of the cell. The model prediction shows a maximum bubble velocity of 0.12 m/s which can be observed on the anode surface.

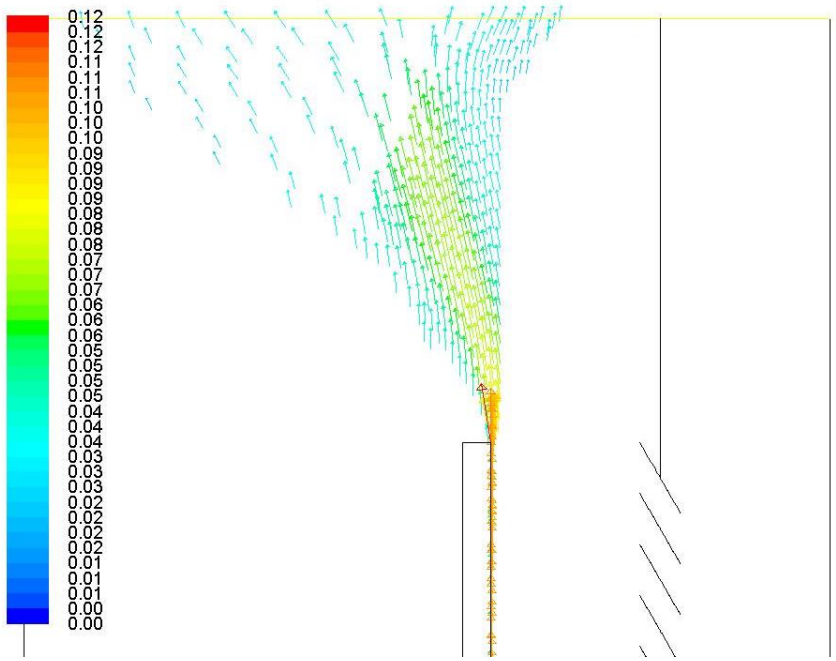

Figure 5.26: Velocity profile of oxygen bubbles at Position A & B for Test 5

Figure 5.27 shows the velocity profile of the electrolyte solution at Position A and B for Test 5. The electrolyte flow field is similar to the other cases as described in the base case. The circulation loop in Position B is in the range of 0.01 to 0.03 m/s.

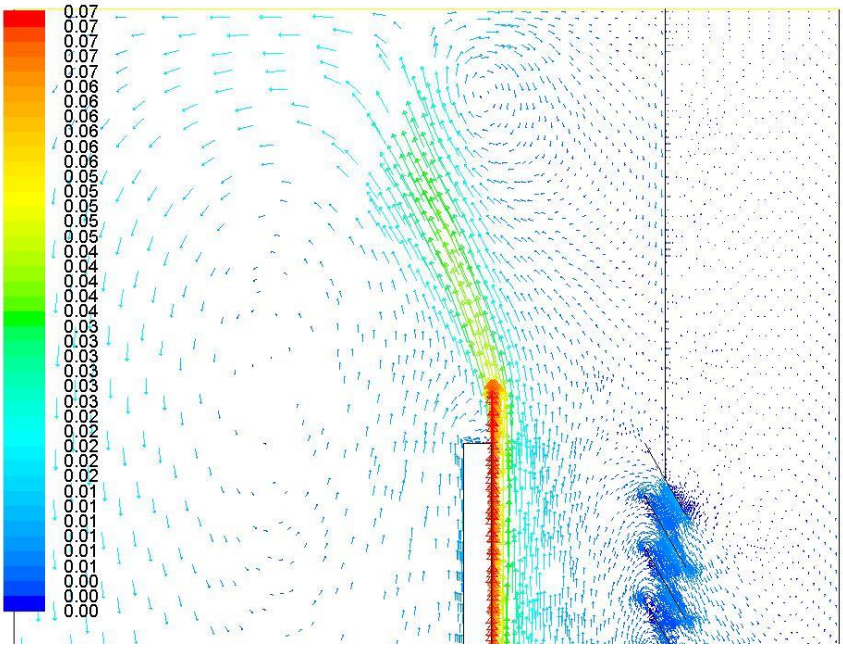

Figure 5.27: Velocity profile of the aqueous $CuSO_4$ solution at Position A & B for Test 5

Figure 5.28 shows the velocity profile of the electrolyte solution at Position C for Test 5. The electrolyte follows a similar circulation pattern as observed in the above cases but the magnitude of the flow is different to the other cases. The velocity profile predicted for the electrolyte at Position C is in the range from 0 to 0.03 m/s.

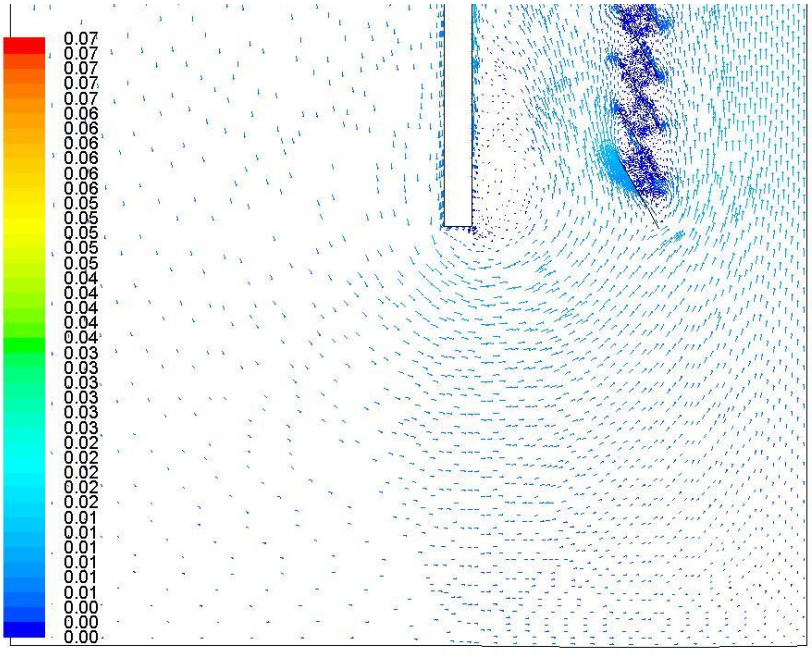

Figure 5.28: Velocity profile of the aqueous $CuSO_4$ solution at Position C for Test 5

Figure 5.29 shows the velocity profile of the electrolyte solution at Position D for Test 5. The electrolyte has the highest speed at the anode surface where the bubbles are generated because of the high driving forces in that area. The model predictions show the highest electrolyte velocity to be 0.07 m/s measured on the anode surface.

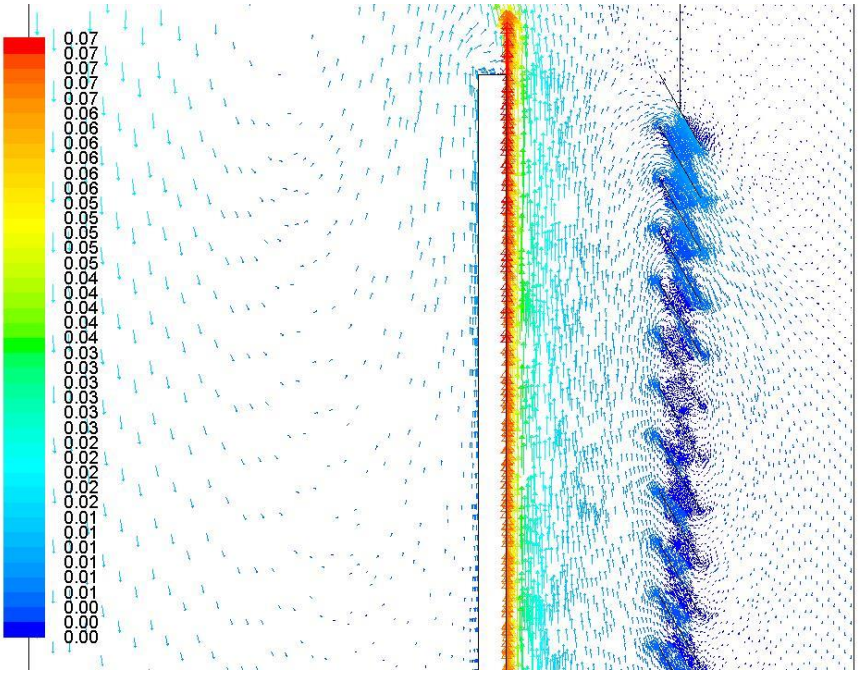

Figure 5.29: Velocity profile of the aqueous $CuSO_4$ solution at Position D for Test 5

5.6.7. Test 6: Inter-electrode gap

Figure 5.30 shows the velocity profile of the oxygen gas bubbles at Position A and B for Test 6. The bubble flow field move upwards passing through Position A and slightly drift towards Position B. The highest bubble velocities are observed on the anode surface and the model prediction shows a maximum bubble velocity of 0.11 m/s.

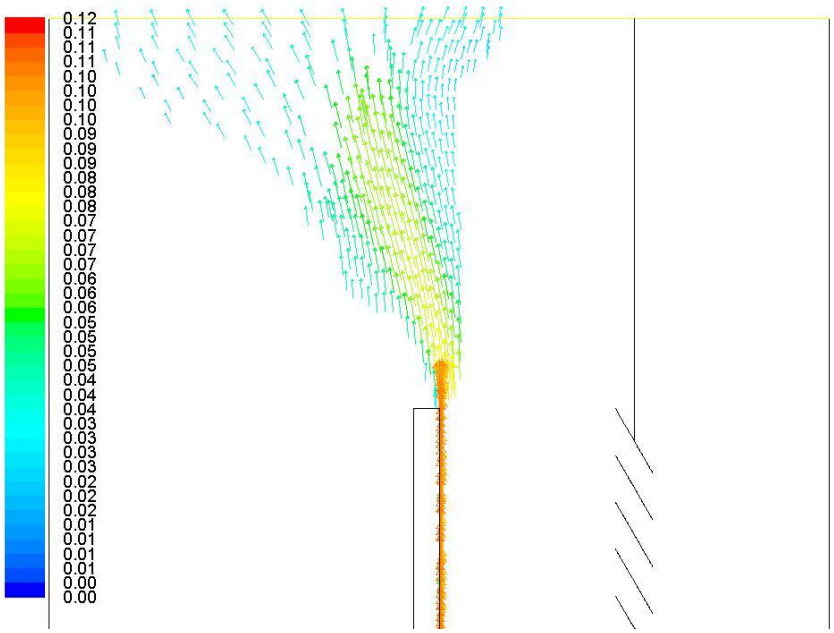

Figure 5.30: Velocity profile of oxygen bubbles at Position A & B for Test 6

Figure 5.31shows the velocity profile of the electrolyte solution at Position A and B for Test 6. The electrolyte flow field shows the electrolyte moving upwards from the anode surface and passing through Position A before moving towards Position B. A circulation loop is observed in Position B and the electrolyte speeds is in the range of 0.01 to 0.03 m/s. The highest electrolyte speed is observed at the anode surface and it is 0.07 m/s.

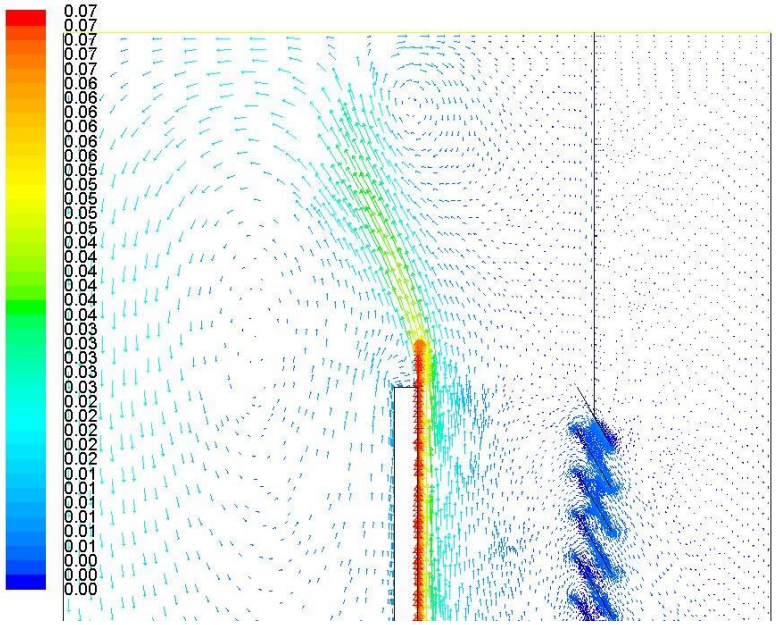

Figure 5.31: Velocity profile of the aqueous $CuSO_4$ solution at Position A & B for Test 6

Figure 5.32 shows the velocity profile of the electrolyte solution at Position C for Test 6. The electrolyte follows a similar circulation pattern as observed in the above cases. The velocity profile predicted for the electrolyte flow at Position C is in the range from 0.01 to 0.03 m/s.

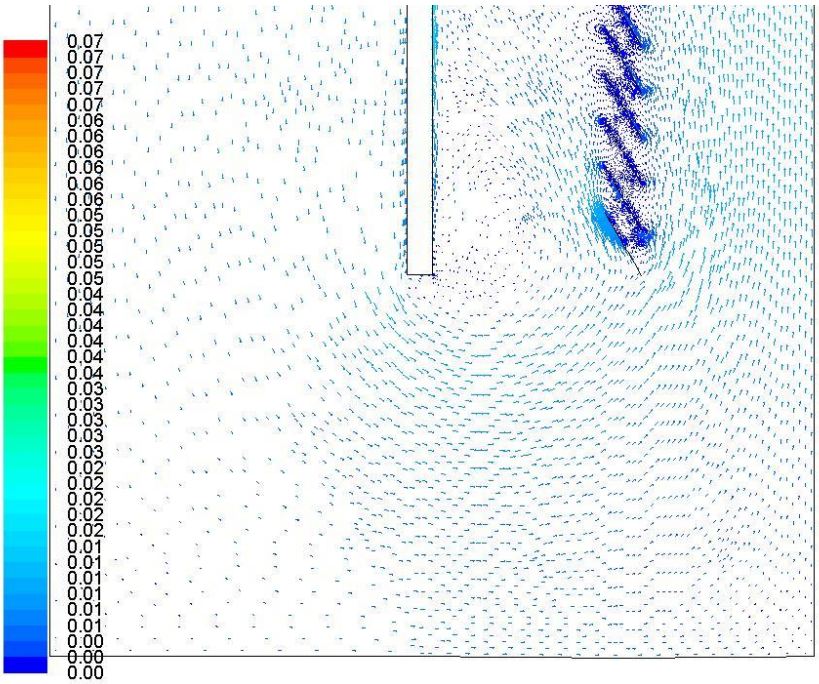

Figure 5.32: Velocity profile of the aqueous $CuSO_4$ solution at Position C for Test 6

Figure 5.33 shows the velocity profile of the electrolyte solution at Position D for Test 6. The electrolyte has the highest speed at the anode surface where the bubbles are generated because the driving force is higher in that region. The model prediction shows the highest electrolyte velocity in Position D of 0.07 m/s and this is at the anode surface.

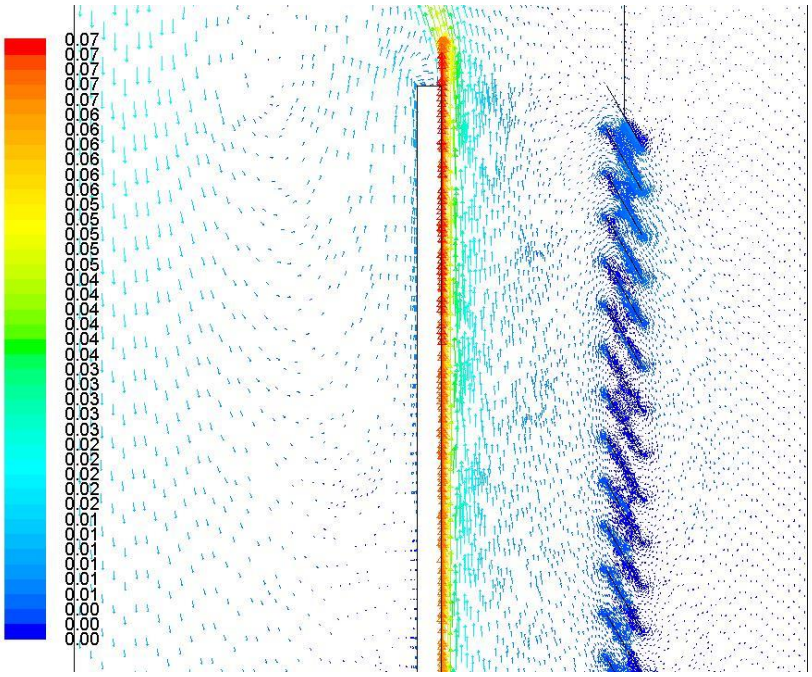

Figure 5.33: Velocity profile of the aqueous $CuSO_4$ solution at Position D for Test 6

Test 4 showed the highest bubble speed predicted by the model in the area above the anode surface compared to the other cases. This was mainly because the anode in Test 4 had a bigger surface area for gas production and the increased number of bubbles produced created a higher driving force. The lowest predicted bubble speed on the anode surface was 0.09 m/s for Test 3. This was the smallest anode height which had the least amount of gas generated on anode.

Test 4 predicted the highest electrolyte speed in Position B compared to the other cases. Again, this can be attributed to the increased number of bubbles generated in Test 4. In Position C and D, Test 4 also predicted the highest electrolyte speeds.

5.7. Experiment vs. CFD model

The experimental results were compared to the model predictions with the aim to validate the model predictions. The results were compared at specific points within the cell. The gas bubbles were tracked within the range given in the plane length and the average bubble speed was measured in that range. The plane length was measured from the bottom of the cell to the top and it represents Position A. Table 5.2 presents the comparison between the bubble speeds obtained by in the experiments and the model predictions with their error values. The gas bubble speeds predicted by the model were in reasonable agreement to those measured in

the experiments as can be seen in Table 5.2. Test 4 had the lowest error at 6% and the highest error was 29% for Test 2.

Table 5.2: Comparison of the bubble speeds obtained from the experiment and the model predictions

Test	Plane length (mm)	Model speed (mm/s)	Experiment speed (mm/s)	Error (%)
Base case	804-806	79	102	23%
Test 1	805-807	68	59	13%
Test 2	814-816	79	111	29%
Test 3	504-506	49	44	10%
Test 4	1010-1012	106	113	6%
Test 5	805-807	77	103	25%
Test 6	808-810	78	85	8%

The data presented in Table 5.2 was plotted in a graph for each of the parameters tested. Figure 5.34 shows an increase in bubble speed with increasing current density for both the model and experiment results. The model does not show a big change in the bubble speed from 100 to 150 A/m^2.

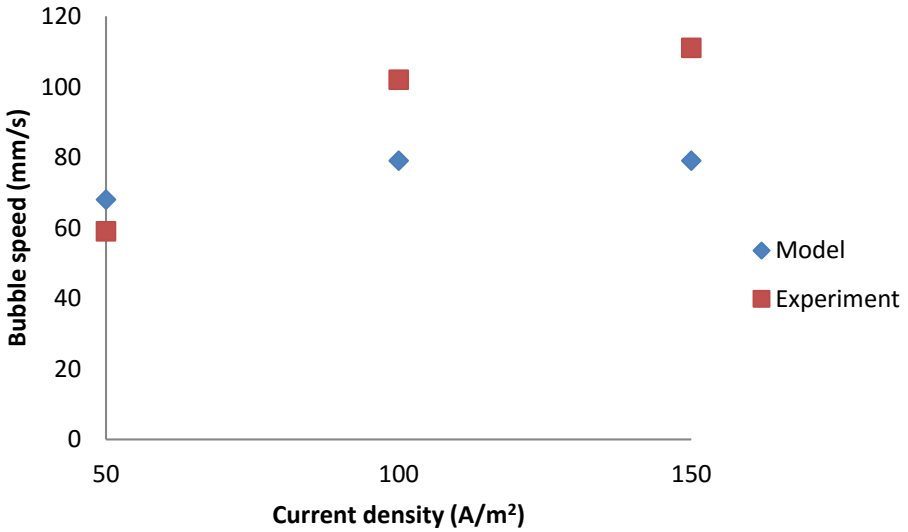

Figure 5.34: Comparison of experiment and model results for increasing current density

Figure 5.35 shows an increase in bubble speed with an increase in anode height for both the experiment and model results.

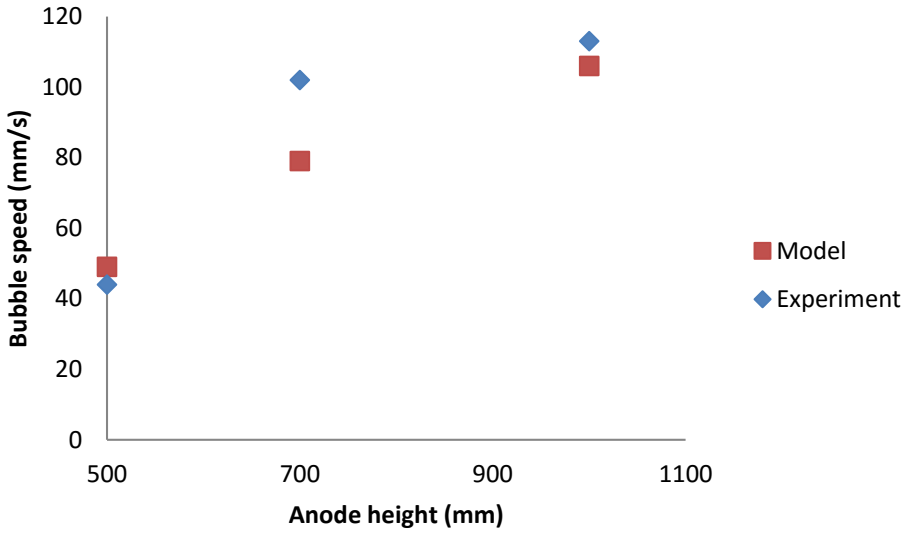

Figure 5.35: Comparison of experiment and model results for increasing anode height

Figure 5.36 shows a decrease in the bubble speed for the experimental results. However, the model predicted almost similar values for the three inter-electrode gaps tested.

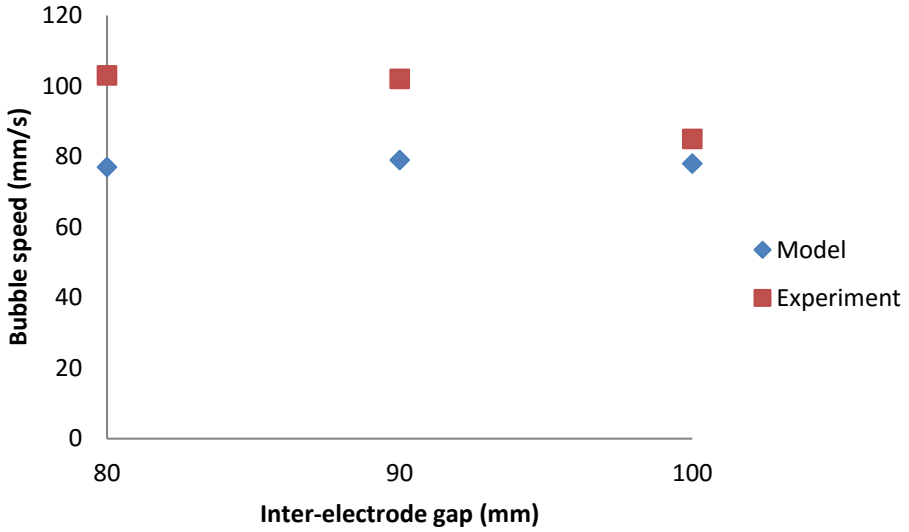

Figure 5.36: Comparison of experiment and model results for increasing inter-electrode gap

6. CONCLUSIONS AND RECOMMENDATIONS

This investigation involved an experimental setup conducted to study the flow patterns of the evolved gas bubbles and the subsequent electrolyte flow. This was both a quantitative and a qualitative study of the flow patterns in the electrolysis cell. The effect of current density, anode height and inter-electrode distance on the flow patterns was tested in the experimental work. A CFD model that was previously developed was then applied to the system used in the experimental work in order to validate the model by comparing the results obtained in the experiments and the model predictions.

All the parameters tested showed an effect on the flow fields observed especially with regards to the magnitude of the flow fields. The anode size and current density had the greatest effect on the bubble speeds and electrolyte circulation. This was mainly due to the increased amount of gas generated when using a large anode and operating at high current densities. This observation was consistent in both the experimental results and the model predictions. However, having an increased amount of gas bubbles can have negative effects on the cell efficiency and thus an optimal anode size and current density needs to be identified.

The flow fields in the cases tested by the CFD model had similar flow patterns in all the positions of interest except for Test4. Test 4 showed slightly different flow patterns to the other cases especially in Position B. The model showed the bubbles accumulating and forming a circulation loop in Position B and this was not predicted in the other tests. In Test 4 the amount of gas bubbles produced was high and this was likely the reason for the difference in the predicted flow patterns. The results from Test 4 emphasize the significant effect that the amount of electrogenerated bubbles has on the flow patterns within the cell.

On the other hand, the model did predict an accumulation and the circulation loop of the gas bubbles in Position B for the other cases. The other cases had fewer gas bubbles generated and the model predicted that the gas bubbles disengage without accumulating in Position B. This was related to the amount of gas bubbles evolved on the anode, more gas bubbles generated will result into the accumulation in Position B. More gas bubbles were generated at the highest current density and also when the largest anode was used.

The flow field patterns observed in the experiments and predicted by the model were in reasonable agreement with the exception of the gas bubbles flow pattern in Position B. The bubble speeds measured in the experiments and predicted by the model also had a reasonable agreement.

When few gas bubbles are generated they tend to rise up along the anode surface; however, when the amount of bubbles generated increases, the bubble curtain moves towards the diaphragm. In the experimental work, it was observed that a small fraction of the bubbles moved towards the diaphragm and that the diaphragm prevented most of these from crossing over to the cathode half. The diaphragm slots trapped some of the bubbles as they move upwards. The diaphragm was effective at low gas bubble production rates and not so effective at higher production rates. Reducing the gap between the diaphragm slots could allow more gas bubbles to be trapped and disengaged as they contact the diaphragm. This would prevent a significant fraction of the gas bubbles from going through the diaphragm slots.

When conducting future flow visualisation work, a dark room must be used in order to have the ultimate control of the illumination and to reduce glare and reflections. Furthermore, sufficient external lighting must be used to provide more illumination in the narrow gap between anode and diaphragm. A lens that allows magnification of the area interest should be used to get a magnified visualisation of the bubble flow. Consider employing a technique such as PIV which is more robust and will give a qualitative and quantitative analysis of the flow field.

The information and insights gained from the experimental study was useful and it should be used as a basis for the CFD model work in the future. Future work on this system should review the methodology and assumptions made in the CFD model with the aim to refine and improve the model predictions. Once the CFD model has been optimized, it should be used to identify the optimum operating conditions, cell design and configuration that will enhance the electrolyte circulation without negatively affecting the cell efficiency.

REFERENCES

Abdelouahed, L, Hreiz, R, Poncin, S, Valentin, G and Lapicque, F (2014a) "Hydrodynamics of gas bubbles in the gap of lantern blade electrodes without forced flow of electrolyte: Experiments and CFD modelling" *Chemical Engineering Science,* 111 255-265.

Abdelouahed, L, Valentin, G, Poncin, S and Lapicque, F (2014b) "Current density distribution and gas volume fraction in the gap of lantern blade electrodes" *Chemical Engineering Research and Design,* 92(3), 559-570.

Al Shakarji, R, He, Y and Gregory, S (2011) "The sizing of oxygen bubbles in copper electrowinning" *Hydrometallurgy,* 109(1–2), 168-174.

Aldas, K (2004) "Application of a two-phase flow model for hydrogen evolution in an electrochemical cell" *Applied Mathematics and Computation,* 154(2), 507-519.

Alexiadis, A, Dudukovic, M P, Ramachandran, P, Cornell, A, Wanngård, J and Bokkers, A (2011) "Liquid–gas flow patterns in a narrow electrochemical channel" *Chemical Engineering Science,* 66(10), 2252-2260.

Ashraf Ali, B and Pushpavanam, S (2011a) "Analysis of liquid circulation and mixing in a partitioned electrolytic tank" *International Journal of Multiphase Flow,* 37(9), 1191-1200.

Ashraf Ali, B and Pushpavanam, S (2011b) "Analysis of liquid circulation and mixing in a partitioned electrolytic tank" *International Journal of Multiphase Flow,* 37(9), 1191-1200.

Baloyi, J, Gololo, K V, Siyakatshana, N and Van Vuuren, D S (2014) *Basic CFD modelling of planar LiCl electrolysis cell configurations,* CSIR Materials Science and Manufacturing, Pretoria.

Bazylak, A (2009) "Liquid water visualization in PEM fuel cells: A review" *International Journal of Hydrogen Energy,* 34(9), 3845-3857.

Bešter-Rogac, M (2008) "Electrical conductivity of concentrated aqueous solutions of divalent metal sulfates" *Journal of Chemical and Engineering Data,* 53(6), 1355-1359.

Boissonneau, P and Byrne, P (2000) "Experimental investigation of bubble-induced free convection in a small electrochemical cell" *Journal of Applied Electrochemistry,* 30(7), 767-775.

Dahlkild, A A (2001) "Modelling the two-phase flow and current distribution along a vertical gas-evolving electrode" *Journal of Fluid Mechanics,* 428 249-272.

Dedigama, I, Angeli, P, Ayers, K, Robinson, J B, Shearing, P R, Tsaoulidis, D and Brett, D J L (2014) "In situ diagnostic techniques for characterisation of polymer electrolyte membrane water electrolysers: Flow visualisation and electrochemical impedance spectroscopy" *Int. J. Hydrogen Energy,* 39(2014), 4468-4482.

Downs, J C (1924) "Electrolysis process and cell", *US1501756 A,* Roessler & Hasslacher Chemical, USA.

Eigeldinger, J and Vogt, H (2000) "Bubble coverage of gas-evolving electrodes in a flowing electrolyte" *Electrochimica Acta,* 45(27), 4449-4456.

Gabrielli, C, Huet, F and Nogueira, R P (2005) "Fluctuations of concentration overpotential generated at gas-evolving electrodes" *Electrochimica Acta,* 50(18), 3726-3736.

Glas, J P and Westwater, J W (1964) "Measurements of the growth of electrolytic bubbles" *International Journal of Heat and Mass Transfer,* 7(12), 1427-"1430,IN5-IN6,1431-1443".

Goodridge, F. and Scott, K., (1995) "Introduction to electrochemical engineering", in *Electrochemical process engineering: A guide to the design of electrolytic plant.* F. Goodridge and K. Scott (Ed.), Plenum Press, New York.

Grjotheim, K., Kvande, H., Qingfeng, L. and Zhuxian, Q., (1998) "Electrochemistry of molten salts", in *Metal Production By Molten Salt Electrolysis.* K. Grjotheim, H. Kvande, L. Qingfeng and Q. Zhuxian (Ed.), China University of Mining and Technology Press (CUMTP), China.

Hine, F, Nagoya Inst of Technol, J and Murakami, K (1980) "Bubble effects on the solution IR drop in a vertical electrolyzer under free and forced convection." *Journal of the Electrochemical Society,* 127(2), 292-297.

Hreiz, R, Abdelouahed, L, Fünfschilling, D and Lapicque, F (2015) "Electrogenerated bubbles induced convection in narrow vertical cells: A review" *Chemical Engineering Research and Design,* 100 268-281.

Ito, H, Maeda, T, Nakano, A, Hasegawa, Y, Yokoi, N, Hwang, C M, Ishida, M, Kato, A and Yoshida, T (2010) "Effect of flow regime of circulating water on a proton exchange membrane electrolyzer" *International Journal of Hydrogen Energy,* 35(18), 9550-9560.

Janssen, L J J (1989) "Behaviour of and mass transfer at gas-evolving electrodes" *Electrochimica Acta,* 34(2), 161-169.

Janssen, L J J and Barendrecht, E (1985) "Mass transfer at gas evolving electrodes" *Journal of Applied Electrochemistry,* 15(4), 549-555.

Kim, K and Fahidy, T Z (1989) "A direct visualization study of anodically generated free convection-II. The effect of anode characteristics, current density and magnetic fields on flow patterns" *Electrochimica Acta,* 34(4), 533-542.

Kline, S J (1969) *Flow visualization,* National commitee for fluid mechanics films, Stanford University.

Kuhn, A.T., (1971) "The Electrowinning of Metals", in *Industrial Electrochemical Processes.* A.T. Kuhn (Ed.), Elsevier publishing company, Amsterdam-London-New York.

Lim, T.T. and Smits, A.J., (2000a) "Dye and smoke visualization", in *Flow Visualization: Techniques and Examples.* T.T. Lim and A.J. Smits (Ed.), Imperial College Pres, London.

Lim, T.T. and Smits, A.J., (2000b) "Hydrogen bubble visualization", in *Flow Visualization: Techniques and Examples.* T.T. Lim and A.J. Smits (Ed.), Imperial College Pres, London.

Lim, T.T. and Smits, A.J., (2000c) "Interpretation of flow visualisation", in *Flow Visualization: Techniques and Examples.* T.T. Lim and A.J. Smits (Ed.), Imperial College Pres, London.

Liu, C -, Sun, Z, Lu, G -, Song, X - and Yu, J - (2015) "Experimental and numerical investigation of two-phase flow patterns in magnesium electrolysis cell with non-uniform current density distribution" *Canadian Journal of Chemical Engineering,* 93(3), 565-579.

Mandin, P, Derhoumi, Z, Roustan, H and Rolf, W (2014) "Bubble over-potential during two-phase alkaline water electrolysis" *Electrochimica Acta,* 128 248-258.

Mandin, P, Derhoumi, Z, Roustan, H and Rolf, W (2013) "Bubble Over-Potential During Two-Phase Alkaline Water Electrolysis" *Electrochimica Acta,* .

Mantell, C.L., (1960) "Scope of electrochemical industries", in *Electrochemical Engineering.* C.L. Mantell (Ed.), McGraw-Hill, New York.

Mat, M D and Aldas, K (2005) "Application of a two-phase flow model for natural convection in an electrochemical cell" *International Journal of Hydrogen Energy,* 30(4), 411-420.

Matsushima, H, Iida, T and Fukunaka, Y (2013) "Gas bubble evolution on transparent electrode during water electrolysis in a magnetic field" *Electrochimica Acta,* 100 261-264.

Mavros, P (2001) "Flow visualization in stirred vessels a review of experimental techniques" *Chemical Engineering Research and Design,* 79(2), 113-127.

Mazloomi, K, Sulaiman, N B and Moayedi, H (2012) "Electrical efficiency of electrolytic hydrogen production" *International Journal of Electrochemical Science,* 7(4), 3314-3326.

Nagai, N, Takeuchi, M, Kimura, T and Oka, T (2003a) "Existence of optimum space between electrodes on hydrogen production by water electrolysis" *International Journal of Hydrogen Energy,* 28(1), 35-41.

Nagai, N, Takeuchi, M and Nakao, M (2003b) "Effects of generated bubbles between electrodes on efficiency of alkaline water electrolysis" *JSME International Journal, Series B: Fluids and Thermal Engineering,* 46(4), 549-556.

Newman, J.S., (1973) "Electrode Kinetics", in *Electrochemical Systems.* N.R. Amundson (Ed.), Prentice-Hall, Inc., United States of America.

Philippe, M, Jérôme, H, Sebastien, B and Gérard, P (2005) "Modelling and calculation of the current density distribution evolution at vertical gas-evolving electrodes" *Electrochimica Acta,* 51(6), 1140-1156.

Pletcher, D. and Walsh, F., (1990a) "Electrochemical engineering", in *Industrial Electrochemistry.* D. Pletcher and F. Walsh (Ed.), Chapman and Hall, New York.

Pletcher, D. and Walsh, F., (1990b) "Fundamental concepts", in *Industrial Electrochemistry.* D. Pletcher and F. Walsh (Ed.), Chapman and Hall, New York.

Pletcher, D. and Walsh, F., (1990c) "Water electrolysis", in *Industrial Electrochemistry.* D. Pletcher and F. Walsh (Ed.), Chapman and Hall, New York.

Riegel, H, Mitrovic, J and Stephan, K (1997) "Role of mass transfer on hydrogen evolution in aqueous media" *Journal of Applied Electrochemistry,* 28(1), 10-17.

Sandenbergh, R (2014a) *Electrometallurgy class notes on basic principles and overview,* Department of materials science and metallurgical engineering, University of Pretoria.

Sandenbergh, R (2014b) *Electrometallurgy class notes on electrochemical kinetics,* Department of materials science and metallurgical engineering, University of Pretoria.

Sandenbergh, R (2014c) *Electrometallurgy class notes on electrochemical reactors ,* Department of materials science and metallurgical engineering, University of Pretoria.

Sandenbergh, R (2014d) *Electrometallurgy class notes on electrowinning aluminium,* Department of materials science and metallurgical engineering, University of Pretoria.

Sandenbergh, R (2014e) *Electrometallurgy class notes on molten salt electrolysis,* Department of materials science and metallurgical engineering, University of Pretoria.

Schmittinger, P., (2003) "Chlorine", in *Ullman's Encyclopedia of Industrial Chemistry.* P. Schmittinger (Ed.), Wiley-VCH GmbH & Co. KGaA, Weinhem, .

Sillen, C W M P, Barendrecht, E, Janssen, L J J and van Stralen, S J D (1982) "Gas bubble behaviour during water electrolysis" *International Journal of Hydrogen Energy,* 7(7), 577-587.

St-Pierre, J and Wragg, A A (1993) "Behaviour of electrogenerated hydrogen and oxygen bubbles in narrow gap cells-part II. Application in chlorine production" *Electrochimica Acta,* 38(13), 1705-1710.

Van Vuuren, D S, Terblanche, D and Swanepoel, E (2013) "Molten salt electrolysis apparatus and process", *WO 2015/024030 A2,* CSIR, South Africa.

Vogt, H (2012) "The actual current density of gas-evolving electrodes - Notes on the bubble coverage" *Electrochimica Acta,* 78 183-187.

Vogt, H (2011) "On the gas-evolution efficiency of electrodes I – Theoretical" *Electrochimica Acta,* 56(3), 1409-1416.

Vogt, H (1989) "The problem of the departure diameter of bubbles at gas-evolving electrodes" *Electrochimica Acta,* 34(10), 1429-1432.

Vogt, H (1985) "Studies on gas-evolving electrodes: The concentration of dissolved gas in electrolyte bulk" *Electrochimica Acta,* 30(2), 265-270.

Vogt, H (1978) "Mass transfer at gas evolving electrodes with superposition of hydrodynamic flow" *Electrochimica Acta,* 23(3), 203-205.

Vogt, H and Stephan, K (2015) "Local microprocesses at gas-evolving electrodes and their influence on mass transfer" *Electrochimica Acta,* 155 348-356.

Wedin, R, Davoust, L, Cartellier, A and Byrne, P (2003) "Experiments and modelling on electrochemically generated bubbly flows" *Experimental Thermal and Fluid Science,* 27(6), 685-696.

Wüthrich, R, Comninellis, C and Bleuler, H (2005) "Bubble evolution on vertical electrodes under extreme current densities" *Electrochimica Acta,* 50(25-26 SPEC. ISS.), 5242-5246.

Zhang, D and Zeng, K (2012) "Evaluating the behavior of electrolytic gas bubbles and their effect on the cell voltage in alkaline water electrolysis" *Industrial and Engineering Chemistry Research,* 51(42), 13825-13832.

APPENDICES

Appendix A

Figure A.1: Photron FASTCAM SA4 details

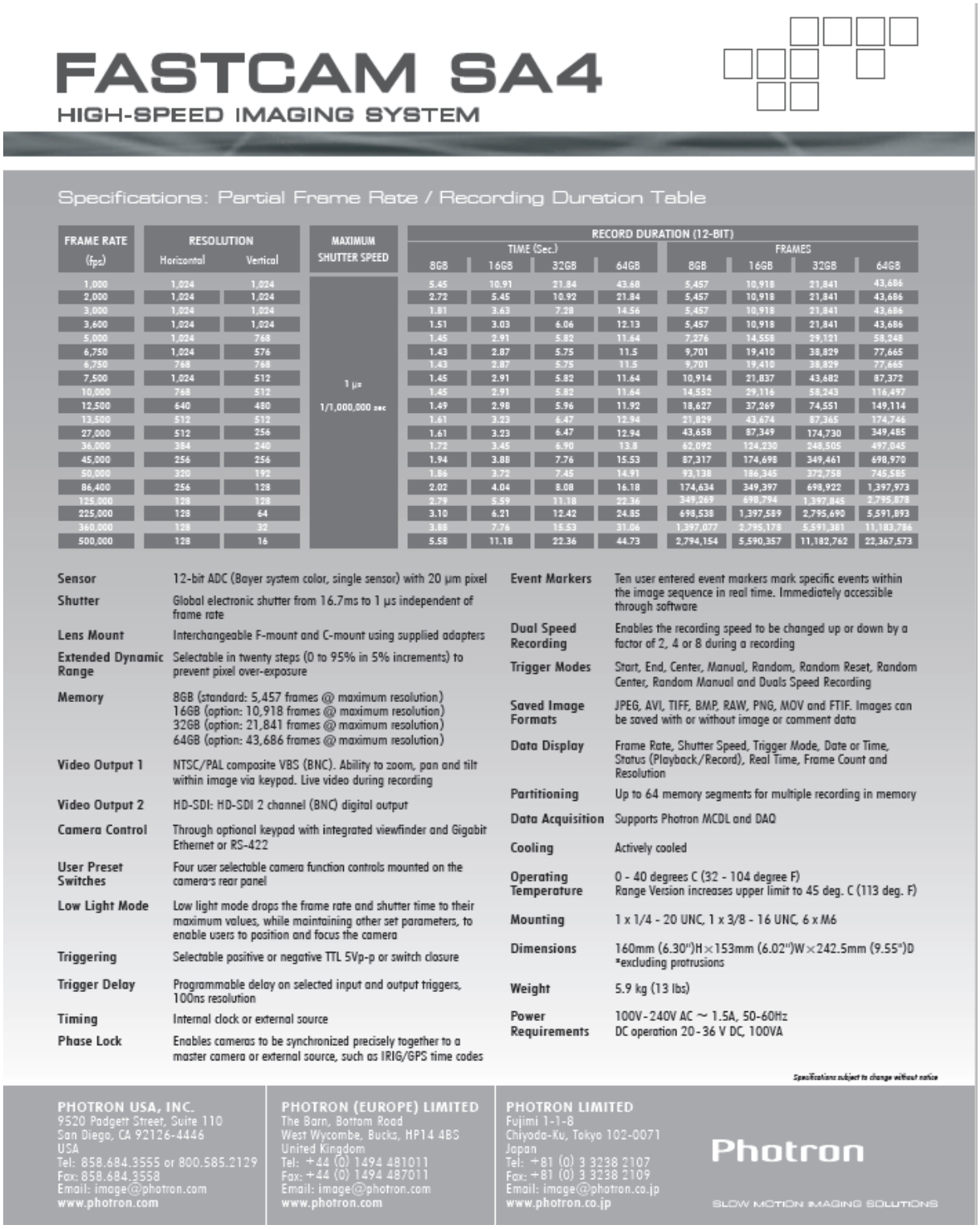

FASTCAM SA4

HIGH-SPEED IMAGING SYSTEM

Specifications: Partial Frame Rate / Recording Duration Table

FRAME RATE (fps)	RESOLUTION Horizontal	RESOLUTION Vertical	MAXIMUM SHUTTER SPEED	RECORD DURATION (12-BIT) TIME (Sec.) 8GB	16GB	32GB	64GB	FRAMES 8GB	16GB	32GB	64GB
1,000	1,024	1,024	1 µs 1/1,000,000 sec	5.45	10.91	21.84	43.68	5,457	10,918	21,841	43,686
2,000	1,024	1,024		2.72	5.45	10.92	21.84	5,457	10,918	21,841	43,686
3,000	1,024	1,024		1.81	3.63	7.28	14.56	5,457	10,918	21,841	43,686
3,600	1,024	1,024		1.51	3.03	6.06	12.13	5,457	10,918	21,841	43,686
5,000	1,024	768		1.45	2.91	5.82	11.64	7,276	14,558	29,121	58,248
6,750	1,024	576		1.43	2.87	5.75	11.5	9,701	19,410	38,829	77,665
6,750	768	768		1.43	2.87	5.75	11.5	9,701	19,410	38,829	77,665
7,500	1,024	512		1.45	2.91	5.82	11.64	10,914	21,837	43,682	87,372
10,000	768	512		1.45	2.91	5.82	11.64	14,552	29,116	58,243	116,497
12,500	640	480		1.49	2.98	5.96	11.92	18,627	37,269	74,551	149,114
13,500	512	512		1.61	3.23	6.47	12.94	21,829	43,674	87,365	174,746
27,000	512	256		1.61	3.23	6.47	12.94	43,658	87,349	174,730	349,485
36,000	384	240		1.72	3.45	6.90	13.8	62,092	124,230	248,505	497,045
45,000	256	256		1.94	3.88	7.76	15.53	87,317	174,698	349,461	698,970
50,000	320	192		1.86	3.72	7.45	14.91	93,138	186,345	372,758	745,585
86,400	256	128		2.02	4.04	8.08	16.18	174,634	349,397	698,922	1,397,973
125,000	128	128		2.79	5.59	11.18	22.36	349,269	698,794	1,397,845	2,795,878
225,000	128	64		3.10	6.21	12.42	24.85	698,538	1,397,589	2,795,690	5,591,893
360,000	128	32		3.88	7.76	15.53	31.06	1,397,077	2,795,178	5,591,381	11,183,786
500,000	128	16		5.58	11.18	22.36	44.73	2,794,154	5,590,357	11,182,762	22,367,573

Sensor	12-bit ADC (Bayer system color, single sensor) with 20 µm pixel
Shutter	Global electronic shutter from 16.7ms to 1 µs independent of frame rate
Lens Mount	Interchangeable F-mount and C-mount using supplied adapters
Extended Dynamic Range	Selectable in twenty steps (0 to 95% in 5% increments) to prevent pixel over-exposure
Memory	8GB (standard: 5,457 frames @ maximum resolution) 16GB (option: 10,918 frames @ maximum resolution) 32GB (option: 21,841 frames @ maximum resolution) 64GB (option: 43,686 frames @ maximum resolution)
Video Output 1	NTSC/PAL composite VBS (BNC). Ability to zoom, pan and tilt within image via keypad. Live video during recording
Video Output 2	HD-SDI: HD-SDI 2 channel (BNC) digital output
Camera Control	Through optional keypad with integrated viewfinder and Gigabit Ethernet or RS-422
User Preset Switches	Four user selectable camera function controls mounted on the camera's rear panel
Low Light Mode	Low light mode drops the frame rate and shutter time to their maximum values, while maintaining other set parameters, to enable users to position and focus the camera
Triggering	Selectable positive or negative TTL 5Vp-p or switch closure
Trigger Delay	Programmable delay on selected input and output triggers, 100ns resolution
Timing	Internal clock or external source
Phase Lock	Enables cameras to be synchronized precisely together to a master camera or external source, such as IRIG/GPS time codes
Event Markers	Ten user entered event markers mark specific events within the image sequence in real time. Immediately accessible through software
Dual Speed Recording	Enables the recording speed to be changed up or down by a factor of 2, 4 or 8 during a recording
Trigger Modes	Start, End, Center, Manual, Random, Random Reset, Random Center, Random Manual and Duals Speed Recording
Saved Image Formats	JPEG, AVI, TIFF, BMP, RAW, PNG, MOV and FTIF. Images can be saved with or without image or comment data
Data Display	Frame Rate, Shutter Speed, Trigger Mode, Date or Time, Status (Playback/Record), Real Time, Frame Count and Resolution
Partitioning	Up to 64 memory segments for multiple recording in memory
Data Acquisition	Supports Photron MCDL and DAQ
Cooling	Actively cooled
Operating Temperature	0 - 40 degrees C (32 - 104 degree F) Range Version increases upper limit to 45 deg. C (113 deg. F)
Mounting	1 x 1/4 - 20 UNC, 1 x 3/8 - 16 UNC, 6 x M6
Dimensions	160mm (6.30")H×153mm (6.02")W×242.5mm (9.55")D *excluding protrusions
Weight	5.9 kg (13 lbs)
Power Requirements	100V-240V AC ~ 1.5A, 50-60Hz DC operation 20-36 V DC, 100VA

Specifications subject to change without notice

PHOTRON USA, INC.
9520 Padgett Street, Suite 110
San Diego, CA 92126-4446
USA
Tel: 858.684.3555 or 800.585.2129
Fax: 858.684.3558
Email: image@photron.com
www.photron.com

PHOTRON (EUROPE) LIMITED
The Barn, Bottom Road
West Wycombe, Bucks, HP14 4BS
United Kingdom
Tel: +44 (0) 1494 481011
Fax: +44 (0) 1494 487011
Email: image@photron.com
www.photron.com

PHOTRON LIMITED
Fujimi 1-1-8
Chiyoda-Ku, Tokyo 102-0071
Japan
Tel: +81 (0) 3 3238 2107
Fax: +81 (0) 3 3238 2109
Email: image@photron.co.jp
www.photron.co.jp

Photron

SLOW MOTION IMAGING SOLUTIONS

Figure A.2: Photron FASTCAM SA 4 specifications

Appendix B: Experimental results

Appendix B1: Position A

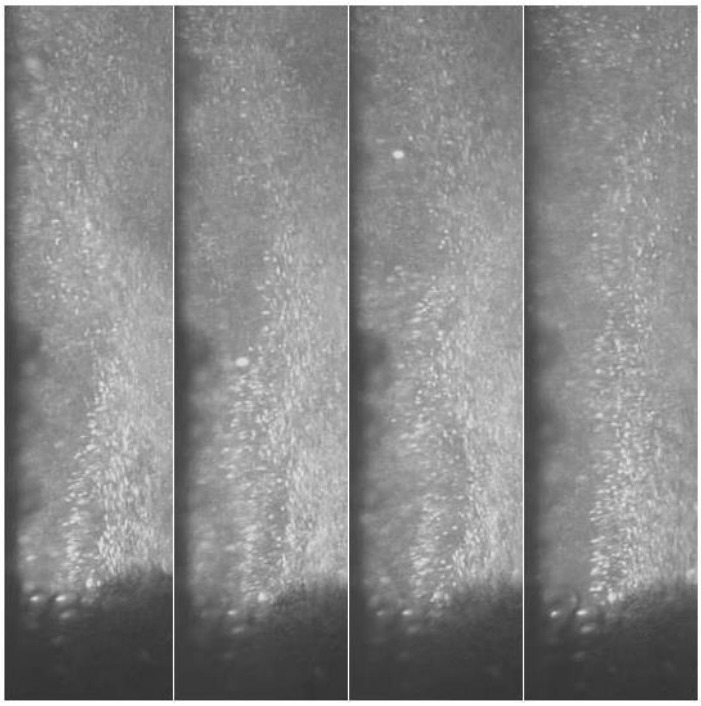

Figure A.3: Gas bubble flow field pattern at Position A for the test 1 (50 A/m^2)

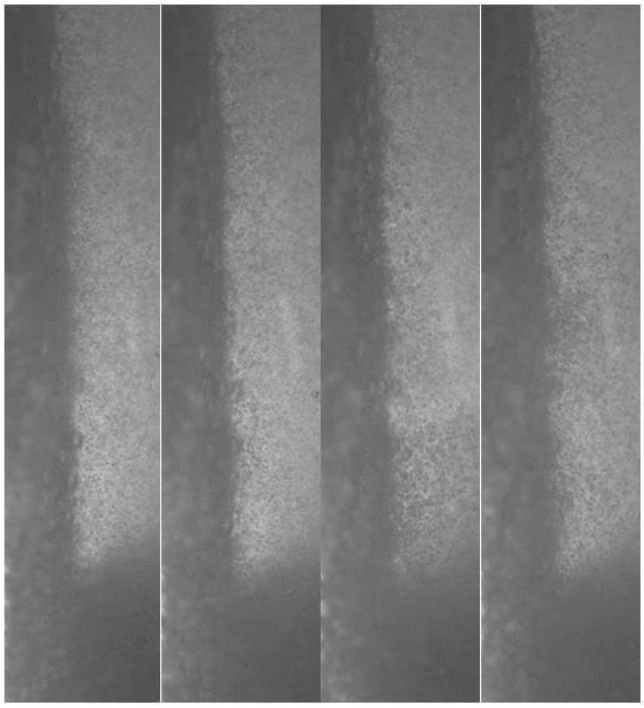

Figure A.4: Gas bubble flow field pattern at Position A for the test 2 (150 A/m^2)

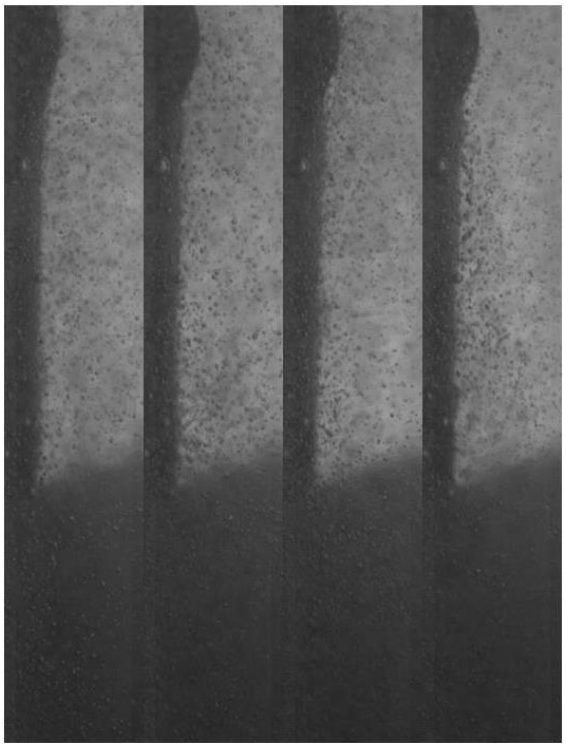

Figure A.5: Gas bubble flow field pattern at Position A for the test 4 (1m anode height)

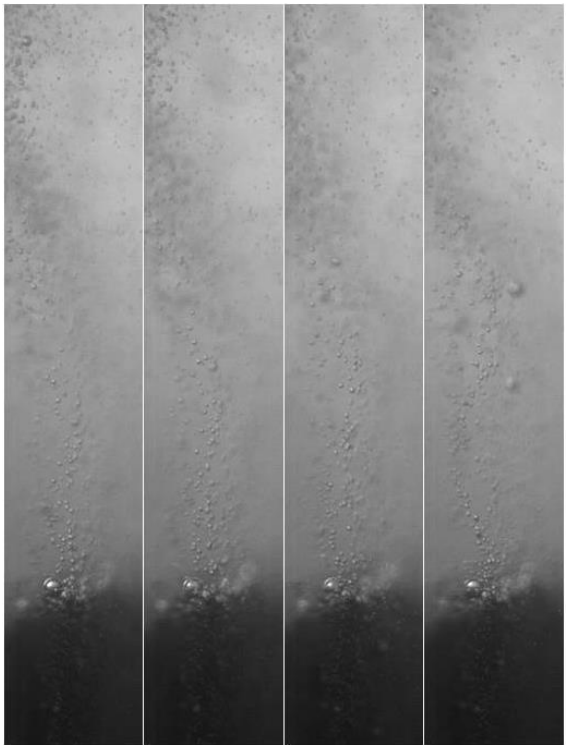

Figure A.6: Gas bubble flow field pattern at Position A for the test 6 (100mm spacing)

Appendix B2: Position B

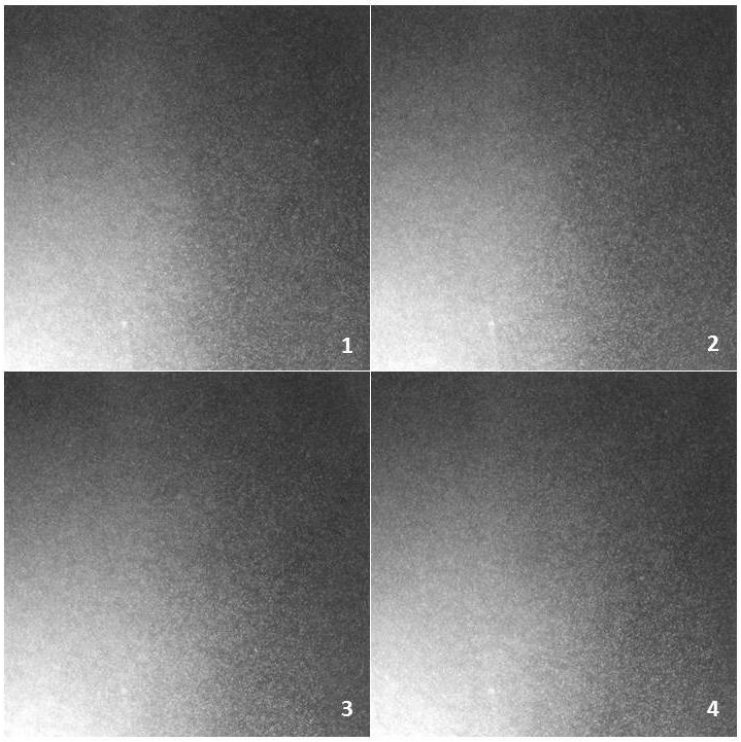

Figure A.7: Gas bubble flow field pattern at Position B for the test 1 (50 A/m^2)

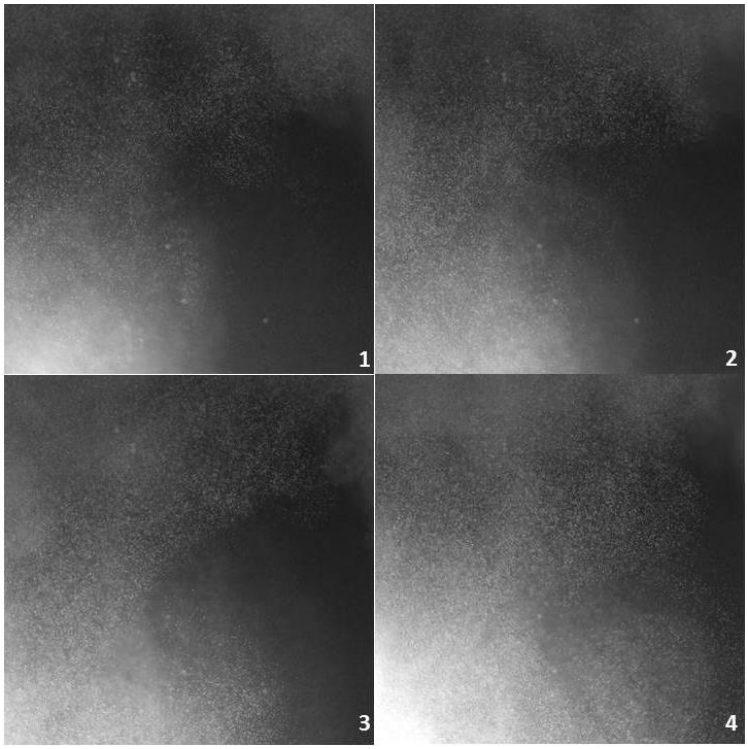

Figure A.8: Gas bubble flow field pattern at Position B for the test 2 (150 A/m^2)

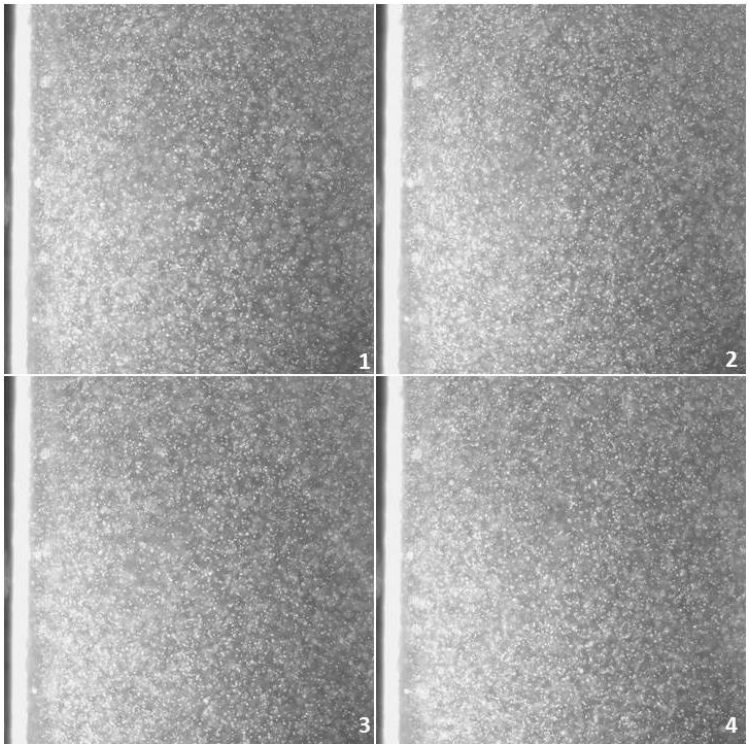

Figure A.9: Gas bubble flow field pattern at Position B for the test 4 (1m anode height)

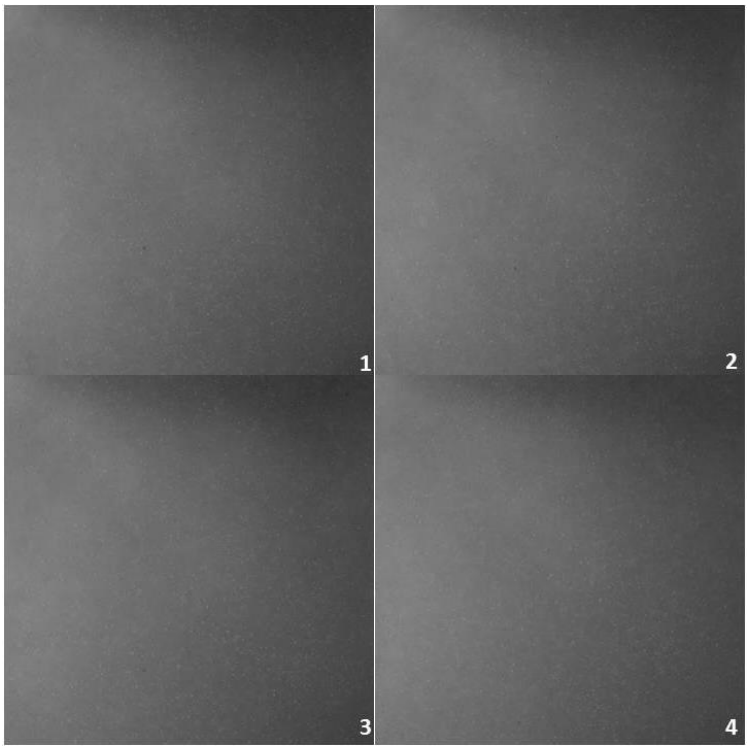

Figure A.10: Gas bubble flow field pattern at Position B for the test 6 (100mm spacing)

Appendix B3: Position C

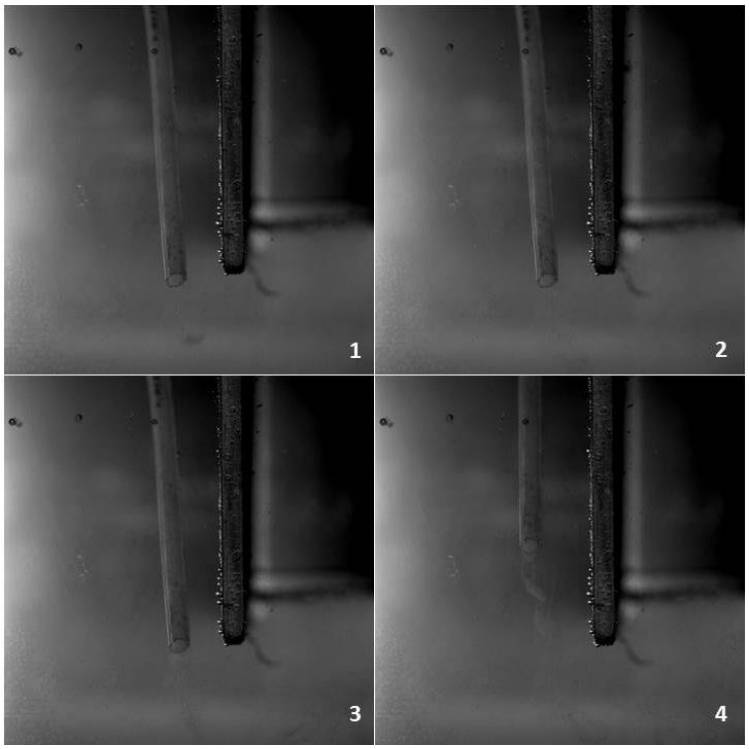

Figure A.11: Electrolyte flow field pattern at Position C for the test 1 (50 A/m^2)

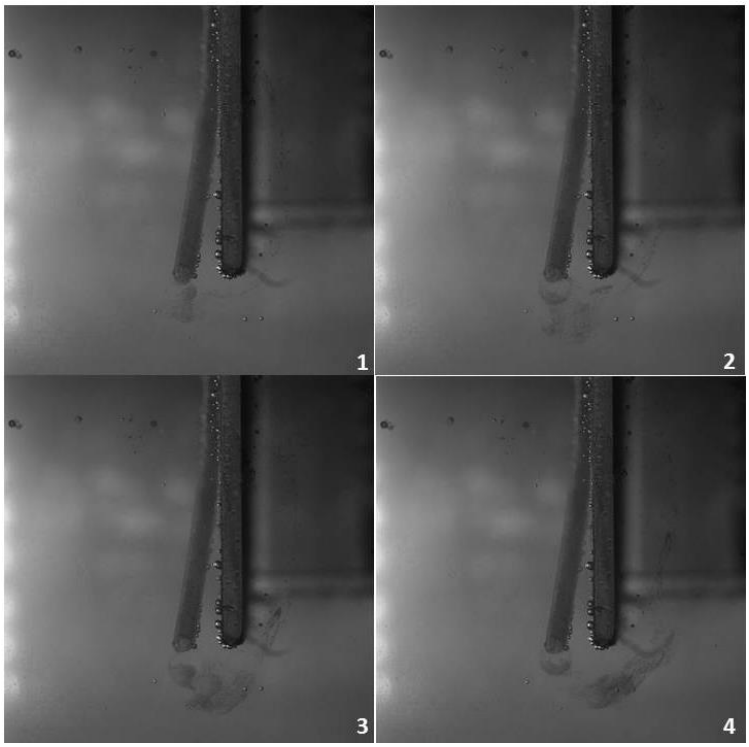

Figure A.12: Electrolyte flow field pattern at Position C for the test 2 (150 A/m^2)

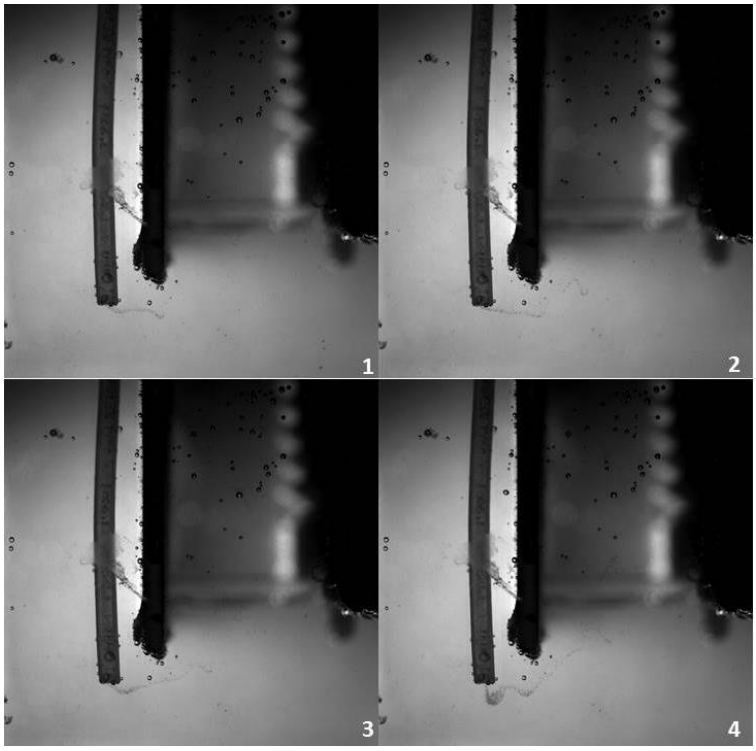

Figure A.13: Electrolyte flow field pattern at Position C for the test 4 (1m anode height)

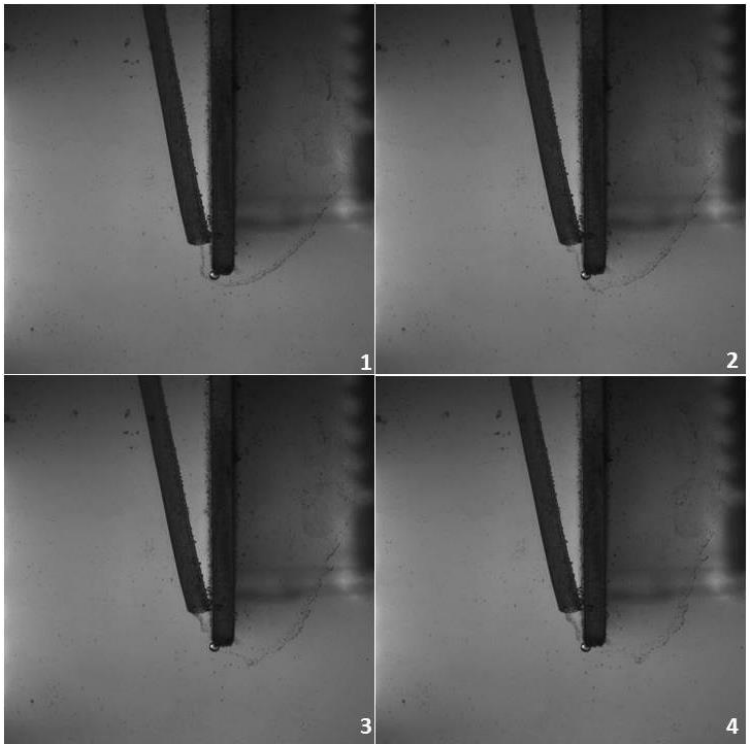

Figure A.14: Electrolyte flow field pattern at Position C for the test 6 (100mm spacing)